UNIVERSITY OF OKLAHOMA

GRADUATE COLLEGE

MAPPING BRAIN ACTIVITY AND RESTING-STATE FUNCTIONAL CONNECTIVITY WITH FUNCTIONAL NEAR-INFRARED SPECTROSCOPY

A DISSERTATION

SUBMITTED TO THE GRADUATE FACULTY

in partial fulfillment of the requirements for the

Degree of

DOCTOR OF PHILOSOPHY

By

FAN ZHANG
Norman, Oklahoma
2022

MAPPING BRAIN ACTIVITY AND RESTING-STATE FUNCTIONAL CONNECTIVITY WITH FUNCTIONAL NEAR-INFRARED SPECTROSCOPY

A DISSERTATION APPROVED FOR THE
STEPHENSON SCHOOL OF BIOMEDICAL ENGINEERING

BY THE COMMITTEE CONSISTING OF

Dr. Han Yuan, Chair

Dr. Lei Ding, Co-chair

Dr. Qinggong Tang

Dr. Michael Markham

Dr. Calin Prodan

Acknowledgements

First and foremost, I would like to express my deepest gratitude to my advisor, Dr. Han Yuan, who directed me to this research with enormous support and resources throughout the program, for her help, guidance and patience over the past five years. Dr. Yuan has provided me with an invaluable research space to explore different research projects and helped me to develop professionally.

I would also like to thank my co-advisor, Dr. Lei Ding, for his support and guidance in my research work. In addition, I would like to express my special thanks to him and his former student Dr. Ali Fahim Khan for helping with the tomography reconstruction as my research collaborators.

My gratitude also goes to my committee members, Dr. Qinggong Tang, Dr. Michael Markham, and Dr. Calin Prodan, for their precious feedback, advice and encouragement at each stage of my Ph.D. study.

I would also like to thank all my lab mates and colleagues, Dr. Ali Fahim Khan, Dr. Yafen Chen, Dr. Guofa Shou, Dr. Yuxuan Chen, Julia Tang, Daniel Cheong, Adaira Reid and many others whom I had the pleasure to work with and from whom I have gained so much support during the past five years. I am grateful for their great assistance and insightful discussions in my research projects. I would also like to thank all my other friends who have given me support in various ways.

Finally, I would like to express my deepest appreciation to my parents and sister for their unconditional support and love in my life.

The work in this dissertation was supported by National Science Foundation (NSF) RII Track-2 FEC 1539068, NSF RII Track-4 2132182, National Institute of

General Medical Sciences P20GM135009, Oklahoma Science and Technology Research and Development HR16-057, National Institutes of Health (NIH) U54GM104938, Oklahoma Shared Clinical and Translational Resources, OU Undergraduate Research Opportunities Program (UROP) and OU Institute for Biomedical Engineering, Science, and Technology (IBEST).

Contents

List of Tables

List of Figures

Abstract

Functional near-infrared spectroscopy (fNIRS) as a non-invasive optical imaging technique to measure cerebral hemodynamics has seen rapid development and increasing use in studying the human brain. fNIRS measures relative changes of oxygenated and deoxygenated hemoglobin in the local tissues as a surrogate measurement of neuronal activity, similarly to the blood-oxygenation-level-dependent (BOLD) functional magnetic resonance imaging (fMRI) which is the current golden standard of functional neuroimaging. Compared with fMRI, fNIRS offers competitive advantages, including low cost, portability, and compatibility with medical electronic devices implanted in patients. However, fNIRS has its limitations and faces several challenges. My dissertation aims to tackle several existing challenges in fNIRS and facilitate the achievement of fNIRS's tremendous potential in research and clinical applications.

Firstly, fNIRS suffers from its susceptibility to superficial blood flow, cardiac pulsation, respiration, and head and jaw motions, which can lead to false positives or negatives in imaging brain activation and connectivity. Most existing fNIRS studies were based on partial montages and have not yet been fully investigated in a whole-head montage in a complex task when concurrent activations from multiple distant regions arise or in a resting-state task when coherent spontaneous activity across functionally connected areas. We have established the capability to record fNIRS signals in a cap-based, whole-head and high-density montage with short-separation channels for superficial signals and auxiliary measurements for physiological noises. I have developed a *novel* automatic denoising method namely PCA-GLM and demonstrated the efficacy of PCA-GLM in correcting fNIRS signals recorded during a visually guided motor task.

Secondly, the capability of using whole-head fNIRS to map the resting-state functional connectivity in large-scale brain networks, especially the default mode network which is critically implicated in the aging process and Alzheimer's disease, has not been fully established and benchmarked to fMRI. We demonstrated the feasibility of the cap-based, whole-head and high-density fNIRS system in mapping the default mode network using conventional seed-based functional connectivity analysis. Moreover, via cross-modal comparison in the same subjects, we have *for the first time* demonstrated the similarity between the default mode network obtainable by a portable fNIRS system and that from fMRI, especially the medial prefrontal, midline posterior and parietal structures that are important biomarkers for normal aging.

Thirdly, the aliasing effects due to an insufficient sampling rate on functional connectivity which commonly occur in functional neuroimaging modalities, especially fMRI, are still poorly understood. Meanwhile, with the advancements in hardware and growing interest in developing high-density fNIRS with a whole-head coverage, the increases in the numbers of optical sources and detectors might come at a price of a decrease in the sampling rate. We have shown that the aliased activity due to a low sampling frequency has resulted in aliased connectivity. Furthermore, *for the first time*, we have discovered a network organization of such aliased functional connectivity that exists within the distribution of the default mode network, which might have confounded our understanding of the resting-state functional connectivity in the human brain.

Lastly, in addition to head motion, fNIRS is also vulnerable to jaw movements, such as clenching teeth, which can affect fNIRS measurements in the auditory, parietal and prefrontal cortices in the studies of hearing, speech and cognitive functions. While

many previous studies have investigated the impact and correction of head movements, the effect and handling of jaw movements in fNIRS signals remain unclear. We have designed a *novel* individually customized bite bar. Our experimental work has demonstrated that the bite bar and the previously developed PCA-GLM method are effective in suppressing jaw movements, removing motion artifacts, and therefore improving auditory response and resting-state functional connectivity.

The outcomes of my dissertation have made significant advancements towards tackling the technical challenges in fNIRS. My work has paved the pathway for using fNIRS as a broadly accessible and noninvasive neuroimaging technique in many clinical applications, such as measuring auditory response in cochlear implant users, detecting abnormality of neurovascular coupling in diseased or impaired conditions, and monitoring the deterioration of the brain function in normal aging and Alzheimer's disease.

Acronyms

EEG: electroencephalography

MEG: magnetoencephalography

fNIRS: functional near-infrared spectroscopy

fMRI: functional magnetic resonance imaging

PET: positron emission tomography

SPECT: single-photon emission computed tomography

DOT: diffuse optical tomography

BOLD: blood-oxygenation-level-dependent

SS: short-separation

LS: long-separation

HbO: oxygenated hemoglobin

HbR: deoxygenated hemoglobin

HbT: total hemoglobin

PCA: principal component analysis

CSU: coefficient of spatial uniformity

PC-LS: spatially uniform component

PC-SS: superficial global component

GLM: general linear model

HRF: hemodynamic response function

CNR: contrast-to-noise ratio

adjusted R^2: adjusted coefficient of determination

RSFC: resting-state functional connectivity

RSN: resting-state network

DMN: default mode network

AD: Alzheimer's Disease

GVTD: global variance in temporal derivative

FEM: finite element method

FWHM: full width at half maximum

PSD: power density spectrum

DS: down-sampled

AFCP: aliased functional connectivity pattern

ROI: region-of-interest

mPFC: medial prefrontal cortex

IPL: inferior parietal lobe

1 Chapter 1: Introduction

1.1 Functional Neuroimaging

In the past decades, noninvasive functional neuroimaging techniques have been extensively used to investigate the human brain function and connectivity in healthy and diseased conditions. Fundamentally, human brain activity can be reflected by electrophysiological signals directly associated with neural activity as well as metabolism and hemodynamic response coupled with neural activity (**Figure 1-1**) (He and Liu, 2008). The metabolic and hemodynamic signals, as surrogate measurements, are used to infer the underlying neural activity (Hillman, 2014; Tsvetanov et al., 2021). Correspondingly there are two categories of noninvasive functional imaging techniques based on their imaging principles. Electroencephalography (EEG) and magnetoencephalography (MEG) measure the electrical and magnetic signals induced by neural activity respectively. Functional magnetic resonance imaging (fMRI), single-photon emission computed tomography (SPECT) and positron emission tomography (PET) measure the hemodynamic or metabolic signals evoked by neural activity. Among these techniques, EEG and fMRI are prevalent in research and clinical diagnosis due to their non-invasive and non-radiative features (Glover, 2011; Light et al., 2010). EEG measures the electrical potential by electrodes placed on the scalp (Teplan, 2002). fMRI measures the blood-oxygenation-level-dependent (BOLD) signal modulated by neuronal activity (Ogawa et al., 1990). These two techniques have their own merits and limitations. EEG has high temporal resolution but low spatial resolution (Burle et al., 2015), while fMRI has high spatial resolution but low temporal resolution (Glover, 2011). Notably, fMRI has been the primary modality used for functional neuroimaging in modern human brain mapping

studies, such as the Human Connectome Project (Van Essen et al., 2013), the Alzheimer's Disease Neuroimaging Initiative (ADNI) (Mueller et al., 2005), the Adolescent Brain Cognitive Development (ABCD) study (Casey et al., 2018), etc. However, although fMRI has provided unprecedented opportunities to understand the human brain functions, the limited accessibility and high expenses of MRI instruments become a bottleneck in the workflow, especially in studying large populations, which is further amplified by health disparities in underserved rural populations and socioeconomically disadvantaged populations of any race or ethnicity. In this context, functional near-infrared spectroscopy (fNIRS), as a non-invasive optical imaging technique with advantages in portability, cost-effectiveness, and compatibility with medical electronic implants has recently drawn great interest in the functional neuroimaging community (Scholkmann et al., 2014). The motivation of this dissertation is to facilitate the research and clinical applications of fNIRS.

The next section offers an overview of fNIRS and discusses several existing challenges in tapping the full potential of fNIRS in human brain research and clinical diagnosis.

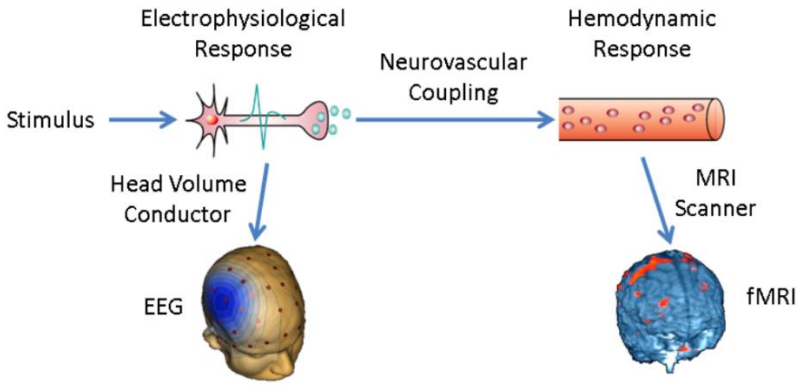

Figure 1-1: Electrical and hemodynamic signals measured by noninvasive functional neuroimaging (adapted from He and Liu (2008), with permission).

1.2 Functional Near-Infrared Spectroscopy

Functional near-infrared spectroscopy (fNIRS) is a non-invasive optical imaging technology that has seen rapid development and increasing use in human brain studies (Scholkmann et al., 2014; Torricelli et al., 2014; Villringer and Chance, 1997; Wheelock et al., 2019). fNIRS measures the changes in cortical hemoglobin oxygenation as surrogates of neuronal activity, similarly to functional magnetic resonance imaging (fMRI) (Scholkmann et al., 2014), but using near-infrared light instead of a magnetic field, as shown in **Figure 1-2**. fNIRS offers several advantages over fMRI: (1) fNIRS has a higher temporal resolution (about 10 Hz) compared with fMRI (about 0.5 Hz) and therefore avoids the aliasing of cardiorespiratory activity (Tong et al., 2011); (2) fNIRS has better cost-effectiveness, portability, and compatibility with other medical devices and thus is more accessible in the research and clinical applications (Hu et al., 2020); (3) fNIRS is more tolerant to motion artifacts and enables measuring the cortical activity while the subject is in a natural position in a less confined space (Cui et al., 2010; Tak and Ye, 2014); (4) fNIRS can provide multiple contrasts including concentration changes in oxyhemoglobin (HbO), deoxyhemoglobin (HbR) and total hemoglobin (HbT) (Tak and Ye, 2014) while the BOLD signal in fMRI is primarily sensitive to the concentration changes in HbR (Buxton, 2013); (5) fNIRS generates less acoustic background noise which can increase attentional demands that bias the resting-state functional connectivity (RSFC) in default-mode network (DMN) (Gaab et al., 2008; Rondinoni et al., 2013); (6) fNIRS allows long-term monitoring, which is especially critical in studying the RSFC in

the developing brain (Hu et al., 2020). Thus, increasing efforts are dedicated to exploring the use of fNIRS in populations not suitable for or with contraindications to fMRI, such as infants (Homae et al., 2010; Molavi et al., 2013; Watanabe et al., 2017; White et al., 2012) or patients with cochlear implants (Bortfeld, 2019; Saliba et al., 2016).

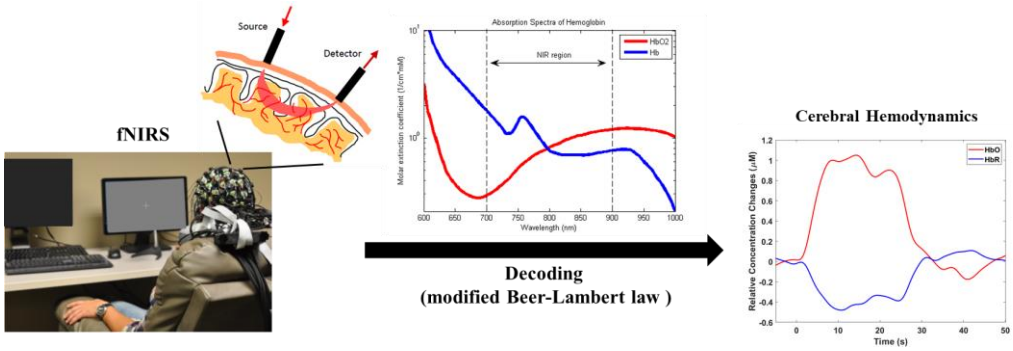

Figure 1-2: Illustration of fNIRS imaging in Dr. Yuan's laboratory. The inserted schematic figure of the source and detector is adapted from https://nirx.net/. The absorption spectra of HbO and HbR in the near-infrared range are adapted from Wikipedia (Figure shared under Creative Commons Attribution-Share Alike License 3.0, https://en.wikipedia.org/wiki/File:Oxy_and_Deoxy_Hemoglobin_Near-Infrared_absorption_spectra.png).

Furthermore, fNIRS can be easily combined with other neuroimaging modalities such as electroencephalography (EEG) (Chiarelli et al., 2017). EEG and fMRI have been integrated to concurrently measure the electrophysiological and hemodynamic signals and achieve a more comprehensive understanding of RSFC and neurovascular coupling (Britz et al., 2010; Musso et al., 2010; Yuan et al., 2016; Yuan et al., 2012). Previous simultaneous fMRI-EEG studies have shown that resting-state networks derived from fMRI data are correlated with the microstates reflected in EEG data (Britz et al., 2010; Musso et al., 2010; Yuan et al., 2012). However, the rapidly switching magnetic gradient

in fMRI heavily interferes with the EEG instruments and causes gradient artifacts in the EEG signals (Bénar et al., 2003). Another study showed that the ventilation system of fMRI can also introduce artifacts in the EEG signals (Nierhaus et al., 2013). Methods have been reported in the literature to reduce the gradient artifacts in EEG data recorded during fMRI (Liu et al., 2012; Mantini et al., 2007; Mayeli et al., 2016). Nevertheless, recording EEG concurrently with fMRI remains a challenging operation. In contrast to fMRI-EEG, the optical signals in fNIRS and electrical signals in EEG are "orthogonal" and thus can avoid direct interferences during simultaneous multi-modal imaging (Chiarelli et al., 2017). In addition, the fNIRS-EEG combination has better portability and lower operation cost. Therefore, fNIRS-EEG can be used for long-term monitoring in studying aging and developing brains in both clinical and non-clinical environments. Furthermore, the fNIRS-EEG multimodal imaging can measure the vascular and neuronal functional connectivity simultaneously and thus has the potential to unveil the neurovascular coupling between two types of connectivity (Scholkmann et al., 2014). A recent fNIRS-EEG study has demonstrated that the fNIRS dynamic resting-state functional connectivity between frontal, parietal and temporal regions in DMN is correlated with an EEG microstate (Zhang and Zhu, 2020).

However, although fNIRS is attractive in clinical research (Chen et al., 2020b), its widespread use has been held back due to contamination of physiological noise in the recordings (Kirilina et al., 2013; Pinti et al., 2018; Tong, 2012). Firstly, due to the fact that the near-infrared light passes through the skin and skull before reaching the cerebral cortex, the fNIRS measurements are sensitive to absorption in the superficial layers of the head (Saager and Berger, 2005). Thus, the signal obtained from a regular long-

separation (LS) channel (for example, 3 cm apart between a pair of source and detector in adults) is a mixture of absorptions by deep cerebral and superficial tissues (Saager and Berger, 2005; Takahashi et al., 2011). Furthermore, even in the cerebrally originated signals, there could be contaminations arising from physiological systemic activity, including changes in heart rate, blood pressure, breathing rate and volume, autonomic nervous system activity and movements (Kirilina et al., 2013; Sasai et al., 2011; Schecklmann et al., 2017; Tachtsidis and Scholkmann, 2016; Tong, 2010; Yuan et al., 2013). The superficial activity and physiological noise collectively affects the accuracy of fNIRS, leading to false positives and false negatives in the imaging of functional brain activity (Tachtsidis and Scholkmann, 2016). Most of the existing fNIRS signals denoising methods were developed in a partial montage that only includes a few channels (Gagnon et al., 2011; Zhang et al., 2007; Zhang et al., 2005), or covers only part of the cortex (Sato et al., 2016; Zhang et al., 2016). Therefore, a denoising strategy that is proven effective for the whole-head montage is needed to enable fNIRS for studying large-scale brain networks, especially in diseased conditions (Irani et al., 2007; Leff et al., 2011; Obrig, 2014).

Since the first finding showed that the low-frequency oscillations (<0.1 Hz) in the blood-oxygenation-level-dependent (BOLD) signals measured by functional magnetic resonance imaging (fMRI) are temporally correlated in the motor cortex and other regions related to motion function under the resting state (Biswal et al., 1995), a great deal of effort has been dedicated to the research of RSFC and resulted in significant advances in the understanding of the functional organization, aging process and neurological disorders of the human brain (Zhang and Raichle, 2010). While remarkably consistent

spatial patterns of fMRI resting-state networks (RSNs) have been found in healthy subjects (Beckmann et al., 2005; Damoiseaux et al., 2006), substantial modulation or alteration can be seen in normal aging (Andrews-Hanna et al., 2007; Damoiseaux et al., 2008) and neurological disorders (Zhang and Raichle, 2010). Research groups have employed fNIRS to characterize network-level neural activity in healthy adults (Aihara et al., 2020; Eggebrecht et al., 2014; Lu et al., 2010; Mesquita et al., 2010; Obrig et al., 2000; Sasai et al., 2011; White et al., 2009; Zhang et al., 2010), assess the abnormality in diseased conditions (Irani et al., 2007; Keehn et al., 2013; Leff et al., 2011), and explore the effects of normal aging (Li et al., 2018). Whole-head and cap-based fNIRS recordings have become available with diffuse optical tomography (DOT) to reconstruct the voxel-wise activity (Chen et al., 2020c; Khan et al., 2021; Zhang et al., 2021), however, RSFC of a complete DMN has not been fully revealed and benchmarked to that in fMRI (Aihara et al., 2020; Eggebrecht et al., 2014).

Although fNIRS has an intrinsic advantage in sampling rate, it can encounter the same well-known problem, i.e., insufficient sampling rate, in fMRI. With the growing interest in utilizing fNIRS to study large-scale functional connectivity, the number of sources and detectors will need to significantly increase in order to achieve high-density measurements and whole head coverage. The broader coverage of the head and the increase in the density of optodes might come at the price of a decrease in the sampling rate. Despite the fact that intrinsic oscillations of the vascular networks (Drew et al., 2020; Mateo et al., 2017) and other physiological oscillations such as respiration, cardiac pulsation and cerebrospinal fluid may also contribute to the measured hemodynamics in the upper frequencies (Liu, 2016), our understanding of the human brain functional

connectivity has been primarily established by fMRI at sub-hertz sampling rates for the activity below 0.1 Hz (Biswal et al., 1996; Cordes et al., 2001; Mitra et al., 1997). However, it is still poorly understood how the oscillations that exist beyond the safely sampled range could contribute to the network organization via the aliased effects.

fNIRS has drawn increasing interest from the neuroscience community to employ this technique to investigate auditory function in healthy subjects and patients with hearing loss (Pollonini et al., 2014; Saliba et al., 2016). For example, fNIRS can be used in infants who have cochlear implants and are unable to verbally communicate their hearing and comfort when adjusting sound levels (Bortfeld, 2019). The understanding of auditory perception mechanisms of normal sound and cochlear stimuli can facilitate the early intervention of hearing loss in infants to reserve and develop their speech and auditory function. There are several critical confounding factors in fNIRS signals, including interferences from superficial layers of the head, systemic physiological noise and motion artifacts (von Lühmann et al., 2019; von Lühmann et al., 2020; Zhang et al., 2021). Although less vulnerable to head movements, fNIRS can still suffer from jaw movements such as speech speaking and voluntary jaw clenching, which can cause contractions of the temporalis muscle (Novi et al., 2020; Schecklmann et al., 2017). The jaw movements could result in blood flow changes in the temporal muscle as well as relative movements between the optodes and the scalp, leading to artifacts in the fNIRS signals (Schecklmann et al., 2017). While many previous studies have investigated the impact and correction of head movements (Cui et al., 2010; Fishburn et al., 2019; Izzetoglu et al., 2010; Scholkmann et al., 2010), the effect and especially handling of jaw movements in fNIRS signals remain largely unclear (Novi et al., 2020; Schecklmann et al., 2017).

The research work included in my dissertation aims to tackle several abovementioned challenges and facilitate the achievement of fNIRS's tremendous potential in research and clinical applications.

1.3 Outline of the Dissertation

This dissertation is organized as follows:

In **Chapter 2** (titled "Correcting physiological noise in whole-head fNIRS"), I will describe the development of a novel algorithm for removing the physiological noises in whole-head fNIRS recordings. fNIRS is known for being susceptible to interferences from physiological activity and motion artifacts. There was an unmet need for a denoising method for whole-head recordings. This chapter proposed and validated an automated pipeline for whole-head fNIRS measurements.

In **Chapter 3** (titled "Network organization of resting-state cerebral hemodynamics and their aliasing contributions measured by functional near-infrared spectroscopy"), I will describe the work of validating fNIRS with fMRI in a group of subjects. Functional connectivity measured by fMRI has been increasingly used as a biomarker to assess cerebral activity in neurological and psychiatric diseases. However, fMRI is bulky and expensive and has a low sampling rate. This chapter validated whole-head fNIRS in mapping large-scale distributed resting-state functional connectivity. In addition, I will also describe my discovery of the aliasing effects on functional connectivity in this investigation on experimental data.

In **Chapter 4** (titled "Characterization of jaw-clenching artifacts in fNIRS recordings and signal correction"), I will describe my development of a novel bite-bar

apparatus and the denoising algorithm in addressing the issue of jaw-movement-related artifacts in fNIRS. Although fNIRS is less vulnerable to head movements, fNIRS can still suffer from jaw movements such as speech speaking and voluntary jaw clenching. This chapter characterized the motion artifacts due to jaw clenching movements in fNIRS signals and validated the efficacy of a customized bite bar and PCA-GLM established in Chapter 2 in improving the fNIRS signals in auditory and resting tasks.

In **Chapter 5** (titled "Conclusions and future work"), I summarize the methodological developments and research findings accomplished in this dissertation. Meanwhile, I also discuss the limitations in this dissertation and provide an outlook as well as recommendations for future research on resting-state functional connectivity with whole-head, high-density fNIRS.

2 Chapter 2: Correcting Physiological Noise in Whole-head fNIRS

2.1 Introduction

Currently, denoising methods for fNIRS that are commonly used in the literature include temporal filtering as a minimal preprocessing method, general linear model (GLM) with short-separation (SS) channels (namely SS-GLM) (Gagnon et al., 2011), spatial filtering based on principal component analysis (namely PCA) (Virtanen et al., 2009; Zhang et al., 2016; Zhang et al., 2005), and PCA filtering integrated with SS channels (namely Sato method) (Sato et al., 2016). Given a sufficient sampling rate in the acquisition, a minimal preprocessing method that primarily relies on band-pass filtering is effective in removing cardiac pulsation (0.8 - 1.6 Hz) and respiration (0.2 - 0.6 Hz) but is not capable to address the noise in low-frequency oscillations (0.04 - 0.2 Hz, LFO) and very-low-frequency oscillations (0.01 - 0.04 Hz, VLFO) (Stefanovska et al., 1999; Tong et al., 2011), which however overlap with the frequencies of resting and evoked neural activity. More advanced methods such as the SS-GLM method utilize additional information from SS channel which has a source-detector distance smaller than 1 cm and is primarily sensitive to superficial tissues (Gagnon et al., 2012; Gagnon et al., 2011; Saager and Berger, 2005). The SS signals can be regressed from LS recordings to attenuate noise originating from superficial tissues and physiological activity (Gagnon et al., 2011). In addition, there are other denoising methods based on SS channels, including temporal embedding canonical-correlation analysis (tCCA) (von Lühmann et al., 2019; von Lühmann et al., 2020), Kalman filter (Dong and Jeong, 2018), etc. However, direct removal of SS recordings may be problematic. Theoretic simulations have demonstrated that SS recordings might contain contributions from deep brain tissues as well (Saager

and Berger, 2005), although in much smaller magnitudes. More importantly, empirical evidence showed that tasks can induce block-wise modulations in SS channels (Kirilina et al., 2012; Takahashi et al., 2011). The task-related changes of oxygenated and deoxygenated hemoglobin (HbO and HbR) obtained in SS recordings have been found to be remarkably similar to those activations observed in regular LS channels, which implies that directly regressing SS recordings from LS recordings may reduce the effect size of detecting task-related activations (Tachtsidis and Scholkmann, 2016). Meanwhile, another type of PCA-based denoising method has limitations too. Out of multiple orthogonal components yielded by applying PCA on LS data, one or a subset of components should be selected and removed as noise to enhance brain activation patterns (Zhang et al., 2016; Zhang et al., 2005). However, the selection of noise components in PCA-based methods typically relies on a manual decision and lacks a systematic approach that has fully validated the origins of physiological noise in the removed components. Due to the intrinsic correlation between noise and neural-associated signals (e.g., the SS and LS signals exhibit similar task-modulated changes), PCA-based methods have limitations in separating noise from signals of interest. Therefore, removing too many principal components is possible and can result in a substantial reduction of activation (Boas et al., 2004; Zhang et al., 2016; Zhang et al., 2005). Other methods based on the decomposition of the multi-channel fNIRS data, such as the independent component analysis (ICA) (Kohno et al., 2007), also suffer from similar limitations when manually choosing noisy components to remove. Thus, in both PCA- and ICA-based methods, the preprocessing procedure is not fully automatic and their performance is not satisfactory (Watabe and Hatazawa, 2019). In the meantime, applying PCA to short-

channel recordings is suggested as an effective strategy to overcome the difficulties in LS-based PCA and SS-GLM methods, while exploiting the regional homogeneity in SS recordings (Sato et al., 2006).

Furthermore, physiological fluctuations in cardiac pulsation, respiration, and voluntary head and jaw movements can affect the fNIRS measurements (Kirilina et al., 2013; Sasai et al., 2011; Tachtsidis and Scholkmann, 2016; Tong, 2010; Yuan et al., 2013). While filtering is commonly used to filter out the range regarding pulse and respiration, non-stationary fluctuations that are related to slow changes in pulse and respiration rate and volumes have been shown to impact hemodynamic measurements in fMRI (Birn et al., 2006; Chang et al., 2009; Hu et al., 1995; Power et al., 2012; Shmueli et al., 2007; Van Dijk et al., 2012; Wise et al., 2004), and yet to be fully considered in fNIRS denoising.

In addition to the above-mentioned limitations in the fNIRS preprocessing methods, an unmet need so far is a denoising method for whole-head fNIRS recordings. Most of the existing methods were developed in a partial montage that only includes a few channels (Gagnon et al., 2011; Zhang et al., 2007; Zhang et al., 2005), or covers only part of the cortex (Sato et al., 2016; Zhang et al., 2016). Despite some recent efforts (Noah et al., 2021; Santosa et al., 2020), these methods have not yet been fully evaluated in a whole-head montage at a complex task when current activations from multiple, distant regions arise, which however is especially critical for imaging resting-state brain networks. Till now, it remains unknown whether the denoising methods for partial montages would still be effective in a whole-head montage, considering that noise in an expanded recording range will challenge the underlying assumptions employed in these

methods. Blood flow in the skin tissues covering the scalp is known to be heterogenous (Kirilina et al., 2013; Schuenke et al., 2010). Facial muscles might be another contributor to physiological noise when the fNIRS montage extends to the temporal region (Novi et al., 2020; Schecklmann et al., 2017). Therefore, a denoising strategy that is proven effective for the whole-head montage is needed to enable fNIRS for studying large-scale brain networks, especially in diseased conditions (Irani et al., 2007; Leff et al., 2011; Obrig, 2014).

In this chapter, we proposed an automatic denoising method for whole-head fNIRS recordings. Our method namely PCA-GLM integrates principal component analysis and general linear model regression based on long-separation (LS) and short-separation (SS) channels and auxiliary measurements. Experimental data acquired from thirteen healthy individuals during a visually cued motor task were used to evaluate whether activations in motor and visual areas are detectable. Then our PCA-GLM method was compared with four other commonly used methods, i.e. minimal processing of filtering only (namely No Correction), SS-GLM (Gagnon et al., 2011), PCA (Huppert et al., 2009; Zhang et al., 2005), and the Sato method (Sato et al., 2016). Performance of all methods was assessed using quantitative metrics, including contrast-to-noise ratio, within-subject standard deviation and adjusted coefficient of determination.

2.2 Methods

2.2.1 Participants

This study was approved by the University of Oklahoma Health Sciences Center Institutional Review Board. Written consent was obtained from all participants prior to the study. All the procedures were carried out in accordance with the IRB guidelines. A

total of thirteen healthy participants without any neurological or neuropsychiatric disorders were enrolled in this study. Participants received financial compensation for their participation. Data of three subjects were excluded from data analysis due to bad data quality. Therefore, data from ten subjects (four females, 34.2 ± 9.9 years old) were used for the analyses.

2.2.2 Data Acquisition

Simultaneous fNIRS and peripheral measurements were collected in all participants. In addition, EEG recordings were recorded concurrently but were not used in the present study. fNIRS data were acquired using a NIRScout system (NIRx GmbH, Berlin, Germany). As illustrated in **Figure 2-1**, The acquisition consisted of 34 dual-wavelength (760 and 850 nm) sources, 31 LS detectors and 8 SS detectors, which jointly formed 109 LS channels and 8 SS channels evenly distributed over the entire head, following a similar montage of our previous study (Chen et al., 2020b). The SS channels had source-detector separations of 8 mm. As suggested in fMRI, the sampling frequency should be set sufficiently high to avoid aliasing effects of respiratory and cardiac activity (Liu, 2016). While fNIRS has the advantage of sampling faster compared with fMRI, its sampling frequency still decreases as the number of light sources used increases. In order to maintain a high sampling rate while using a large number of sources, we employed parallel source illumination in the NIRScout system, which illuminated multiple sources in each single time step. To avoid optical crosstalk, the optimal source illumination sequence was manually generated based on the criterion that the distances between sources activated during the same step should be larger than 9 cm so that each detector does not receive light from multiple sources. 34 sources were illuminated in 10 steps,

which resulted in a sufficient sampling rate of 6.25 Hz. The sensitivity profile of the fNIRS probe to cortical absorption changes obtained by Monte Carlo simulation with photon propagation in AtlasViewer (Aasted et al., 2015) is shown in **Figure 2-1**. The number of photons in the simulation was set as 1e7 (Aasted et al., 2015). The fNIRS optodes and EEG electrodes were placed on an elastic cap (EASYCAP GmbH, Herrsching, Germany), according to the international 10-5 system (Oostenveld and Praamstra, 2001). Additional auxiliary data of acceleration, respiration, and cardiac pulses were recorded by a three-dimensional accelerometer, a pneumatic respiration belt and a photoplethysmography respectively which were connected to the auxiliary input ports of the actiCHamp system (BrainProducts, München, Germany). Auxiliary data were sampled at a frequency of 500 Hz.

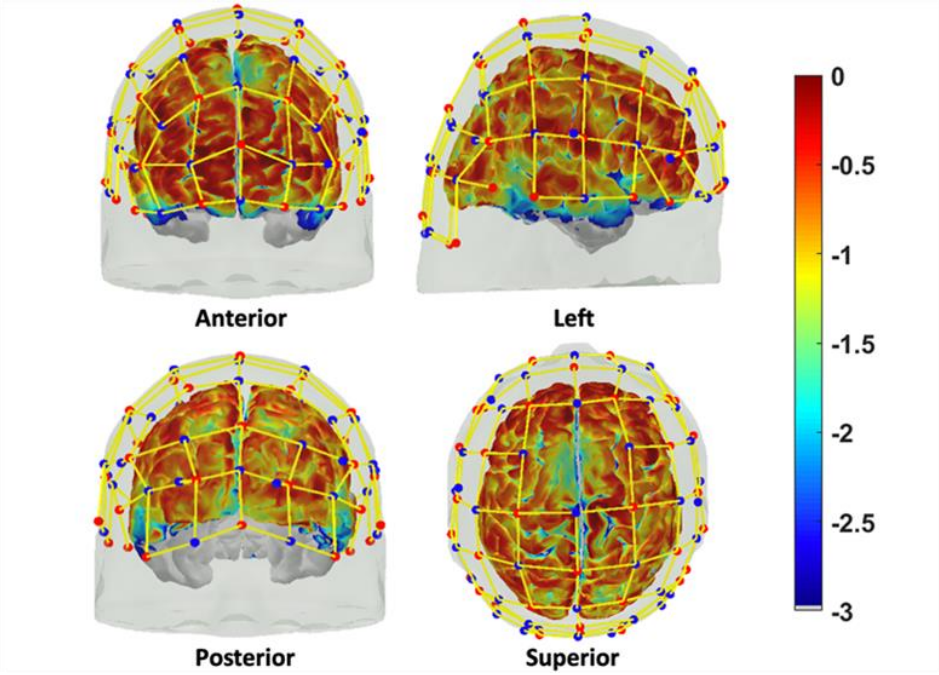

Figure 2-1: fNIRS probe configuration and sensitivity map. Sources (red), detectors (blue) and measurement channels (yellow) are shown on the scalp. The sensitivity profile

of the probe is shown on the cortex. The color scale delineates the sensitivity logarithmically (Zhang et al., 2021).

2.2.3 Experimental Paradigm

Participants were instructed to clench their right hands guided by visual cues at a comfortable sitting position in a dark room. Each participant performed two repeated sessions of clenching at 1 Hz and two sessions of clenching at 2 Hz. Within each session, there was an initial resting period (30 s) followed by six blocks. Each block contained a task period (20 s) and a resting period (30 s). **Figure 2-2** shows the schematic diagram of the experimental paradigm. E-prime (Psychology Software Tools, Sharpsburg, PA) software was used to display instructions and visual cues on the monitor during the experiments.

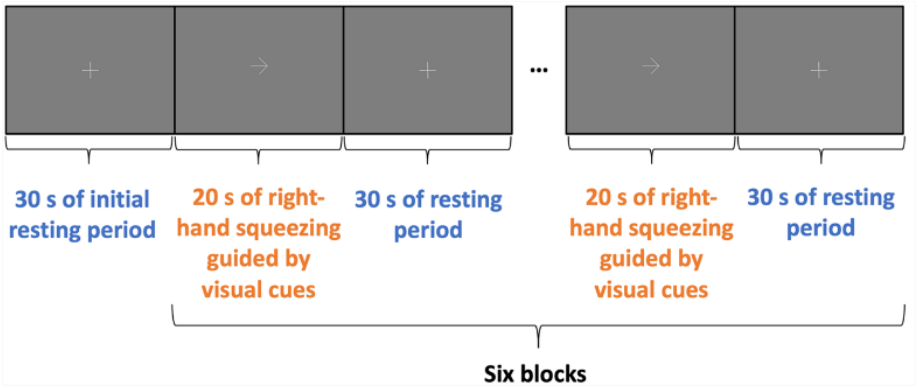

Figure 2-2: The schematic diagram of the experimental paradigm. Each session comprised an initial resting period (30 s) and six blocks. Each block included a task period (20 s) and a resting period (30 s) (Zhang et al., 2021).

2.2.4 fNIRS Data Preprocessing

fNIRS data were automatically preprocessed using proprietary scripts in MATLAB® (The Mathworks, Natick, MA) in conjunction with the HOMER2 toolbox (Huppert et al.,

2009). Specifically, the preprocessing pipeline included: 1) converting raw data to optical density (OD); 2) computing power spectral densities using the Welch's method (a window length of 60 s and 50% overlap) and excluding bad channels that showed no heartbeat frequency peak (0.8 - 1.6 Hz); 3) bandpass filtering OD with 0.008 – 0.2 Hz; 4) converting filtered OD to relative concentration changes of oxy-hemoglobin (ΔHbO) and deoxy-hemoglobin (ΔHbR) based on the modified Beer-Lambert law (MBLL) (Scholkmann et al., 2014). The differential pathlength factors were selected as 7.25 and 6.38 for 760 nm and 850 nm, respectively (Herold et al., 2018). The molar extinction coefficients at 760 and 850 nm were 645.5 cm^{-1}/M and 1097.0 cm^{-1}/M for HbO and 1669.0 cm^{-1}/M and 781.0 cm^{-1}/M for HbR, respectively (Piper et al., 2014).

2.2.5 PCA-GLM Denoising Method

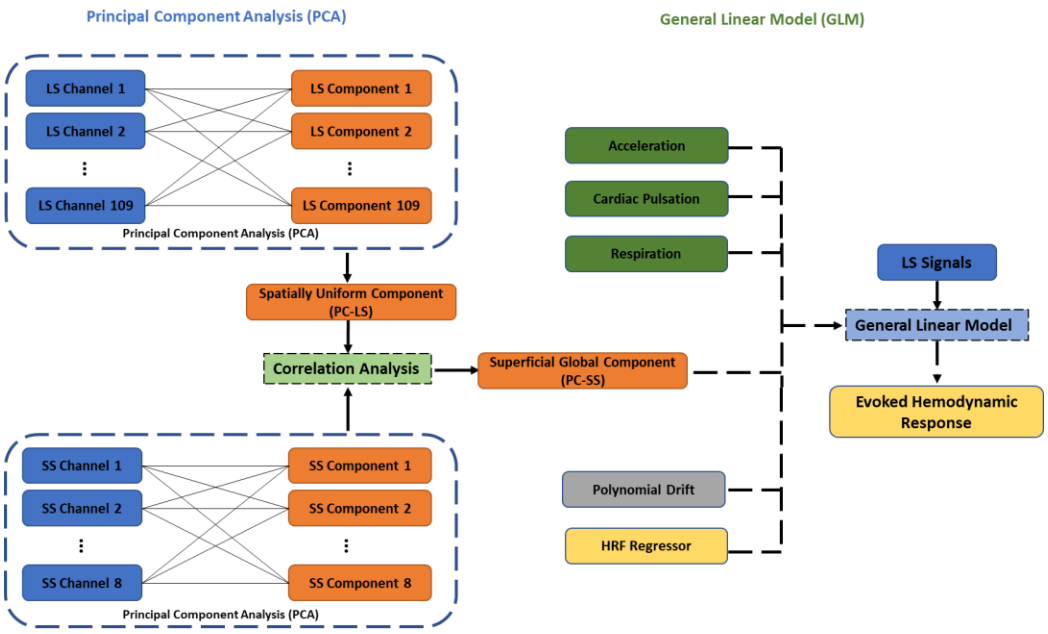

Figure 2-3: The framework of the proposed PCA-GLM method.

After preprocessing of fNIRS data, we developed a novel approach (namely PCA-GLM) to remove the physiological noise by utilizing PCA and GLM based on 109 LS

and 8 SS channels that evenly covered the whole head. The framework of PCA-GLM is illustrated in **Figure 2-3**. Firstly, PCA was applied to LS data to decompose signals into multiple components. Topographic distributions were displayed over whole-head LS channels (**Figure 2-4A**) and assessed by a metric called the coefficient of spatial uniformity (CSU) (Kohno et al., 2007). Because spatial uniformity indicates systemic physiological activity (Zhang et al., 2005), a principal component with the highest value of CSU was identified and named as the spatially uniform component (abbreviated as PC-LS hereafter). After determining the PC-LS component, the time course of PC-LS was not directly removed from the multi-channel LS data; instead, the PC-LS was used to select a component from the SS measurements which are more directly sensitive to the absorption by superficial tissues (Saager and Berger, 2005). Specifically, a total of eight-channel preprocessed SS data were subject to a separate principal component analysis, and the SS component that had the highest temporal correlation with PC-LS was chosen as the superficial global component (abbreviated as PC-SS hereafter). The time course of PC-SS was then used as a nuisance regressor to be removed by GLM. Exemplar time courses of PC-LS and PC-SS are plotted in **Figures 2-4B and C.**

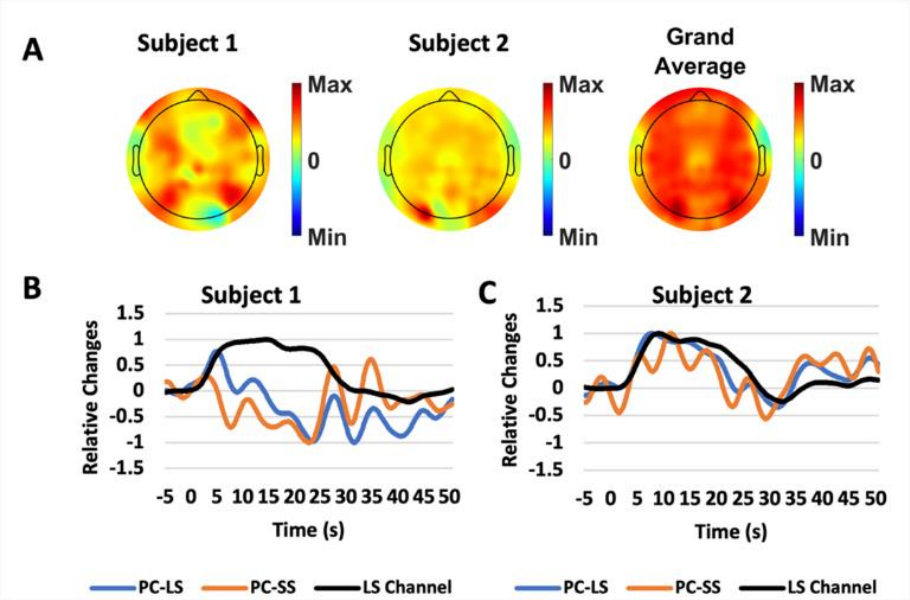

Figure 2-4: (A) The spatial map of PC-LS in two representative subjects and the grand average of all subjects. The spatial map of each session is normalized by its maximum value before it is used to calculate the grand average. (B) and (C) are the exemplar time courses of PC-LS, PC-SS, and from one LS channel over the motor area in Subjects 1 and 2, respectively (Zhang et al., 2021).

A general linear model was configurated for each session to remove physiological noise. Prior to GLM, auxiliary data of acceleration, respiration, and cardiac pulsation were processed by a band-pass filter with 0.008 Hz – 0.2 Hz and further detrended by a 3-order polynomial drift. The time course of PC-SS, the detrended auxiliary data (acceleration, respiration and cardiac pulsation) and a 3-order polynomial drift were included in the design matrix as nuisance regressors. The main effect was accounted for by a hemodynamic response function (HRF) regressor, which was derived by convolving the block design with a canonical two-gamma HRF model (Lindquist et al., 2009). **Figure**

2-5 shows an example of detrended nuisance regressors in a single session together with an HRF predictor.

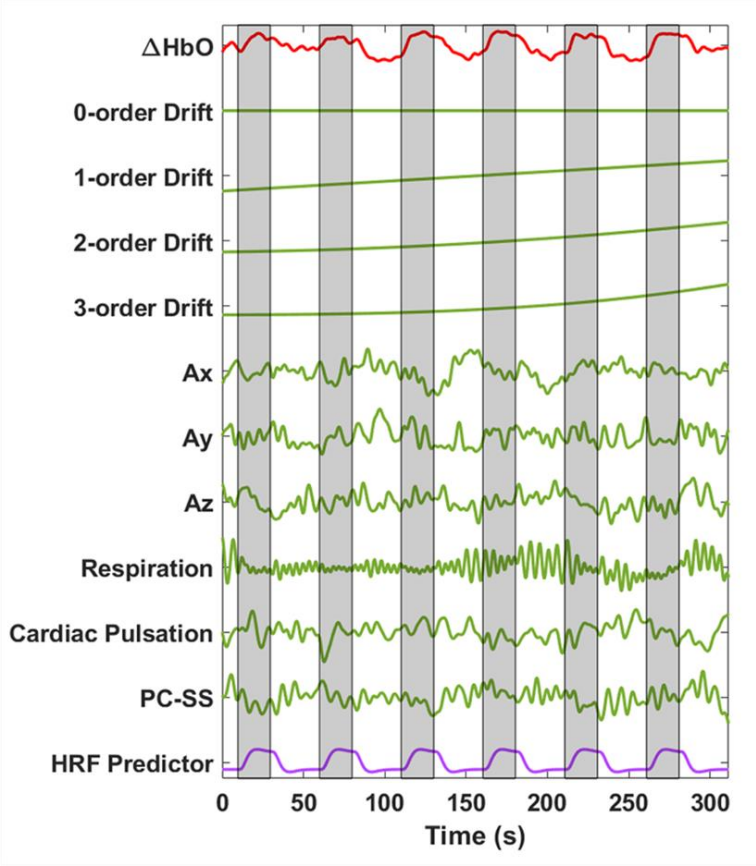

Figure 2-5: Relative concentration changes in a LS channel, 3-order drift, nuisance regressors from auxiliary measurements, the noise component PC-SS, and HRF predictor. Both fNIRS and auxiliary measurements were band-pass filtered with 0.008 to 0.2 Hz. Shaded areas correspond to the task periods (Zhang et al., 2021).

2.2.6 Comparison with Other Denoising Methods

Our proposed PCA-GLM method was compared with four other commonly used preprocessing methods, i.e., a minimal preprocessing of temporal filtering (namely No Correction), the PCA on SS channels (namely Sato method) (Sato et al., 2016), the spatial filtering method (namely PCA) (Huppert et al., 2009; Zhang et al., 2005) and the GLM-

based method that directly regresses the SS from LS recordings (namely SS-GLM) (Gagnon et al., 2011). To implement the PCA method (Zhang et al., 2005), we used the enPCAFilter (nSV = 3) function in Homer2 toolbox (Huppert et al., 2009), which used the entire session of both task and resting data to calculate the PCs. In the SS-GLM method, we used the nearest neighbor SS channel to each LS channel as a regressor representing physiological noise, together with a 3-order polynomial drift and an HRF regressor. In the Sato method, the first PC of SS recordings were used as a nuisance regressor along with a 3-order polynomial drift and an HRF regressor in a general linear model to denoise LS recordings.

To quantify the performance of the proposed PCA-GLM method and three other methods, we evaluated three metrics including contrast-to-noise ratio (CNR), within-subject standard deviation (SD) and adjusted coefficient of determination (adjusted R^2).

(1) The contrast-to-noise ratio (CNR) is calculated as the difference between the mean amplitudes during the task and the rest period normalized by the summation of variances at task and rest periods (Cui et al., 2010; Nguyen et al., 2018; Zhang et al., 2005). The CNR is defined as follows:

$$CNR = \frac{mean(task) - mean(rest)}{\sqrt{var(task) + var(rest)}} \qquad (2.1)$$

where "task" denotes the task period (from 6 s to 16 s), and "rest" denotes the resting period (from -5 s to 0 s) with respect to the onset of each task block (t = 0 s). A high CNR value indicated that the ratio of task-evoked signal to noise is high.

(2) The within-subject standard deviation (SD) (Brigadoi et al., 2014) is calculated as the standard deviation across blocks of a single session when calculating the block averages.

(3) The adjusted coefficient of determination (adjusted R^2) is calculated to evaluate the goodness of fitting by comparing the preprocessed time courses and the task design (Sato et al., 2016). A standard GLM with polynomial drift and HRF regressor was applied to the time courses processed by the No Correction method and those by the PCA method, respectively.

The metrics of CNR, within-subject SD and adjusted R^2 were reported in two representative channels over the motor and visual regions respectively, which were determined by finding the channel that had the highest beta value associated with the task effect in GLM. To assess the performance at a group level, metrics obtained from all subjects were pooled and compared using a two-tailed paired *t*-test with the Benjamini-Hochberg method to correct multiple comparisons (Benjamini and Hochberg, 1995).

2.2.7 Visualization of Task-evoked Activations in Whole-head Recordings

To visualize fNIRS in detecting task-related activations, we calculated time courses of relative changes that are normalized to the variances of task and rest periods, consistent with the definition of contrast-to-noise ratio. Specifically,

$$y_{normalized} = \frac{y - mean(rest)}{\sqrt{var(task) + var(rest)}} \qquad (2.2)$$

where y and $y_{normalized}$ denoted the time courses of a fNIRS channel before and after normalization, "task" denotes the task period (from 6 s to 16 s) and "rest" denotes the resting period (from -5 s to 0 s) with respect to the onset of task blocks (t = 0 s). In each session, the normalized relative changes were segmented into task blocks, aligned at the beginning of task blocks, and then averaged as the block average per session. At the group level, the block averages of all sessions were averaged. Channels representing the contralateral motor cortex, the ipsilateral cortex and the bilateral visual cortex were

illustrated. At the group level, in order to determine whether the activation was significant, a one-sample two-sided *t*-test was performed at each time point across all subjects' sessions, separately for our GLM-PCA method and No Correction method. In addition, a paired two-sample, two-tailed *t*-test was performed to evaluate whether GLM-PCA and No Correction methods yielded different time courses. The resulted *p* values were corrected for multiple comparisons using the Benjamini-Hochberg procedure (Benjamini and Hochberg, 1995).

In addition, to visualize the whole-head topography in detecting task-related activations, a group-level one-sample, two-tailed *t*-test vs. 0 was performed on all channels across all subjects' sessions, based on the beta values associated with the task effect in GLM. The resulted *p* values were corrected for multiple comparisons using the Benjamini-Hochberg procedure (Benjamini and Hochberg, 1995).

2.3 Results

Firstly, a PCA decomposition was performed on the LS recordings and the principle component associated with the highest CSU value (Kohno et al., 2007) was selected as PC-LS. **Figure 2-4A** shows the topographies of the PC-LS in two individual subjects and grand average, respectively. The CSU values corresponding to the exemplar sessions in Subject 1 and Subject 2 are 2.06 and 2.66, respectively. Also, in all individuals, the PC-LS presents a high spatial uniformity with a CSU of 1.74 ± 0.77 (mean ± SD) and ranging from 0.64 to 3.62. The values are consistent with our previous finding (Zhang et al., 2019) and also comparable to those reported in Kohno et al. (2007), despite that in the current study a whole-head montage of more than three times channel numbers was used. Furthermore, we found that the PC-LS accounted for 35.94 ± 18.01 % of the total

variances in long-distance channel data across all sessions. Consistently described in previous fNIRS studies (Zhang et al., 2005), such a component that has a homogenous spatial distribution in regular LS channels is recognized for representing noise originating from superficial skin responses.

Next, a separate PCA decomposition was performed on 8 SS channels that were evenly distributed over the scalp. The principal component derived from SS recordings which has the highest temporal correlation with the time course of previously identified PC-LS was selected as the noise component of all SS data (namely PC-SS). This procedure was operated under the consideration that measurements of multiple LS and SS channels are sensitive to a common physiological noisy component originating from the superficial skin tissues (Saager and Berger, 2005, 2008). Indeed, **Figures 2-4B and C** show representative time courses of PC-LS and PC-SS from two representative subjects. Noteworthy, PC-LS and PC-SS exhibited a similar profile. Across all subjects and sessions, the correlation between PC-LS and PC-SS was 0.67 ± 0.14 (mean $\pm$ SD).

Aside from the temporal similarity between PC-LS and PC-SS, they exhibited important differences. **Figures 2-4B and C** show that PC-SS have more fluctuations in the same time window than the PC-LS, suggesting that PC-SS contains higher frequency oscillations. Furthermore, although PC-LS exhibits a uniform distribution, the PC-LS shows an increase in HbO (and a decrease in HbR, data not shown) during the motor task period, which are similar to the task-related changes in a regular LS channel over the motor area (e.g., the black-colored curves in **Figures 2-4B and C** from the same session). The observation is consistent with previous studies which reported that although PC-LS

captures noise of superficial contributions, it is not free of task-modulated changes (Sato et al., 2016).

Therefore, in order to avoid attenuating the task-related changes in LS channels, our processing pipeline removed the PC-SS rather than the PC-LS. Other nuisance regressors included the auxiliary physiological measurements and 3-order polynomial drift (shown in **Figure 2-5**).

We have applied our proposed method (PCA-GLM) and four established preprocessing methods (i.e., No Correction, PCA, SS-GLM and Sato Method) to the experimental dataset acquired in a group of healthy subjects. Regarding performance metrics of CNR, within-subject SD and adjusted R^2, two-tailed paired-sample *t*-tests were conducted to compare our PCA-GLM method with four other methods. Benjamini-Hochberg method was used to address the multiple comparison problem (Benjamini and Hochberg, 1995). All results shown here were based on HbO contrast unless otherwise specified. **Figure 2-6** demonstrates that our PCA-GLM method improves upon the minimal preprocessing method with no correction of superficial noise, yielding significantly higher CNR, lower within-subject SD and higher R^2 ($q < 0.001$). Compared with three established denoising methods (Sato method, PCA and SS-GLM), our PCA-GLM resulted in the highest CNR and R^2 in both motor and visual channels and significantly outperformed the other methods. In terms of the within-subject SD, PCA-GLM shows good reliability with the lowest value than other methods, except the PCA. However, in the PCA method, the low within-subject SD was accompanied by low CNR and low adjusted R^2, which were attributed to the overall small magnitudes of time courses after removing excessive components.

Noteworthy, our PCA-GLM method is completely automatic, including the determination of PC-LS and PC-SS as well we as the GLM regression. In the four other methods that were compared, the PCA filtering method was configurated to be automatic by mandating a fixed number of components to be removed (n = 3).

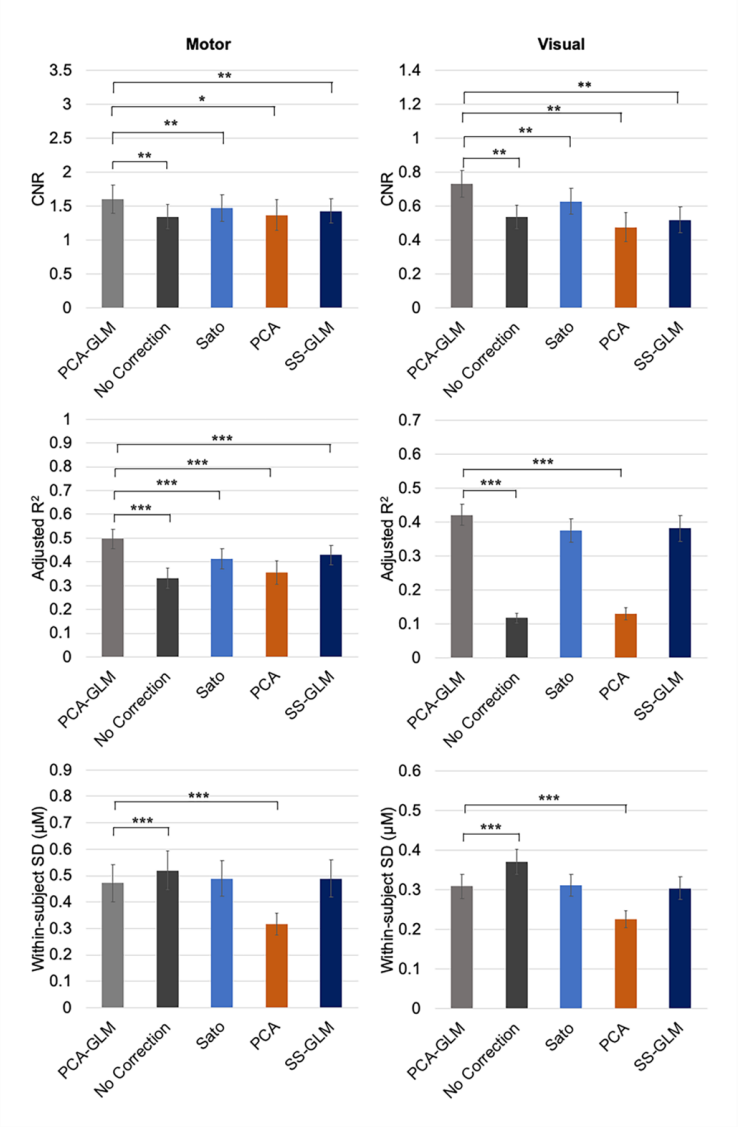

Figure 2-6: Comparison of denoising performance. CNR, adjusted R^2 and within-subject SD in HbO of the motor channel (left column) and visual channel (right column) were compared between PCA-GLM and No Correction, Sato method, PCA or SS-GLM. The asterisks above lines indicate statistically significant differences between different

methods (* $q < 0.05$, ** $q < 0.01$, *** $q < 0.001$, after applying Benjamini-Hochberg method). The error bars indicate the standard errors across sessions (Zhang et al., 2021).

Figure 2-7 shows the automatic denoising outcomes in a representative subject (Subject 1) by applying our PCA-GLM method in a total of 109 long-channel recordings that covered the whole head. As our study used a visually cued motor task, activations in both the motor and visual areas were expected. Whole-head topographies of HbO activations across 5 to 15 s in the single trials and block averages of the normalized relative changes are shown in **Figure 2-7A**. In addition, the single-trial and block-average time courses of the normalized relative changes from selected channels in the motor and visual areas are illustrated in **Figure 2-7B**. After processing by PCA-GLM, a strong and focal activation in the contralateral motor area became evident in both the single-trial and the block-average topography. Other identified areas included the ipsilateral sensorimotor area with a focus shifted towards the posterior direction than the contralateral motor area, as well as the bilateral visual area that appeared to be symmetrically activated. In the time courses of single trials and block averages, the PCA-GLM yielded an overall stronger activation in ΔHbO during the task durations, compared with the minimal processing.

Group results across all subjects are shown in **Figure 2-8**. The grand average of ΔHbO time courses from the motor and visual areas is shown in **Figure 2-8A**. In multiple channels over the contralateral motor cortex, ipsilateral sensorimotor cortex and bilateral visual cortices, significant activations during the tasks were detected by our PCA-GLM method (**Figure 2-8A**). Compared with the results from minimal processing with no correction of SS channels, our method yielded a higher magnitude of HbO increases during the task periods and more time points with significant activations from rest periods

(q < 0.05, multiple comparisons corrected), which is consistent with a group-level increase of CNR (**Figure 2-6A**). A group-level topography of activations is shown in **Figure 2-8B**. A *t*-test on the task-association effect revealed significant activations in the channels from the contralateral motor, the ipsilateral premotor, and the bilateral visual areas (q < 0.05, after applying the Benjamini-Hochberg method with a false discovery rate of 0.05).

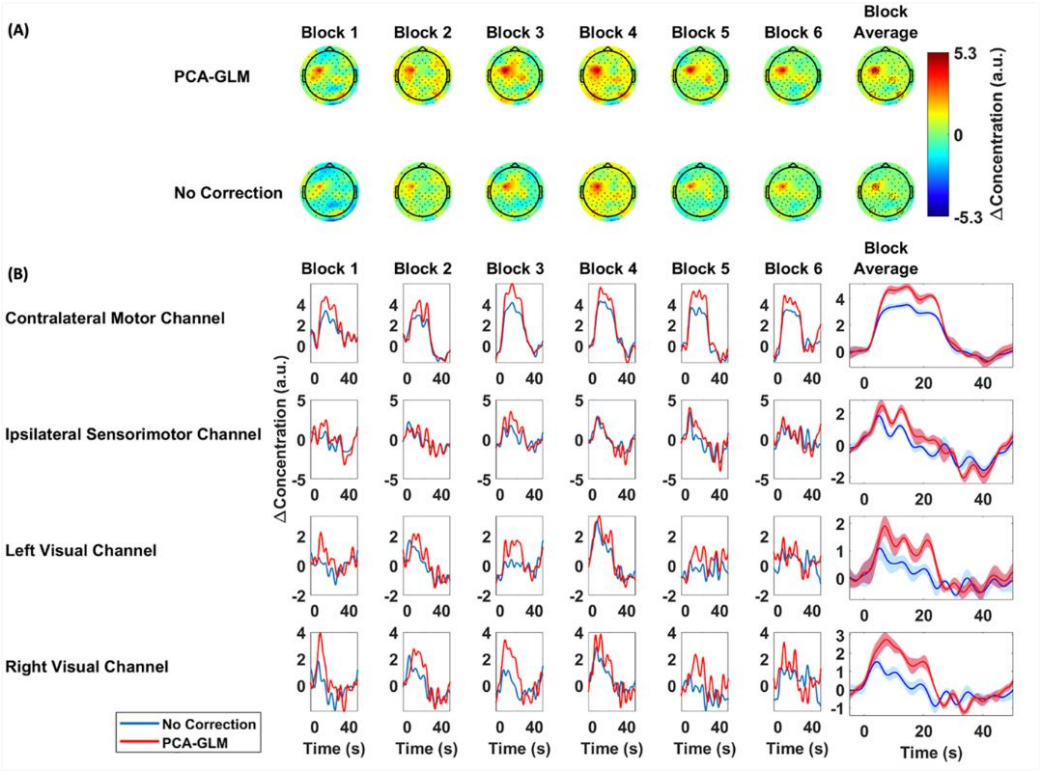

Figure 2-7: Sing-trial and block-average data show concurrent activations in motor and visual areas during the task period in Subject 1. (A) Topographies of the mean amplitudes across 5 to 15 s of the single trials and block averages of all LS channels after PCA-GLM and No Correction. The dash circles label the motor and visual channels, of which the block averages are shown below. (B) Single-trial time courses and their block averages in motor and visual channels after PCA-GLM and No Correction in the same subject. The

line and shaded area represent the mean and standard error across blocks, respectively (Zhang et al., 2021).

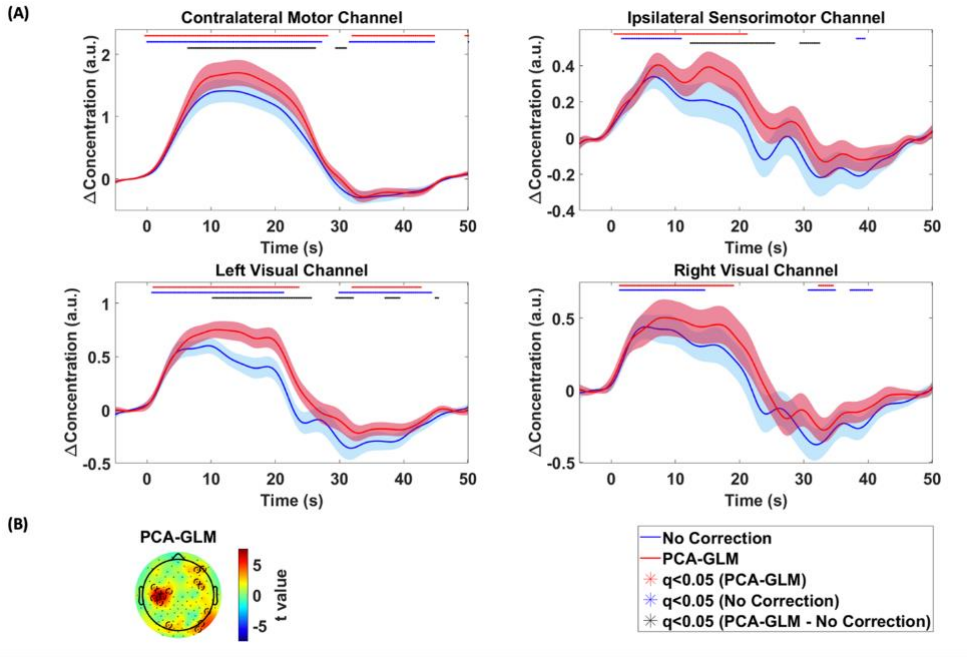

Figure 2-8: Group-level results show concurrent activations in motor and visual areas during the task period. (A) Grand average of block averages in motor and visual channels produced by PCA-GLM and No Correction methods. The solid lines and shaded areas represent the mean and standard error across sessions, respectively. The red and blue asterisks indicate the time points with significant activations ($q < 0.05$ after Benjamini-Hochberg correction) for the block averages by PCA-GLM and No Correction, respectively. The dark asterisk indicates the time points with significant differences between PCA-GLM and No Correction against 0 ($q < 0.05$ after Benjamini-Hochberg correction). (B) Topography of group-level activations associated with the task. The shown t-values were from the *t*-test across all subjects. The dash circles indicate the LS

channels that were significantly activated ($q < 0.05$ after Benjamini-Hochberg correction) (Zhang et al., 2021).

2.4 Discussions

fNIRS has seen rapid development and increasing use in studying the human brain under normal and diseased conditions (Chen et al., 2020b; Pinti et al., 2018; Wheelock et al., 2019). However, fNIRS suffers from its susceptibility to the superficial tissues and systemic physiological noise associated with the cardiac pulse, respiration and movement (Kirilina et al., 2013; Schecklmann et al., 2017; Tong et al., 2011). The presence of physiological noise confounds the accuracy of fNIRS for monitoring brain activation, with false positive and false negative results in images (Tachtsidis and Scholkmann, 2016). Therefore, in order to tap the full potential of fNIRS, it is essential to correct these confounding factors from fNIRS signals.

In this chapter, we proposed a novel denoising method namely PCA-GLM for whole-head fNIRS recordings. Our method was applicable and effective in a montage of 109 LS and 8 SS channels that evenly covered the scalp. To our knowledge, our study is the first to report a preprocessing method that integrates Long- and Short-separation channels and auxiliary measurements to improve fNIRS signals in a whole-head montage. Especially, our study has evaluated the proposed preprocessing method in a complex task and for the first time reported effective denoising outcome of concurrent visual and motor activations in a whole-head montage. Results demonstrated that, during the task-on periods of a visually cued motor task, oxyhemoglobin activity in the contralateral primary motor, ipsilateral premotor/sensorimotor, and bilateral primary visual areas were increased relative to the task-off period (shown in **Figures 2-7 and 2-8**). Because subjects

performed hand clenching with visual cues in the task-on blocks and rested with a grey screen in the task-off blocks, concurrent activations in the motor and visual areas were consistent with subjects' behavior. This finding of contralateral activation in primary motor and ipsilateral activation in sensorimotor areas is in agreement with the hemodynamic response previously observed in fNIRS (Franceschini et al., 2003; Franceschini et al., 2006; Huppert et al., 2006; Leff et al., 2011) and fMRI studies (Huppert et al., 2006; Yuan et al., 2010; Yuan et al., 2011). In addition, activation in the primary visual cortex is also consistent with the previous report of fNIRS covering the visual regions (Chen et al., 2015; Franceschini et al., 2006; Jasdzewski et al., 2003; Liao et al., 2010; Obrig et al., 2002; Putze et al., 2014). Importantly, our study using a whole-head montage has reported concurrent activations in channels over different and distant brain lobes, i.e., motor and visual activations in a visuomotor task.

In order to remove the confounding physiological noise in fNIRS, our study utilized several auxiliary sensors in addition to the whole-head fNIRS, including multiple SS channels to capture superficial signals and auxiliary measurements of acceleration, respiration and cardiac pulsation. Based on these physiological measurements, we proposed a novel way of integrating two-step PCA and GLM to remove the systematic noise embedded in regular LS channels. We have evaluated the denoising performance of our method with four other commonly used methods for processing fNIRS signals, including the minimal preprocessing with no correction of superficial signals, PCA-based spatial filtering (Zhang et al. 2005; Huppert et al., 2009), GLM with SS channels (Gagnon et al., 2011) and the Sato method that combined PCA and SS channels (Sato et al., 2016). Although many studies so far have evaluated various fNIRS methods in denoising

performance (Pinti et al., 2018; Santosa et al., 2020; Sato et al., 2016; von Lühmann et al., 2020; Wyser et al., 2020; Zhang et al., 2009; Zhang et al., 2015; Zhang et al., 2005), the data used in those studies (including synthetic data) only contains a partial montage of the head, e.g., covering only the motor cortices (Gagnon et al., 2011; Santosa et al., 2020; Sato et al., 2016; Wyser et al., 2020; Zhang et al., 2005), prefrontal cortex (Dong and Jeong, 2018; Pinti et al., 2018), or visual cortex (von Lühmann et al., 2019; Zhang et al., 2009; Zhang et al., 2015). When evaluating these methods, experimental data or synthetic data with one focal activation are commonly used, event at a wide montage (Noah et al., 2021; Zhang et al., 2016). Importantly, our study has extended the algorithms of PCA, SS-GLM and the Sato method to a much larger set of channels evenly covering the whole head and compared the denoising performance with our PCA-GLM method. Since PCA filtering and the Sato method reply on a homogenous global pattern in capturing superficial noise, their performance at whole-head montage was not guaranteed, considering that emerging evidence has suggested the contributors to physiological noise are heterogenous rather than homogenous (Erdogan et al., 2014; Kirilina et al., 2012; Schecklmann et al., 2017; Sutoko et al., 2019; Wyser et al., 2020). In the meanwhile, although SS-GLM allows heterogeneous SS signals in the denoising scheme, the direct removal of SS time series may reduce the effect size in regular LS fNIRS signals, since the task-related activity is still detectable in superficial signals – therefore the denoising performance of SS-GLM at whole-head montage remained unknown. Evaluation of our proposed method and four other common methods showed that PCA-GLM resulted in superior CNR, within-subject SD and adjusted R^2 in experimental whole-head recordings from a visually cued motor task. The CNR and

adjusted R^2 yielded by our PCA-GLM method was the highest among all methods in both motor and visual channels, and significantly outperformed all other methods. The superior performance of CNR indicates that our denoising method is valid and can improve the capability of fNIRS in detecting cerebral activations by effectively removing physiological noise. Furthermore, the experimental validation of concurrent motor and visual activity in our study suggests the feasibility of fNIRS in imaging large-scale neural networks in human subjects, such as the default mode network and attention network, which are composed of multiple nodes in distant lobes and are implicated in many neurological and neuropsychiatric diseases (Aihara et al., 2020; Duan et al., 2012; Li et al., 2018; Lu et al., 2010; Zhang et al., 2010).

Another benefit of removing physiological noise is the increased reliability in fNIRS signals, which is evidenced by the smaller within-subject SD of our PCA-GLM method as compared with the No Correction ($q < 0.001$ for both motor and visual channels), SS-GLM ($q = 0.07$ for the motor channel) and Sato Method ($q = 0.07$ for the motor channel), except for the PCA method. However, in the PCA method, the low within-subject SD was accompanied by low CNR and low adjusted R^2, which were overall attributed to the small magnitudes of time courses after removing excessive components. The time courses of tasks have further shown that our method could yield more data points with activations and yield significantly stronger activations at sensorimotor and visual cortices, compared with No Correction (**Figure 2-8**). Furthermore, single-trial time courses processed by our method have shown prominent task-engaged activations in both the motor and visual channels (**Figure 2-7B**), especially with higher and detectable amplitudes than the resting period. These findings further suggest that the fNIRS might be applicable in brain-

computer interface studies that rely on the detection of single-trial activity (Coyle et al., 2007; Hong et al., 2015; Naseer and Hong, 2015). Because fNIRS is noninvasive, portable and robust to head movement (Carius et al., 2016; Herold et al., 2018; Perrey, 2008), it offers a complementary advantage as a sensing modality for developing neural interfaces (He et al., 2020).

Noteworthy, our denoising method is implemented as an automated pipeline for whole-head fNIRS recordings. Previously, studies employing PCA or ICA for denoising fNIRS data have relied on manual criteria, either choosing noisy components by visual inspection or manually setting a certain threshold to determine noise components. However, in our proposed PCA-GLM method, the selection of the noise component in the LS channels is automatically determined by choosing the SS component that resembles the LS component in the highest temporal correlation. Therefore, with the formulation of nuisance regressors, the entire preprocessing pipeline becomes automatic, which enables efficient batch processing in clinical applications of fNIRS.

In comparing our method with other commonly used methods, our PCA-GLM method contains a two-step PCA approach to derive the noise component, which differs from existing methods that performed PCA only on the LS channels (Zhang et al., 2005), or only on the LS channel (Sato et al., 2016). Previously, PCA-based filtering has been exploited to remove the global hemodynamic component by decomposing regular LS recordings only. However, without directly measuring superficial signals from SS channels, the decomposed components from LS data alone are insufficient in delineating the noise contribution. As shown in **Figures 2-4B and C**, the time courses of PC-LS exhibited a task-alike modulation, in a very similar manner to the LS channel of interest

located over the motor area. Therefore, directly removing a PC-LS that carries a task effect will attenuate the effect size in these PCA filter methods. Similarly, a single SS channel which is located near the LS channel might also carry the task effect. Therefore, in our developed method, we used PC-SS as a regressor to regress the physiological and superficial noise from fNIRS signals. Our method derived the noisy component via PCA on a total of eight SS channels evenly distributed over the scalp, motivated by our previous findings that PC-SS exhibits a high correlation with PC-LS and that PC-SS is primarily contributed by superficial noise (Zhang et al., 2019). Therefore, the PC-SS was removed, rather than PC-LS or a single SS channel, which yielded a significantly improved CNR, as shown in **Figure 2-6**.

In the current study, our method removes one noise component that is spatially uniform and commonly reflected in LS and SS measurements (CSU of PC-LS is 1.74 ± 0.77; the temporal correlation between PC-LS and PC-SS is 0.67 ± 0.14), which has a reliable origin from superficial noise (Kohno et al., 2007; Tong, 2010; Zhang et al., 2005). Importantly, our method has developed a framework where more than one noise component from the whole-head LS and SS recordings can be derived and removed, such as originating from temporal muscles. However, future studies are warranted to validate the origins of additional noise components.

Furthermore, our study utilized auxiliary recordings of pulse, respiration and movement. These additional nuisance regressors address the slow fluctuations in pulses, respiration and movement. Results in **Figure 2-9** demonstrated the benefit of including the auxiliary data in our PCA-GLM method, resulting in higher CNR, better fitting and lower variance. Notably, this benefit of denoising was achieved by including zero-shift

time courses of auxiliary measurement, although studies have shown that a time-embedding approach (von Lühmann et al., 2020) or considering a response function to the respiration (Birn et al., 2008) or cardiac pulses (Chang et al., 2009) might further capture their impact on cerebral hemodynamics. While these fluctuations are typical of less concern to a task in block design, they have been suggested to bias the organization of large-scale networks, especially in the resting brain (Mesquita et al., 2010; Yuan et al., 2013).

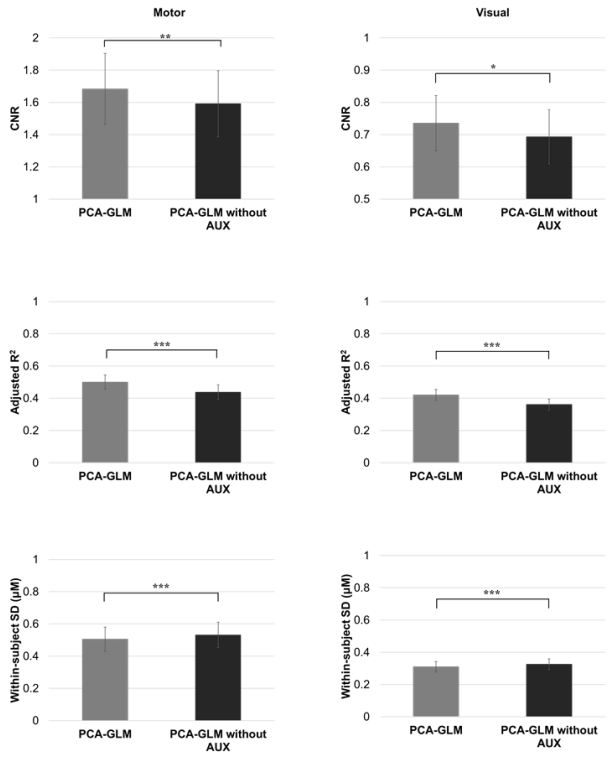

Figure 2-9: Comparison of denoising performance. CNR, within-subject SD and adjusted R^2 in HbO of the motor channel (left column) and visual channel (right column) were compared between PCA-GLM and PCA-GLM without auxiliary measurements. The asterisks above lines indicate statistically significant differences between methods (* $p < 0.05$, ** $p < 0.01$, *** $p < 0.001$) (Zhang et al., 2021).

2.5 Conclusions

In summary, we have developed a novel denoising method to remove the physiological noise in whole-head fNIRS recordings. Our approach of identifying and removing noise based on long- and short-separation channels and auxiliary measurements is completely automatic without manual maneuver. The results demonstrated that the proposed pipeline is capable of detecting concurrent and distant brain activations in a whole-head fNIRS montage, with improvements in detectability and reliability upon established methods. The results suggest that our denoising method for whole-head fNIRS can accelerate the usage of fNIRS in neuroscience research and clinical care, especially in studying large-scale brain networks in normal and diseased conditions.

3 Chapter 3 Network Organization of Resting-State Cerebral Hemodynamics and Their Aliasing Contributions Measured by fNIRS

3.1 Introduction

The brain remains remarkably active in the absence of explicit inputs (Shulman et al., 2004). Since the early discovery that the hemodynamic oscillations in the functional magnetic resonance imaging (fMRI) data are temporally correlated at a resting state (Biswal et al., 1995), a great deal of efforts has been dedicated to understanding these correlations as resting-state functional connectivity (RSFC) in studying human brain function and organization (Fox and Raichle, 2007). For example, a widely-investigated default mode network (DMN) is described as a network organization of correlated activity in medial prefrontal cortex, posterior cingulate cortex/precuneus, inferior parietal lobule, lateral temporal cortex (Buckner et al., 2008). Then the altered functional connectivity between anterior and posterior midline structures of DMN is found to be related to cognitive function and has further been postulated as a hallmark of the aging process (Andrews-Hanna et al., 2007) and Alzheimer's Disease (AD) (Greicius et al., 2004; Jones et al., 2016). The fMRI, alone or combined with electroencephalogram (EEG) or magnetoencephalography (MEG) for better temporal resolution (Brookes et al., 2011; Yuan et al., 2016; Yuan et al., 2012), has become the main tool for characterizing the functional organization of the human brain in healthy conditions, aging and developmental processes, and neurological disorders (Zhang and Raichle, 2010).

Recently, an optics-based modality to noninvasively measure hemodynamics in the human brain - functional near-infrared spectroscopy (fNIRS) - has shown tremendous

potential in studying RSFC (Chen et al., 2020b; Lu et al., 2010; White et al., 2009; Zhang et al., 2010). fNIRS offers better cost-effectiveness, portability, and compatibility with electromagnetic devices (Chiarelli et al., 2017; Hu et al., 2020; Naseer and Hong, 2015; Scholkmann et al., 2014). Considering the overwhelming number of people that are projected to be with AD and an even larger number to be placed at the prevention and intervention stages (Sperling et al., 2014), a broadly accessible instrument is especially welcomed in tracking the aging trajectory of brain functions and network organization (Chen et al., 2022). Whole-head and cap-based fNIRS recordings have become available with diffuse optical tomography (DOT) to reconstruct the voxel-wise activity (Chen et al., 2020c; Khan et al., 2021; Zhang et al., 2021), yet RSFC of a complete DMN has not been fully revealed and benchmarked to that in fMRI (Aihara et al., 2020; Eggebrecht et al., 2014).

In addition, fNIRS offers a high temporal resolution, typically at the rate of 2-10 Hz (Chen et al., 2020c; Eggebrecht et al., 2014; Zhang et al., 2021), which is higher than a typical fMRI whole-brain scan of 0.5 Hz (Andrews-Hanna et al., 2007; Yeo et al., 2011). Despite the intrinsic oscillations of the vascular networks (Drew et al., 2020; Mateo et al., 2017) and other physiological oscillations such as respiration, cardiac pulsation and cerebrospinal fluid which may also contribute to the measured hemodynamics in the upper frequencies (Liu, 2016), our understanding of the human brain functional connectivity has been primarily established by fMRI at sub-hertz sampling rates for the activity below 0.1 Hz (Biswal et al., 1996; Cordes et al., 2001; Mitra et al., 1997). Since hemodynamics is resulted from the interplay between local neuronal activity, oxygen consumption, and vascular circulation (Buxton, 2013; Logothetis, 2008), it is unknown

how the oscillations that exist beyond those safely sampled ranges could contribute to the network organization via the aliased activity.

In this study, we used a whole-head, cap-based and high-density fNIRS instrument to measure oxyhemoglobin (HbO) and deoxyhemoglobin (HbR) at the sampling frequency of 6.25 Hz. We benchmarked fNIRS in imaging DMN with that obtained from fMRI. By computing DOT based on individuals' realistic anatomy, we have mapped the network at a fine voxel resolution, demonstrating high similarity with fMRI in a common cortical space. Furthermore, we deliberately down-sampled the raw optical recordings to a sub-hertz temporal resolution and have found altered connectivity in the ultra-slow frequency range, giving rise to a set of aliased functional connectivity patterns (AFCPs) that may obscure our interpretation of RSFC.

3.2 Methods

3.2.1 Participants

The study was approved by the University of Oklahoma Health Sciences Center Institutional Review Board. Written consent was obtained from all participants prior to the study. All procedures were carried out in accordance with the IRB guidelines. A total of 20 healthy participants without any neurological or neuropsychiatric disorders were screened and enrolled in this study. Three participants were not able to complete all data recordings. In addition, resting-state data from four participants were excluded from the present study due to poor data quality (primarily excessive motions). Therefore, data from thirteen participants (5 females, 31.7 ± 9.3 years old) were used for the analyses. Participants received financial compensation for their participation.

3.2.2 Data Acquisition

Blood-oxygenation-level-dependent (BOLD) fMRI data and fNIRS-EEG data were acquired from each participant in two separate visits. Structural head MRI and fMRI images of participants were acquired using a GE Discovery MR750 whole-body 3-Tesla MRI scanner (GE Health, Milwaukee, WI, USA). The following parameters were used for MRI scanning: FOV = 240 mm, axial slices per slab = 180, slice thickness = 1 mm, image matrix = 256 × 256, TR/TE = 8.45/3.24 ms. The following parameters were used for fMRI scanning: FOV = 240 mm, axial slices per slab = 41, slice thickness = 4 mm, image matrix = 64 × 64, TR/TE = 2600/60 ms. fMRI data were recorded when participants rested in a supine position inside the scanner with their eyes opened. One 6-minute resting session per participant was included for the fMRI.

Simultaneous fNIRS, EEG (not analyzed in this study) and peripheral measurements of respiration, pulse, and triaxial acceleration were recorded, following the protocol described in our previous publication (Zhang et al., 2021). Two 6-minute recording sessions of eyes-open resting state were acquired per each participant who comfortably sit in a dark and sound-damped room.

3.2.3 fNIRS Data Preprocessing

fNIRS data were automatically preprocessed by adapting our previously developed automatic denoising procedure, namely principal-component-analysis-based general linear model (PCA-GLM) (Zhang et al., 2021). As illustrated in **Figure 2-3**, the preprocessing pipeline included these steps: 1) converting raw data to optical density (OD); 2) computing power spectral densities using the Welch's method (a window length of 60 s and 50% overlap) and excluding bad channels that showed no heartbeat frequency

peak (0.8 - 1.6 Hz); 3) bandpass filtering OD with 0.008 – 0.2 Hz; 4) identifying and rejecting bad time segments with excessive head movements using the metric of global variance in temporal derivative (GVTD) (Sherafati et al., 2020). The time points that had GVTD values larger than three times the mean GVTD value across all time points were identified, and then time windows of 10 s centered at these time points were masked as bad time segments and excluded from further analyses (Sherafati et al., 2020). 5) Although fNIRS has its intrinsic advantage of high sampling frequency, interferences from auto-regulation in the vasculature and other physiological sources occur at various frequencies (White et al., 2009). By employing eight SS channels that have minimal penetration into the cortical tissue, we measured the superficial hemodynamics in the scalp and used that combined with LS channels to construct a superficial signal regressor, which was then removed as one of the nuisances. Specifically, PCA was applied to LS OD data to decompose signals into multiple components. The spatial uniformity of each principal component was assessed by the metric of coefficient of spatial uniformity (Kohno et al., 2007). Because spatial uniformity indicates superficial skin responses (Zhang et al., 2005), a principal component with the highest value of spatial uniformity was identified, namely PC-LS. Then, instead of directly removing the time course of PC-LS from the multi-channel data, the PC-LS was used to select a component from the SS measurements which capture the absorption by superficial tissues (Saager and Berger, 2005). A total of eight, evenly distributed SS OD data were subject to a separate PCA, and the SS component that had the highest temporal correlation with PC-LS was chosen, representing the skin response. The selected SS component was then used as a nuisance regressor to be removed by GLM. 6) A general linear model was configurated per each

session to remove physiological noise. Prior to GLM, auxiliary data of acceleration, respiration, cardiac pulsation were processed by a band-pass filter with 0.008 Hz – 0.2 Hz and further detrended by a 3-order polynomial drift. The time course of the SS component, the detrended auxiliary data (acceleration, respiration and cardiac pulsation) and a 3-order polynomial drift were included in the design matrix as nuisance regressors.

In addition, to investigate the effect of a low sampling rate on the functional connectivity, we have re-sampled the fNIRS data (originally acquired at 6.25 Hz) by a decimation ratio of 13, resulting in a sampling rate of 0.48 Hz. The down-sampled fNIRS data were preprocessed using the same procedure.

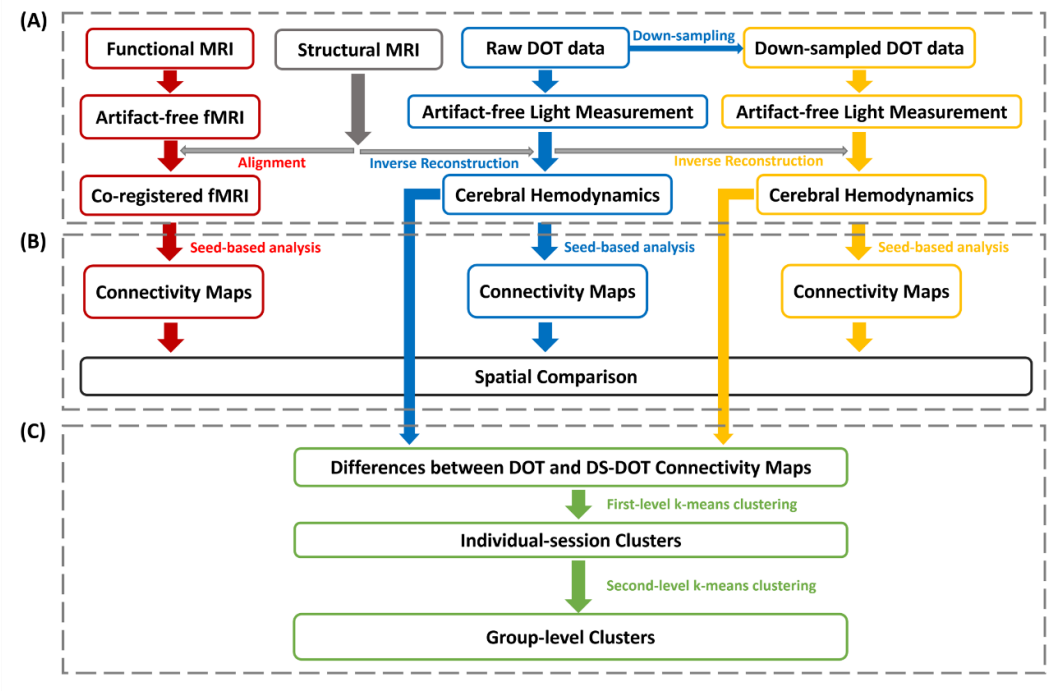

Figure 3-1: Schematic framework of computations. (A) Data preprocessing of fMRI, fNIRS and down-sampled fNIRS data. (B) Seed-based functional connectivity analyses. (C) K-means clustering on the differential functional connectivity maps between DOT and down-sampled DOT.

3.2.4 Diffuse Optical Tomography Reconstruction

Participant-specific structural MRI data were used to create individual finite element method (FEM) volume meshes (Khan et al., 2021). A spectrally-constrained linear FEM-based forward model (Srinivasan et al., 2005) linking hemodynamic responses $\vec{x}(t)$ and scalp-based light measurements $\vec{y}(t)$ was established as:

$$\vec{y}(t) = A\vec{x}(t) \qquad (3.1)$$

where the sensitivity matrix A was calculated using the NIRFAST software (Dehghani et al., 2009). The volumetric inverse source space was constructed with nodes inside the brain (enclosed by the pial surface) and no deeper than 45 mm from the scalp, beyond which the sensitivity had dramatically decreased. A single-step joint inverse reconstruction using regularized minimum norm estimate (Bertero et al., 1988) yielded the volumetric inverse solution data $\vec{x}(t)$. The inverse data were first smoothed with a 6 mm spherical kernel and then projected to the fsaverage5 smoothed white matter surface from FREESURFER (Fischl, 2012; Ségonne et al., 2004). The projection was performed by assigning the data to each node on the cortical surface from the nearest finite element node in terms of Euclidean distance. Both cortical data of HbO and HbR concentration changes were reconstructed. Because the deoxygenated status reflected in HbR is a direct approximation to the T2* contrast in fMRI (Ogawa et al., 1990), HbR was primarily used in the further analysis of this study for the benchmark purpose. Tomography for the down-sampled fNIRS data was computed in the same procedure, resulting in down-sampled DOT (DS-DOT).

3.2.5 fMRI Data Preprocessing

For the purpose of cross-modal validation, we have also collected resting-state fMRI data in the same group of participants. The fMRI data processing was performed using Analysis of Functional NeuroImages software (AFNI, http://afni.nimh.nig.gov/) (Cox, 1996). The first five volumes of each fMRI run were excluded from the analysis to allow the BOLD signal to reach a steady state. The fMRI then went through these processing steps including slice timing and rigid-body motion correction, spatial smoothing with a Gaussian kernel with a full width at half maximum (FWHM) of 13 mm, and a bandpass filtering (0.009-0.08 Hz). Notably, the 13-mm FWHM was considered to match up with that in DOT. In addition, six affine motion parameters and the global signal from the entire brain were regressed out from the dataset. Data points of excessive motion (root mean square larger than 0.2 mm) were excluded from regression and further analysis using the *censoring* option implemented in AFNI (afni_proc.py). The threshold of 0.2 mm was suggested by Power and colleagues (Power et al., 2013). Specifically, the L2-norm of the derivatives of the motion parameters estimated from motion registration was calculated and those time points with an L2-norm larger than the threshold of 0.2 mm were censored/excluded in the regression and the later functional connectivity analysis. The fMRI data of each participant were firstly spatially co-registered to high-resolution individual anatomical images and then normalized to the Talairach and Tournoux template brain (Talairach and Tournoux, 1988).

3.2.6 Seed-based Mapping of Resting-state Functional Connectivity

After preprocessing, seed-based mapping of functional connectivity was performed in fMRI, DOT and DS-DOT by calculating the Pearson's correlation coefficients between

the average time course of a seed region with a radius of 10 mm and the time courses of other nodes (Power et al., 2011). In order to study the functional connectivity maps of DMN, we considered the key nodes of DMN as the seed regions, including medial prefrontal cortex (mPFC), inferior parietal lobe (IPL), precuneus and a compound seed (the average of mPFC, IPL, and precuneus). **Table 3-1** lists the coordinates of the seeds.

For fMRI data, the correlation values were first subject to Fisher's Z transform. For the cross-modal evaluation, we projected the functional connectivity to a common space of the cortical surface. Specifically, the individual-level volumetric Z maps were projected to the fsaverage5 smoothed white matter surface with 10,242 vertices per hemisphere (Fischl et al., 1999) using the *3dVol2Surf* in AFNI. The individual-level Z maps in the surface space were then averaged to obtain the group-level connectivity map and subject to node-wise one-sample two-tailed Student's t-tests to assess the significance of functional connectivity.

Table 3-1: The coordinates of seeds for the resting-state functional connectivity maps. All numbers are in MNI coordinates. Identical seeds are used for fNIRS and fMRI maps.

	Left hemisphere			Right hemisphere		
	x	y	z	x	y	z
mPFC	-8.4	51.5	14.9	8.7	52.4	15.1
IPL	-39.5	-57.0	40.7	39.0	-55.9	42.6
Precuneus	-6.5	-64.5	39.8	6.6	-62.5	39.6

For DOT and DS-DOT data, the global signal was first calculated by averaging the time traces of all nodes over the cortical surface and regressed out from the time traces of individual cortical nodes (Desjardins et al., 2001). The seed-based correlation analysis was then calculated in the surface space. The individual maps of Pearson's correlation coefficients were subject to Fisher's Z transform and smoothed with a Gaussian kernel with FWHM of 13 mm using the mri_surf2surf in FreeSurfer (Dale et al., 1999). The smoothed individual-level Z surface maps were then averaged to obtain the group-level connectivity map.

The similarity between the DOT and fMRI functional connectivity was quantitatively evaluated by spatial correlation and dice coefficient (Eggebrecht et al., 2014; Yuan et al., 2016). The spatial correlation was calculated for the unthresholded DOT and fMRI functional connectivity maps with the same seed. The dice coefficient was calculated for the binary DOT and fMRI maps (1 for a significant p-value after multiple comparisons correction).

3.2.7 Aliased Functional Connectivity Patterns

To study the effect of aliased sampling on the RSFC, we have down-sampled the fNIRS data at the rate of 0.48 Hz. After identical procedures of preprocessing and tomography projection, including additional band-pass filtering of 0.009 Hz – 0.08 Hz that is commonly used in fMRI RSFC analysis, functional connectivity maps were created based on DOT and DS-DOT, respectively. Differential connectivity maps were calculated by subtracting the DOT connectivity maps from the DS-DOT connectivity maps. Since aliased activity led to aliased connectivity maps, we explored whether any structural organization exists in these differential connectivity maps. Because the study is primarily

interested in examining whether the DMN was in any way affected by an insufficient sampling rate, we used a data-driven approach to search for organized patterns among all the differential maps associated with nodes in the DMN. A two-level k-means clustering was performed to classify the differential functional connectivity maps based on their spatial similarities (Britz et al., 2010; Michel and Koenig, 2018). At each level, the clustering was repeated 100 times to increase the chances of escaping local minima, with randomly initialized centroid positions (Allen et al., 2014). In terms of the distance measure, we selected the 'cosine' distance to consider the sign of these differential values with an emphasis on the overall similarity among patterns.

Specifically, each node in the Yeo template of DMN (Yeo et al., 2011) was selected as a seed, regarding which a differential connectivity map was calculated. The individual-session differential maps were subject to the first-level k-means clustering. Similar to previous studies, the number of clusters was determined using the criterion of the cluster cost, computed as the ratio between within-cluster distance to between-cluster distance (Allen et al., 2014; Li et al., 2021), in order to minimize the within-cluster distance and maximize the between-cluster distance. The appropriate number of k was selected at the elbow of the curve, which optimally balances the cluster cost and cluster number. The individual-session centroids were then concatenated and used as input for the second-level clustering to yield group-level patterns which are in the following referred to as aliased functional connectivity patterns (AFCPs).

Furthermore, we utilized a region-of-interest (ROI) approach to visualize which frequencies contributed to the aliased connectivity values. Based on each AFCP, we have selected a seed ROI that yielded the corresponding AFCP map and then selected a target

ROI in the hemisphere-symmetric location with representative differential values. We quantified the frequency contribution to aliased connectivity by decomposing the correlation coefficient between time traces of the seed and target ROIs by Fourier transformation of the time traces (Cordes et al., 2001; Cordes et al., 2000). Three frequency bins were calculated: < 0.05 Hz, 0.05 – 0.1 Hz, 0.1 – 0.2 Hz, for both DOT and DS-DOT. Note that AFCP were calculated based on the DOT and DS-DOT filtered from 0.009 Hz to 0.08 Hz. Therefore, we have normalized the frequency-specific connectivity values at each bin to the connectivity values of 0.009-0.08 Hz in the original DOT, in order to itemize the frequency-specific contributions.

3.2.8 Statistical Analysis

To assess the significance of the functional connectivity values, all group-level maps were subject to node-wise one-sample two-tailed Student's t-tests. The resulted p values were corrected for multiple comparisons using Benjamini-Hochberg method (n = 12021; n is the number of nodes which are commonly available across all participants) (Benjamini and Hochberg, 1995), resulting in *q* values. Also, to assess the significance of the aliased functional connectivity patterns, all group-level centroids were subject to node-wise one-sample two-tailed Student's t-tests. The resulted statistics were also corrected for multiple comparisons using Benjamini-Hochberg method (Benjamini and Hochberg, 1995).

3.3 Results

3.3.1 Hemodynamic Activity at the Sensory Level

In the present study, resting-state hemodynamic activity in the human participants is measured by pairing optical sources and detectors in a whole-head, cap-based system.

The time traces of a fNIRS channel in two wavelengths (760 nm and 850 nm) are illustrated in **Figure 3-2A**, with time segments of motion artifacts that are excluded from further analyses. The power density spectrums (PSDs) of the time traces are shown in **Figure 3-2B**. Notably, in the representative participant, the cerebral hemodynamics show a peak in the ultra-slow range (< 0.1 Hz), in addition to peaks associated with the cardiac pulse (~ 1.3 Hz) and respiration (~ 0.23 Hz). After band-pass filtering of 0.008 – 0.2 Hz, the time traces present resting-state, spontaneous fluctuations in **Figure 3-2C**.

In addition, in order to examine the effect of a low sampling rate on the hemodynamic activity and connectivity, we have deliberately down-sampled the time traces of the fNIRS data from originally 6.25 Hz to 0.48 Hz (**Figure 3-2D)**. As a result, there are considerable differences in the amplitudes of PSDs between fNIRS and down-sampled data (**Figure 3-2E**). Notably, down-sampled data present higher power amplitudes than the original data, due to the aliasing of cardiac and respiratory activity into the ultra-slow range. After band-pass filtering of 0.008 - 0.2 Hz, there appears a greater amount of and faster-evolving fluctuations in the down-sampled data **(Figure 3-2F)**.

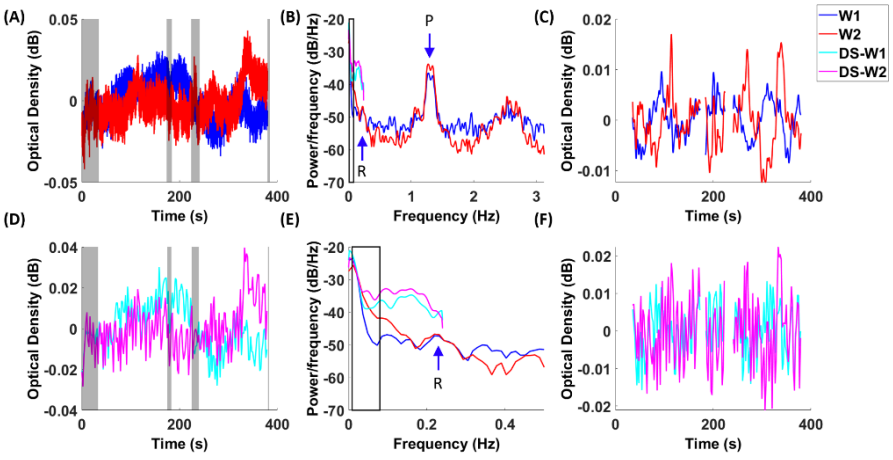

Figure 3-2: fNIRS time courses and spectrums. Temporal traces of raw data in fNIRS (A) and down-sampled fNIRS (D). Gray shaded areas indicate the time segments with motion artifacts. Power spectrums of fNIRS (B) and down-sampled fNIRS (D). Black squares indicate the power spectrum at 0 – 0.5 Hz. Band-pass filtered (0.009 – 0.08 Hz) time courses in fNIRS (C) and down-sampled fNIRS (F). An arrow labeled with "P" indicates the peak associated with cardiac pulses in the signal. An arrow labeled with "R" indicates the peak associated with respirations in the signal.

3.3.2 Resting-state Functional Connectivity Maps of DOT and fMRI

We evaluated the cross-modal correspondence of DOT and fMRI regarding the default mode network obtained in the same group of participants. The seed regions and corresponding seed-based functional connectivity with mPFC, IPL, precuneus and a compound seed (the average of mPFC, IPL, and precuneus) are shown in **Figure 3-3**, with maps thresholded at $q < 0.05$ after multiple-comparison correction. **Figure 3-4** shows the unthresholded maps. The seed-based functional connectivity maps of DOT in both **Figures 3-3 and 3-4** present spatial patterns comparable with those of fMRI, which is consistent with high spatial correlations and dice coefficient values between DOT and fMRI functional connectivity maps, as listed in **Table 3-2**. The compound-seeded functional connectivity maps of DOT depict the DMN hubs including mPFC, IPL, and precuneus, which spatially resemble those of fMRI (**Figure 3-3A**). The mPFC-seeded functional connectivity maps of DOT show functional connectivity between left and right mPFC, similar to that of fMRI (**Figure 3-3B**). The IPL-seeded functional connectivity maps of DOT exhibit similar spatial patterns to that of fMRI and reveal functional connectivity between left and right IPL (**Figure 3-3C**). The precuneus-seeded functional

connectivity maps of DOT show functional connectivity at left and right precuneus as depicted in fMRI (**Figure 3-3D**). We have primarily focused our cross-modal investigation on HbR data because the HbR contrast approximates the imaging mechanism of fMRI. In addition, **Figure 3-5** shows the HbO-derived default mode network that also presents a consistently high resemblance with fMRI, which is consistent with the quantitative values of spatial correlations and dice coefficients listed in **Table 3-3.**

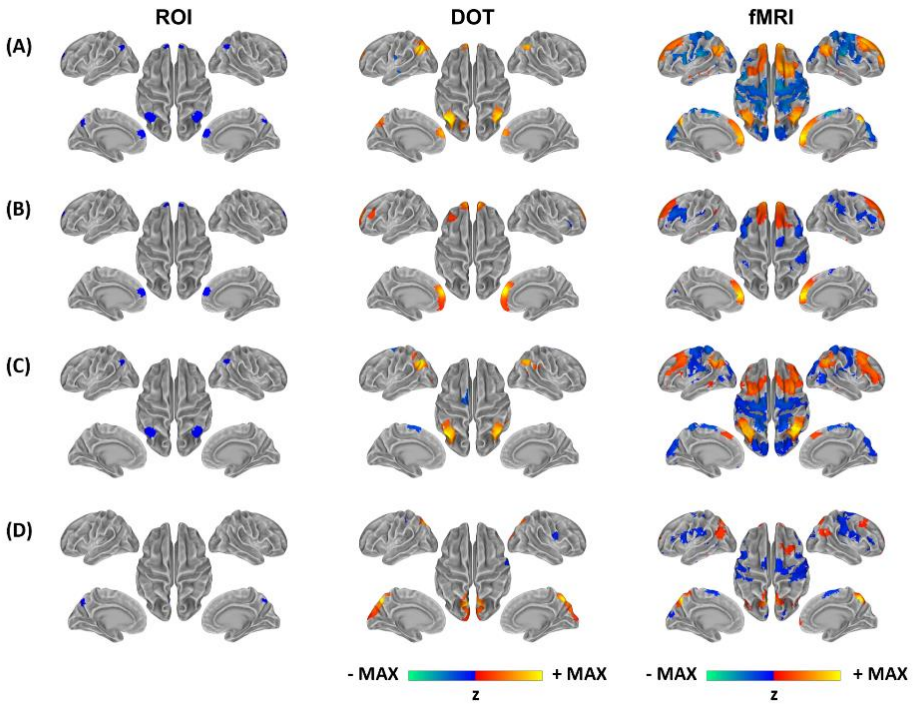

Figure 3-3: Resting-state functional connectivity by fNIRS HbR and fMRI. Connectivity maps are based on seeds of (A) a compound seed (the average of mPFC, IPL and precuneus) (B) mPFC, (C) IPL and (D) precuneus ($q < 0.05$ after multiple comparison correction).

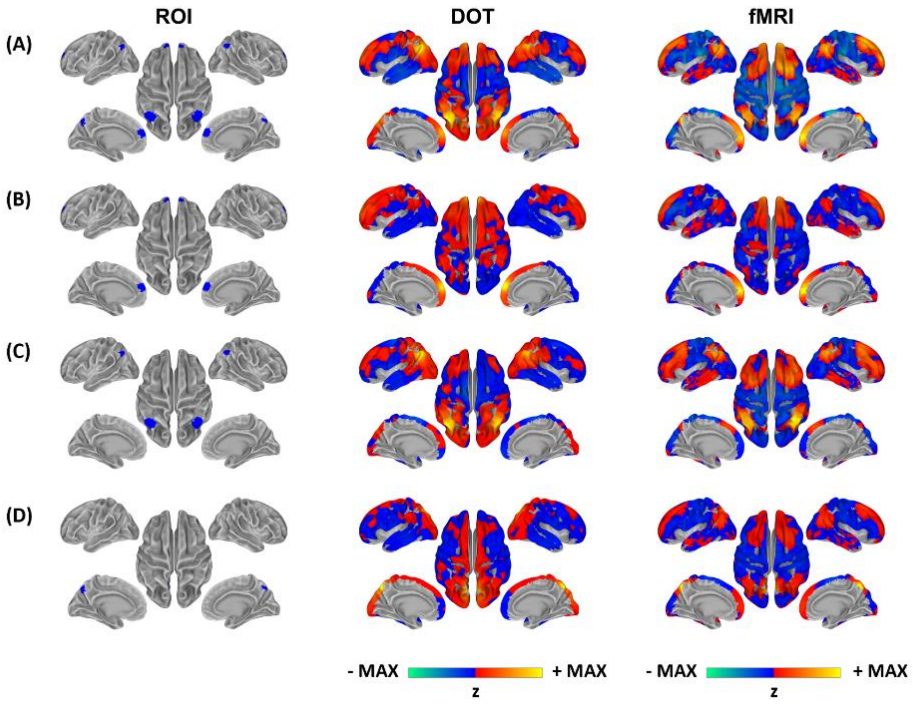

Figure 3-4: Unthresholded resting-state functional connectivity by fNIRS HbR and fMRI. Unthresholded connectivity maps are based on seeds of (A) a compound seed (the average of mPFC, IPL and precuneus) (B) mPFC, (C) IPL and (D) precuneus.

Table 3-2: Comparison between resting-state functional connectivity maps by fNIRS HbR and fMRI. Spatial correlations are calculated based on unthresholded maps. Dice coefficients are calculated based on thresholded maps at $q < 0.05$ after FDR correction.

Seed	Spatial Correlations	Dice Coefficients
Compound	0.47	0.20
mPFC	0.56	0.29

IPL	0.49	0.22
Precuneus	0.57	0.23

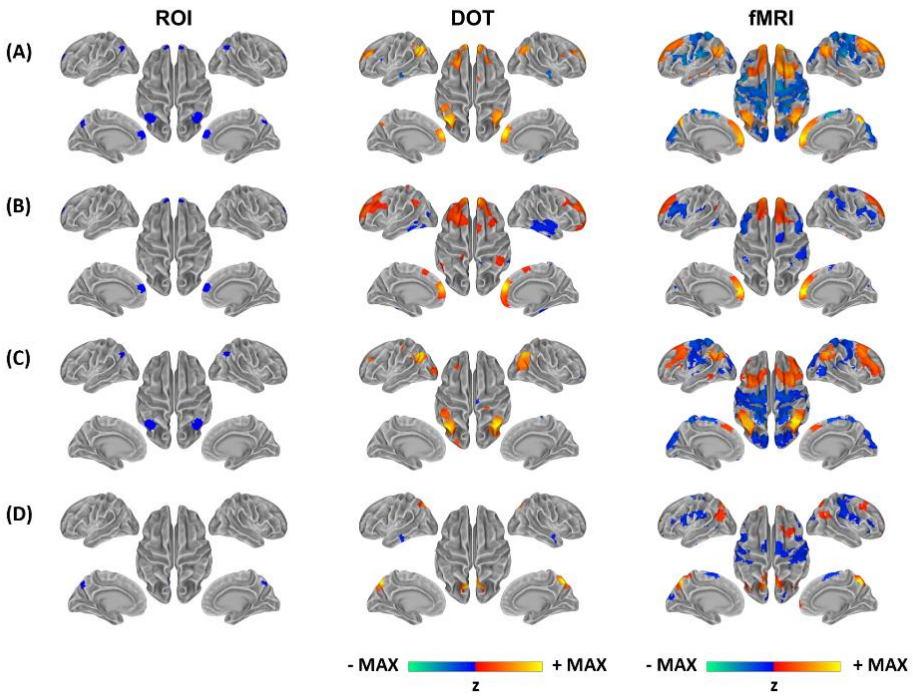

Figure 3-5: Resting-state functional connectivity by fNIRS HbO and fMRI. Connectivity maps are based on seeds of (A) a compound seed (the average of mPFC, IPL and precuneus) (B) mPFC, (C) IPL and (D) precuneus ($q < 0.05$ after multiple comparison correction).

Table 3-3: Comparison between resting-state functional connectivity maps by fNIRS HbO and fMRI. Spatial correlations are calculated based on unthresholded maps. Dice coefficients are calculated based on thresholded maps at $q < 0.05$ after multiple comparisons correction.

Seed	Spatial Correlations	Dice Coefficients
Compound	0.41	0.23
mPFC	0.48	0.34
IPL	0.39	0.23
Precuneus	0.56	0.18

3.3.3 Aliased Functional Connectivity Patterns

Furthermore, we examined whether aliased activity due to an insufficient sampling rate led to aliased functional connectivity. By exploring a data-driven analysis of the differential connectivity maps between DOT and DS-DOT, we have identified a set of four structurally organized patterns that represent the aliased connectivity. **Figure 3-6** shows the spatial maps of seeds and centroids of the aliased functional connectivity patterns (AFCP) generated by the two-level k-means clustering. The numbers of clusters (k1 = 5, k2 = 4) were determined based on the L-curves of the ratio between within-cluster distance to between-cluster distance of the first- and second-level clustering, respectively (shown in **Figure 3-7)**. **Figure 3-6A** visualizes the spatial distribution of the seeds that drive each AFCP, via a winner-take-all strategy to map the seeds associated with the highest occurrence of clusters. Interestingly, for each AFCP, seeds that led to a common aliasing pattern exhibit cortical patches with spatial continuity and bilateral hemispheric symmetry. For example, seeds for AFCP1 are aggregated at IPL, AFCP2 at prefrontal cortex, AFCP3 at mPFC and AFCP4 at temporal cortex, while all AFCPs

involve seeds from bilateral hemispheres (**Figure 3-6A**). Furthermore, AFCPs are distinct spatial patterns that include both increases and decreases in functional connectivity that are produced after down-sampling the signals to a low rate (**Figure 3-6B**). Although the seeds were confined to be within the Yeo template of DMN, the aliased connectivity values extend to the whole cortical space. AFCP1 shows decreased functional connectivity in bilateral IPL and increased functional connectivity in frontal and visual cortices after down-sampling, while the AFCP1 is associated with seeds from IPL only. AFCP2 shows decreased functional connectivity in bilateral mPFC and temporal cortex and increased functional connectivity in bilateral visual cortex, with AFCP2 associated with seeds at prefrontal cortex. AFCP3 shows decreased functional connectivity in bilateral mPFC and motor cortex and increased functional connectivity in bilateral temporal cortex. Meanwhile, AFCP4 shows an almost reversed pattern against AFCP3, with increased functional connectivity in bilateral mPFC, motor cortex, IPL and precuneus and decreased functional connectivity in bilateral temporal cortex. Interestingly, despite their inversely related patterns, AFCP3 and AFCP4 are associated with distant seed patches, centering at mPFC and temporal cortices respectively.

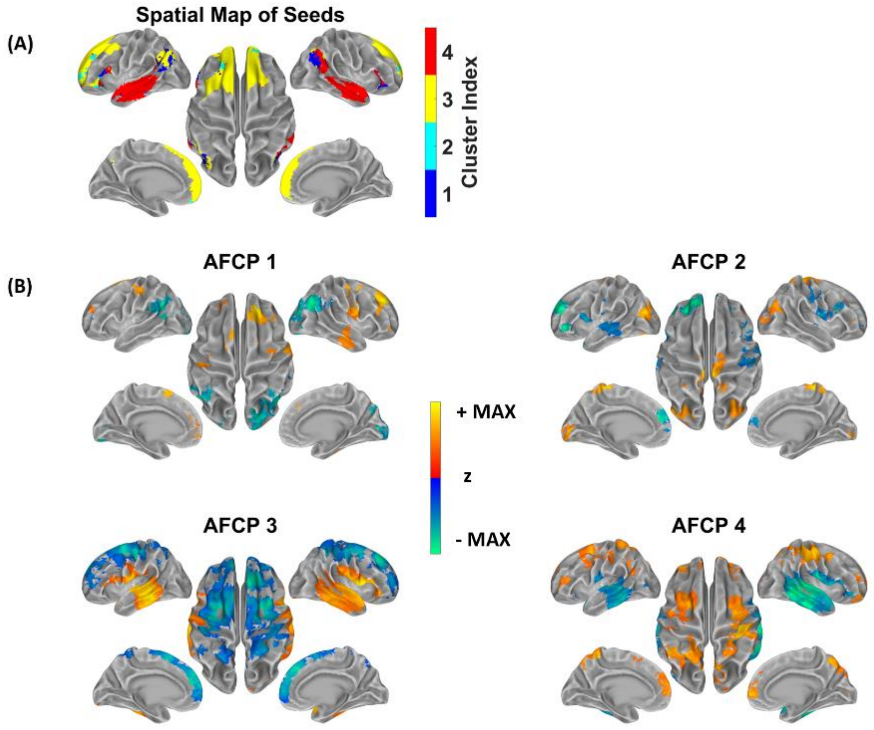

Figure 3-6: Aliased functional connectivity patterns (AFCPs) of HbR. (A) Four AFCPs are discovered and their associated seeds. At each seed, the AFCP which has the highest number of sessions in all differential functional connectivity maps was assigned. (B) Spatial distribution of each AFCP. Red-yellow color bar indicates an increase in functional connectivity and blue-green indicates a decrease in functional connectivity caused by the insufficient sampling frequency ($q < 0.05$ after multiple comparisons corrected).

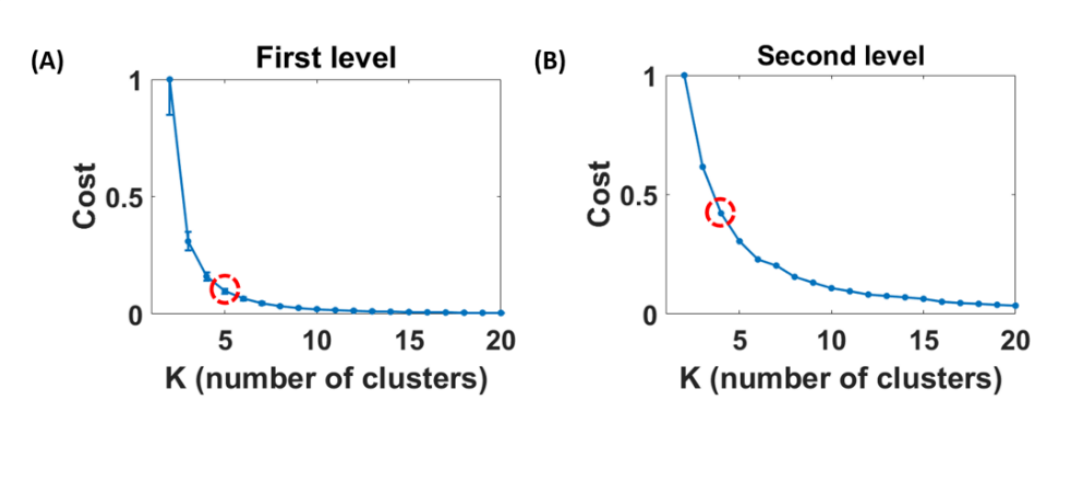

Figure 3-7: L curve for k-means clustering. The cost as the ratio between within-cluster distance to between-cluster distance is plotted against the cluster numbers for the (A) first-level and (B) second-level clustering. The red dash circled indicates the elbow of the curve, which was selected as the number of aliased functional connectivity patterns for the individual- and group-level clustering.

In order to further delineate the frequency-specific contributions of the aliased connectivity values, we have utilized a ROI approach to visualize the connectivity values before and after down-sampling. **Figure 3-8** illustrates the seed and target ROIs circumscribed at hemispherical symmetric regions per each AFCP. Since RSFC is calculated in the filtered signals of 0.009-0.08 Hz as commonly in fMRI, the RSFC of original DOT of 0.009-0.08 Hz served as the normalizing baseline to compare the values across all frequency bins. Regarding the left and right IPL as representative ROIs (**Figure 3-8A**), down-sampling has induced a significant decrease in the RSFC of 0.009-0.08 Hz in HbR. Meanwhile, the original DOT shows lower connectivity values in the upper frequencies (0.05-0.1 Hz and 0.1-0.2 Hz) that are below the bar at the infra-slow frequencies (<0.05 Hz), suggesting that unsynchronized activity in upper frequencies is

associated with the RSFC decreases after down-sampling. **Figures 3-8 B-D** show additional ROIs at hemispherically symmetric positions in other AFCPs in HbR, where the DS-DOT data present decreases in RSFC of 0.009-0.08 Hz. Likewise, relative lower connectivity values are seen in the upper-frequency range (0.05-0.1 Hz and 0.1-0.2 Hz), compared to those in the ultra-slow range (<0.05 Hz), again indicating the unsynchronized activity coincides with decreases in RSFC. On the contrary, an increase in connectivity does occur in the down-sampled HbO DOT as shown in another representative seed ROI at the mPFC (**Figure 3-8E**). Interestingly, in this case, the upper frequencies 0.05-0.1 Hz and 0.1-0.2 Hz shows connectivity values as high as those in the infra-slow range (< 0.05 Hz), which in turn are associated with a remarkable four-fold increase of RSFC in DS-DOT, suggesting that the aliasing from synchronized activity contributed to the increase of RSFC.

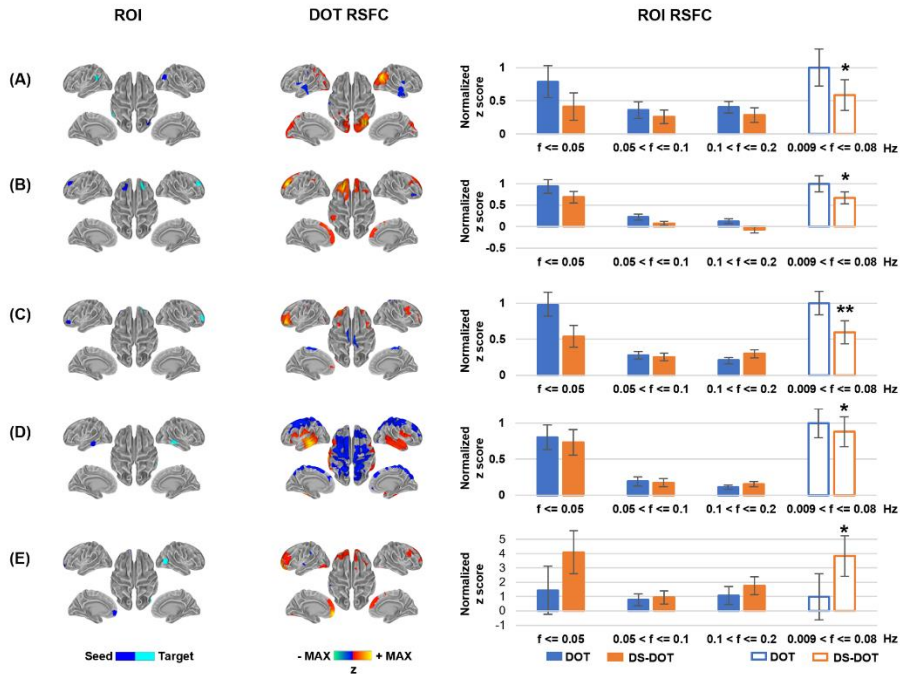

Figure 3-8: Frequency contributions to resting-state functional connectivity in ROIs. (A-D) seed and target regions were selected based on aliased functional connectivity patterns in HbR. (E) seed and target regions were selected to show an increase in functional connectivity due to aliasing effects in HbO. The connectivity values (mean and standard errors) are normalized to the mean connectivity of DOT in the range from 0.009 Hz to 0.08 Hz, for each ROI pair. * indicates a significant difference between DS-DOT and DOT, at $p < 0.05$. ** indicates a significant difference between DS-DOT and DOT, at $p < 0.01$.

3.4 Discussions

In this study, we have demonstrated the feasibility of a whole-head, cap-based and high-density fNIRS system in mapping large-scale DMN using conventional seed-based RSFC analysis. Previous fNIRS studies with partial or sparse montages have been able to map the RSFC concerning prefrontal (Mesquita et al., 2010), sensorimotor (Lu et al., 2010; Mesquita et al., 2010; White et al., 2009), auditory (Lu et al., 2010) and visual areas (Mesquita et al., 2010; White et al., 2009). However, the capability of fNIRS in mapping large-scale brain networks has not been fully established, especially in those cognitively related brain networks such as DMN, dorsal attention network and frontoparietal control network that involve multiple distanced regions (Andrews-Hanna et al., 2007; Greicius, 2008; Zhang and Raichle, 2010). Recent fNIRS studies have made progress in mapping part of DMN (Eggebrecht et al., 2014), yet important midline regions or IPL are still missing due to lacking optodes to fully cover those. Here we reported a novel fNIRS-DOT study based on a whole-head and cap-based fNIRS array. Especially, our tomographic fNIRS data as illustrated in **Figure 3-3** have for the first time shown a

complete DMN system including mPFC, posterior midline, and bilateral IPLs, which exhibits remarkable spatial similarity to fMRI RSFC maps derived from the same group of participants. In addition, the maps from fNIRS data also show correspondence with the template DMN generated in a large-scale fMRI study (Thomas Yeo et al., 2011).

Our demonstration of a fNIRS system in imaging DMN is especially important for monitoring the brain in aging and progressive AD states. Our results have revealed the functional connectivity among mPFC, precuneus and IPL, all of which are closely associated with memory and other cognitive functions (Sperling et al., 2010). The inclusion of these key regions in the DMN has significant clinical values. Andrews-Hanna et al. (2007) have shown that the anterior-posterior functional connectivity between midline DMN structures at semantic classification and passive fixation tasks is reduced in normal aging and positively correlated with cognitive performance. Similarly, Damoiseaux et al. (2008) demonstrated that, in the resting state, the reduced RSFC in DMN is associated with aging years and correlated with declined performance in neuropsychological tests. Many studies across individuals with AD or prodromal AD have documented altered functional connectivity within DMN, including precuneus/PCC, mPFC and inferior parietal cortex (Greicius et al., 2004; Koch et al., 2012; Sorg et al., 2007; Zhou et al., 2010). Intriguingly, it has been noted that the amyloid-β accumulation distribution in AD strikingly overlaps with the cortical hubs of high activity and metabolism, such as mPFC and PCC, which indicates the association between the functional connectivity at these cortical hubs and amyloid-β deposition (Buckner et al., 2009). It is further postulated that the pathological process in these key DMN regions also extends to the aging individuals at the preclinical stage of AD even before clinical

symptoms develop (Bateman et al., 2012; Sperling et al., 2009). Therefore, neuroimaging of such resting-state connectivity in DMN and other cognitive networks has been placed at pivotal positions, such as biomarkers, in clinical trials of intervention and prevention studies (Cavedo et al., 2014; Sperling et al., 2014). However, notably fMRI has been the primary modality, in many cases the only modality, to be included for functional neuroimaging in these studies. Power analysis for the prevention trials in AD usually yielded more than 1,000 individuals are needed (Hsu and Marshall, 2017). Considering the overwhelming number of people that are projected to be with AD and an even larger number to be placed at the prevention and intervention stages, the limited accessibility and high expenses of MRI instruments become a bottleneck in the workflow. Therefore, the fNIRS-DOT capability as demonstrated in our study provides an economic and practically feasible option for assessing the anterior-posterior DMN connectivity as biomarkers for monitoring aging and Alzheimer's disease in large populations.

In addition, we have shown that a sampling rate that is much lower than the respiration and cardiac pulse frequency will introduce spatially organized aliased connectivity to RSFC. By deliberately down-sampling the raw fNIRS recordings to a sub-hertz frequency, we demonstrated that differences in the activity as well as connectivity do occur in the down-sampled data. Furthermore, our data-driven analysis on the differential RSFC maps between DOT and DS-DOT has revealed that the aliasing effect is seed-/region-dependent (e.g., AFCP3 vs. AFCP4) and that the resulted spurious connectivity exists within the DMN regions and extends beyond in other cortical areas, appearing as aliased networks (**Figure 3-6**). Although fNIRS offers the advantage of high temporal resolution, maintaining a high sampling rate while using a large number of optodes can

become a challenge, or sometimes compromise, for the deployment of full-head coverage and high-density measurement. Despite that a low sampling has been widely used in similar fMRI studies, our findings have emphasized that maintaining a sufficiently high sampling rate of fNIRS is crucial, especially when RSFC of DMN is considered as a biomarker. For example, the functional connectivity between IPL and mPFC has been shown to be associated with normal aging (Andrews-Hanna et al., 2007) and AD (Koch et al., 2012). However, we demonstrated that when the seed is placed at mPFC, the aliasing effects can cause inflated and deflated functional connectivity in temporal cortex and mPFC, respectively (AFCP3 in **Figure 3-6**). Another example is AFCP1 in **Figure 3-6**, where down-sampling has led to a decreased connectivity in hemispherically symmetrical left and right IPL regions, which is consistent with the fMRI findings that the IPL connectivity is decreased in the down-sampled data than the original data at short TR (Golestani et al., 2017). Our analysis of the frequency decomposition on these connectivity values (**Figures 3-8 A-D**) has pointed out that the unsynchronized upper-frequency range is likely the origin of the alternations seen in down-sampled data of ultra-slow 0.009-0.08 Hz. The aliased activity from the respirational and cardiac frequencies could become unsynchronized noises to attenuate the correlations in cerebral hemodynamics, which is also supported by Huotari et al. (2019) when down-sampled fMRI data with TR = 3 s had significantly lowered correlation coefficients than raw data. Meanwhile, aliasing-related increases to RSFC is also possible, as shown in **Figure 3-8E**, which suggests that the physiological noises in synchronization may be a significant contributor or even dominating the RSFC in insufficiently sampled cerebral hemodynamics. Since the aliased functional connectivity patterns may obscure our

current understanding, accurate imaging without aliasing is especially important in understanding AD stages, because of the high comorbidity of vascular diseases in aging populations.

Implications of the organized aliased patterns are relevant to fMRI. Furthermore, the seed- and region-dependent properties of aliasing effects demonstrated in this work are supported by the literature. Typically, whole-brain fMRI has a TR of 2 s and can only theoretically sample the signals up to 0.25 Hz, which is, unfortunately, lower than the necessary Nyquist rate for respiratory (~0.3 Hz) and cardiac (~1 Hz) activity. Earlier fMRI studies have already shown that aliased activity do exist in the voxel-wise measurements (Cordes et al., 2001; Cordes et al., 2000). In addition, cardiac pulsation (Chang et al., 2009; Glover et al., 2000) and respiration (Birn et al., 2006; Birn et al., 2008) are major origins of aliased activity in typical fMRI scans. However, the aliasing effects on functional connectivity are still poorly understood. Our study has taken a novel data-driven approach and revealed, for the first time, several whole-brain patterns attributed to the aliasing. The AFCPs discovered in our study are supported by a number of fMRI studies. Tong et al. (2011) have demonstrated that the aliased cardiac signals appear in a spatial distribution that consists of dense arteries and large veins, which appears similar to AFCP3 and AFCP 4. Other studies using ultrafast fMRI at TR = 0.35 s (Boubela et al., 2013) or 0.1 s (Huotari et al., 2019) also identified similar patterns associated with cardiac pulsation. Importantly, our analysis has pointed out that the aliasing could contribute to not only increases but also decreases in connectivity in a reversed spatial pattern, depending on the different seed regions (mPFC drives AFCP3 vs. middle temporal cortex drives AFCP4). Meanwhile, studies utilizing ultrafast fMRI

have demonstrated that respiration affects prefrontal and occipital regions (Tong and Frederick, 2014), which also appears in AFCP 1 and AFCP2. More recently, a study with MREG (TR = 0.1 s) also depicted that the cardiac power is prominent in areas adjacent to cerebral arteries and large venous sinuses while the respiratory power is strong in the posterior regions, perivenous cortical structures and posterior central cerebrospinal fluid (CSF) ventricles (Huotari et al., 2019). The abovementioned previous studies, either using the aliased or unaliased signals, have jointly demonstrated that respiration and cardiac pulsation have distinct spatial distributions in the BOLD signals. In other words, respiration and cardiac pulsation can cause different aliased signals in the low-frequency band (~0.1 Hz) across different regions when they are sampled with an insufficient sampling rate. As the functional connectivity is estimated by measuring the temporal correlation of LFOs between the seed and the other region, the aliasing effects on functional connectivity are, therefore, a compound of the aliasing effects on BOLD signals in the seed and the other region. It is hence plausible that our results demonstrated the aliasing effects of insufficient sampling rate on functional connectivity are both seed- and region-dependent. Noteworthy, the standard normalization procedure for human brain imaging focuses on normalizing the brain tissues into a homogenous space. However, the anatomy of vasculature is outside of the scope of such normalization. Nonetheless, our data-driven analysis that focuses on segregating the differential connectivity maps was able to discover several organized aliased connectivity patterns at the group level. Interestingly, recent emerging evidence has demonstrated that BOLD spontaneous activity might exist in frequency bands above 0.1 Hz, the conventional cutoff for functional connectivity (Boubela et al., 2013; Chen and Glover, 2015; Jahanian et al.,

2019). Although it is not clear whether or to what extent these high-frequency connectivity patterns are driven by noises or neuronal activity, delineating aliasing contributions from valid neuronal-driven hemodynamics is crucial in understanding the functional organization of the human brain.

3.5 Conclusions

Functional neuroimaging of the resting-state brain networks has been placed at pivotal positions, such as biomarkers, in studies of aging and clinical trials for Alzheimer's disease. However, notably fMRI has been the primary modality, in many cases the only modality, to be included for functional neuroimaging in these studies. Our study has demonstrated that the cap-based, brain-wide fNIRS recordings can map the resting-state functional connectivity in the posterior midline, prefrontal and parietal structures of the default mode network. fNIRS as a broadly accessible modality has tremendous potential to accelerate aging research, especially in large populations. The extensive clustering analyses in our work have provided a comprehensive roadmap for the aliasing effects on functional connectivity due to insufficient sampling rate and emphasized the importance of maintaining a high sampling rate to avoid the aliasing effects or applying signal correction techniques to reduce the aliasing effects when studying resting-state functional connectivity.

4 Chapter 4 Controlling Jaw Clenching Motion Artifacts in fNIRS

4.1 Introduction

Compared with fMRI, fNIRS provides complementary advantages of low cost, portability and low operating noise and compatibility with medical electronic implants (e.g., cochlear implants) (Chiarelli et al., 2017; Luke et al., 2021; Scholkmann et al., 2014). Therefore one of the booming applications of fNIRS is in studying speech perception and production (Sevy et al., 2010; Wan et al., 2018). There are several features of fNIRS that make it a unique tool for studying auditory and language functions. fNIRS is quiet compared with fMRI in which the scanner generates loud operating noise. The silent environment could avoid interferences with auditory stimulation and other psychological effects such as stress and fear, which have been shown to induce activations in the auditory cortex (Plichta et al., 2011). Unlike fMRI, EEG and MEG, fNIRS has no interference with cochlear implants or hearing aids, as it uses near-infrared light to measure the hemodynamic signals. Furthermore, as the light emitters and detectors are mounted on a cap attached to the head, fNIRS is considered relatively less sensitive to head movements (Cui et al., 2010) and does not require participants to be constrained in a head-fixed position, which makes it suitable for cohorts with limited tolerance and compliance, including infants, children and the elderly.

fNIRS has drawn increasing interest from the neuroscience community to employ this technique to investigate auditory function in healthy subjects and patients with hearing loss (Pollonini et al., 2014; Saliba et al., 2016). For example, fNIRS can be used in infants who have cochlear implants and are unable to verbally communicate their hearing and comfort when adjusting sound levels (Bortfeld, 2019). The understanding of

auditory perception mechanisms of normal sound and cochlear stimuli can facilitate the early intervention of hearing loss in infants to reserve and develop their speech and auditory function. Another rapid increase of fNIRS usage is in cognitive neuroscience in a naturalistic or challenging environment. Exemplar work includes studies using wearable fNIRS to investigate walking in patients with Parkinson's disease (Nieuwhof et al., 2016) or elderly people with mild cognitive impairment to assess cognitive functions (Maidan et al., 2016; Makizako et al., 2013).

However, there are critical confounding factors in fNIRS signals, including interferences from superficial layers of the head, systemic physiological noise and motion artifacts (von Lühmann et al., 2019; von Lühmann et al., 2020; Zhang et al., 2021). Although less vulnerable to head movements, fNIRS can still suffer from jaw movements such as speech speaking and voluntary jaw clenching, which can cause contractions of the temporalis muscle (Novi et al., 2020; Schecklmann et al., 2017). The jaw movements could result in blood flow changes in the temporal muscle as well as relative movements between the optodes and the scalp, leading to artifacts in the fNIRS signals (Schecklmann et al., 2017). While many previous studies have investigated the impact and correction of head movements (Cui et al., 2010; Fishburn et al., 2019; Izzetoglu et al., 2010; Scholkmann et al., 2010), the effect and especially handling of jaw movements in fNIRS signals remain largely unclear (Novi et al., 2020; Schecklmann et al., 2017).

In our previous preliminary work, we studied the motion artifacts related to jaw movements, including clenching, speaking, swallowing and sniffing and observed that jaw clenching produced robust and consistent artifacts in fNIRS signals (Zhang et al., 2022). In this study, we aimed to characterize the jaw-clenching-related artifacts in

fNIRS, test whether an individually customized bite bar can help to suppress jaw movements, and test whether our previously established denoising pipeline namely PCA-GLM (Zhang et al., 2021) can reduce the artifacts in fNIRS signals due to jaw clenching. These aims were realized by one experiment provoking the jaw-clenching artifacts, one experiment evoking the auditory response and one experiment depicting the resting-state functional connectivity.

In this study, we instructed healthy subjects to perform three types of tasks, including a jaw clenching task, an auditory task and a resting task. Before each experiment, we customized a bite bar for each participant. The jaw clenching task required the subjects to voluntarily clench their jaw following a block design. The auditory and resting tasks were performed repeatedly with and without applying a bite bar to each participant, in order to validate the efficacy of an individually customized bite bar in suppressing jaw clenching. Data of all three types of tasks were preprocessed with a minimal preprocessing pipeline and our previously established PCA-GLM method (Zhang et al., 2021) to test the efficacy of the PCA-GLM method in removing the jaw clenching artifacts.

4.2 Methods

4.2.1 Participants

Informed consent was obtained from each subject before the beginning of each experiment. All study protocols were approved by the Institutional Review Boards at The University of Oklahoma Health Sciences Center. A total of ten healthy subjects without acute jaw and teeth problems participated in this study. Data from one subject were excluded due to bad coupling between optodes and scalp. Therefore, data from nine

subjects (six females, 23.1 ± 5.9 years old) were used for the analyses. Participants received financial compensation for their participation.

4.2.2 Design of Bite Bar

Bite bars were made using a plastic piece and vinyl polysiloxane putty for each subject. Specifically, a plastic piece was first created using Adobe Illustrator (Adobe Systems Inc., San Jose, CA, USA). This piece was then laser cut out of quarter-inch-thick acrylic at the University of Oklahoma Fabrication Lab. The piece measured 4 x 1.5 inches with a 1.25-inch diameter semicircular cutout on the narrower end. The bite bar was assembled by combing the plastic piece and dental putty. The putty used here was vinyl polysiloxane, which was made by mixing 5 mL putty base and 5 mL putty catalyst thoroughly for 1 minute. The mixture putty was then formed around a bite piece and placed in the subject's mouth such that the bite bar was inserted comfortably approximately 1-2 inches deep. The subject was then instructed to bite down firmly while the putty was molded by their teeth for three minutes. After the putty was molded, the bite bar was ready for use in the experiment. A picture of the bite bar customized for one of the subjects is shown in **Figure 4-1A**.

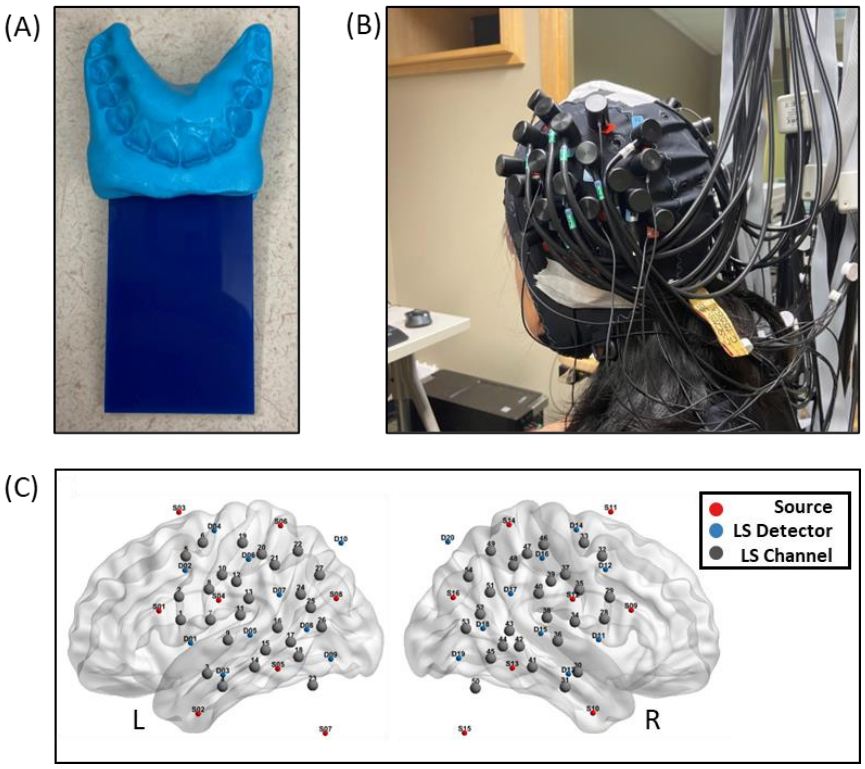

Figure 4-1: Experimental settings. (A) A customized bite bar. The bite bar was assembled using dental putty (top) and a plastic piece (bottom). (B) Arrangement of fNIRS optodes in a human subject. (C) Illustration of the fNIRS optodes covering the auditory and parietal cortices. The red solid circles, blue solid circles, and gray solid circles indicate fNIRS sources, long-separation (LS) detectors and LS channels, respectively.

4.2.3 Experimental Paradigm

Participants were instructed to perform three types of tasks in a comfortable sitting position with their eyes opened. Specifically, each subject performed (1) two sessions of a jaw-clenching task, (2) three sessions of auditory task without biting a bite bar, (3) three sessions of auditory task with biting a bite bar, (4) two sessions of resting-state task without biting a bite bar and (5) two sessions of resting-state task with biting a bite bar. The tasks of with-bite-bar vs. without-bite-bar conditions were counterbalanced in two

sequences, to which subjects were randomly assigned. A jaw-clenching session consisted of seven blocks, each of which included a clenching period of 20 s and a resting period of 30 s. During the clenching period, the participants were instructed to perform the jaw clenching at 0.15 Hz (i.e., with an interval of 6.67 s) guided by a visual cue. An auditory session consisted of seven blocks, each included an auditory stimuli period of 20 s and a resting period of 30 s. The auditory stimulus was adapted from a previous study (Chen et al., 2015) and consisted of two pure tones of 554 and 440 Hz. The tones were sampled at 44.1 kHz and were alternated, starting with the 554 Hz tone. Each tone lasted 500 ms with a 50 ms linear rise and fall. The stimulus was made in the Adobe Audition software (Adobe Systems Inc., San Jose, CA, USA). Each resting session lasted six minutes. In total, 10 sessions of recording were acquired from each subject. E-Prime (Psychology Software Tools, Sharpsburg, PA) software was used to display instructions and present the tasks on an LCD monitor. The auditory stimuli were played at a fixed sound volume (60 dB sound pressure level) through two earbuds worn in the ears of participants.

4.2.4 Data Acquisition

A NIRScout system (NIRX, New York, United States) was used to collect fNIRS data at a sampling rate of 3.91 Hz. A total of 16 light sources (760 nm and 850 nm) and 20 light detectors were arranged over the left and right auditory cortices to form an array with 54 long-separation (LS) channels at about 30-mm distance. In addition, 16 short-separation (SS) (8-mm) detectors were placed around each source and constructed 16 SS channels. **Figures 4-1B and C** show the instrument setting and the layout of fNIRS optodes. Physiological measurements including triaxial acceleration, respiration, and cardiac pulsation were also simultaneously collected by a 64-channel actiCHamp system

(Brain Vision, North Carolina, United States), following the protocol described in Zhang et al. (2021).

4.2.5 fNIRS Data Preprocessing

fNIRS data were preprocessed using Homer2 (Huppert et al., 2009) and proprietary codes in MATLAB® (The Mathworks, Natick, MA) reported in our previous work (Zhang et al., 2021). Specifically, the data were preprocessed following these steps: 1) converting the raw data into optical densities (ODs); 2) calculating the power spectral densities of each channel using the Welch's method with a time window of 60 s and 50% overlapping and rejecting bad channels which showed no peak at heartbeat frequency range (0.8-1.6 Hz); 3) bandpass filtering ODs with 0.008-0.2 Hz; 4) converting the filtered ODs to relative changes of oxy-hemoglobin (HbO) and deoxy-hemoglobin (HbR) using the modified Beer-Lambert law (MBLL) (Scholkmann et al., 2014). The differential pathlength factors of 7.25 and 6.38 were used for 760 nm and 850 nm, respectively (Herold et al., 2018). The molar extinction coefficients were 645.5 cm-1/M and 1097.0 cm-1/M for HbO and 1669.0 cm-1/M and 781.0 cm-1/M for HbR at 760 nm and 850 nm, respectively (Piper et al., 2014).

4.2.6 Denoising fNIRS Signals with Linear Regression

A general linear model (GLM) was configured per session for denoising processing. A third-order polynomial drift and a hemodynamic response function (HRF) regressor which accounts for the task-evoked effects were included in the design matrix. The HRF regressor was derived by convolving the stimuli structure with a canonical two-gamma HRF model (Lindquist et al., 2009). This GLM model was referred to as No Correction.

In addition, a more advanced model namely PCA-GLM (Zhang et al., 2021) was configured per session for data. A superficial systemic component (PC-SS) was identified by performing principal component analysis (PCA) on LS and SS measurements separately and correlation analysis between LS and SS components. The auxiliary measurements of triaxial acceleration, respiration and pulsation were bandpass filtered with 0.008 Hz - 0.2 Hz and then detrended by a third-order polynomial drift. The detrended auxiliary measurements and a third-order polynomial drift, a clenching regressor were included in the design matrix.

4.2.7 Block Averages and Topographies

For jaw-clenching and auditory tasks, the block averages were calculated by removing the baseline (i.e., mean amplitude of -5 to 0 s to the onset of each block) and calculating the mean and standard error across seven blocks. The topographies displayed the mean amplitudes across 5 to 15 s of the block averages of all LS channels. Standard errors were calculated in the block averaging process. Based on the clenching data, a channel of notable clenching-related artifacts was noted and designated as the clenching channel.

To examine the tasked-evoked response to auditory stimuli, we calculated the block averages of HbO. The averaged HbO amplitude during a stimulation window (5 – 18 s) was compared to the averaged HbO amplitude during a resting window (20 – 30 s) by a two-tailed paired-sample t-test, as a more sensitive measure of detecting the activations (Wu et al., 2022). An fNIRS channel of representative responses to the stimuli, namely the auditory channel, was selected based on the group-level HbO topography with

multiple comparisons correction by the Benjamini-Hochberg procedure with a false discovery rate of 0.05 (Benjamini and Hochberg, 1995).

4.2.8 Measure of Motion Artifacts

To assess the effects of jaw clenching on fNIRS signals and the efficacy of bite bar in suppressing jaw-related motion artifacts, we utilized a motion detection metric termed global variance of temporal derivatives (GVTD) which has been shown to strongly correlates with auxiliary measures of motion (Sherafati et al., 2020). Specifically, the optical densities of both wavelengths after bandpass filtering of 0.008 to 0.2 Hz were pooled together for the calculation of GVTD. The resulted GVTD time course represents the global co-fluctuation across all channels regardless of the sign/direction of the fluctuations. To assess whether jaw clenching introduces motion artifacts in fNIRS signals, the means of GTVD in the clenching period (0 - 20 s in each block) and the resting period (20 – 50 s in each block) were calculated for each session. A two-tailed paired-sample t-test was performed to determine whether there are significant differences in GVTD between the clenching and resting periods. In addition, to demonstrate the correlation between GVTD and instructed motion, the group-level GVTD time course was obtained by averaging the GVTD time courses from all sessions.

To assess whether a bite bar is effective in suppressing jaw-clenching movements, the mean GVTD across the entire session was calculated for auditory and resting tasks per session. A two-tailed paired-sample t-test was performed to determine whether there are significant differences in mean GVTD between auditory/resting data without and with addressing the individually customized bite bars to the subjects.

4.2.9 Evaluation of Motion Control Performance in Auditory Task

To evaluate the motion control performance by bite bar and PCA-GLM, we calculated four metrics, including within-subject standard deviation (SD), contrast-to-noise ratio (CNR), mean amplitudes and beta values of the HRF regressor, following our previous denoising study (Zhang et al., 2021).

(1) The within-subject standard deviation (SD) (Brigadoi et al., 2014) is calculated as the standard deviation across blocks of a single session when calculating the block averages.

(2) The contrast-to-noise ratio (CNR) is calculated as the difference between the mean amplitudes during the task and the rest period normalized by the summation of variances at task and rest periods (Cui et al., 2010; Nguyen et al., 2018; Zhang et al., 2005). The CNR is defined as follows:

$$CNR = \frac{mean(task) - mean(rest)}{\sqrt{var(task) + var(rest)}} \qquad (1)$$

where "task" denotes the task period (from 6 s to 18 s), and "rest" denotes the resting period (from -5 s to 0 s) with respect to the onset of each task block (t = 0 s). A high CNR value indicated that the ratio of task-evoked signal to noise is high.

(3) The mean amplitude is defined as the averaged amplitude of the relative concentration changes during a window (5 – 18 s) within the stimuli period (Strangman et al., 2002).

(4) The beta value of the HRF regressor is output from the GLM and represents the amplitude of activation.

In statistical analysis, a two-way analysis of variance (ANOVA) was performed on each of the four quantitative metrics (beta value, CNR, mean amplitude and within-subject SD) of the LS channel with bite bar condition and data processing method as factors. There are in total four different combinations including [No Bite Bar, No Correction], [Bite Bar, No Correction], [No Bite Bar, PCA-GLM] and [Bite Bar, PCA-GLM].

4.2.10 Evaluation of Motion Control Performance in Resting-state Recordings

Based on clenching data, a channel with the strongest artifacts was identified and designated as the clenching channel. To evaluate whether applying a bite bar and the denoising method has improved the resting-state functional connectivity, channel-wise connectivity was calculated and compared between the conditions of [Bite Bar, PCA-GLM] and [No Bite Bar, No Correction]. Since the purpose of our study was to evaluate the effect of motion control, we focused on the connectivity seeded from the clenching channel. The long-range connectivity was also known for being erroneously affected by motion (Power et al., 2012), we then focused on comparing the cross-hemispheric connectivity, i.e., between the left clenching channel and all channels on the right hemisphere. The Pearson's correlation coefficients were firstly calculated and converted to z scores by the Fisher Z-transformation. To assess whether functional connectivity was significant at the group level, a two-tailed one-sample t-test was performed. Then to assess whether applying a bite bar and the denoising method had made any difference, a two-tailed, paired t-test was performed between the conditions of [Bite Bar, PCA-GLM] and [No Bite Bar, No Correction]. The multiple comparison problem was addressed by

the Benjamini-Hochberg procedure (Benjamini and Hochberg, 1995) with a false discovery rate of 0.05.

4.3 Results

4.3.1 Effects of Jaw-clenching on fNIRS Signals

Figures 4-2A and B show the full time courses and block averages in two channels located at the temporal muscles (hereafter termed as clenching channels) in one representative subject and at the group level, respectively. The full time courses in bilateral clenching channels showed that the relative concentration changes in HbO and HbR both exhibited hemodynamic-response-like fluctuations consistent across seven consecutive blocks. The block averages modulated by the jaw clenching showed an increase in HbO and a decrease in HbR, highly resembling a hemodynamic response evoked by a motor (Zhang et al., 2021) or auditory task (Luke et al., 2021) but with a larger amplitude. More importantly, the peak in HbO caused by each of the three jaw-clenching movements is visible in the block averages. **Figures 4-2C and D** show the topographies of the mean amplitudes averaged across 5 to 15 s visualized by NIRS-KIT (Hou et al., 2021). The topographies showed that the artifact caused by jaw clenching exhibited a broader spatial extent compared to normal hemodynamic response, primarily concentrating at the temporal muscle regions. These results demonstrated that jaw clenching can introduce hemodynamic-response-like artifacts in fNIRS signals, but with a larger amplitude and a broader spatial extent compared with the normal hemodynamic response. Similar responses in HbR, notably the task-evoked decreases, are also seen and shown in **Figure 4-3**, which resembles a typical response to sound stimuli overall the auditory cortices.

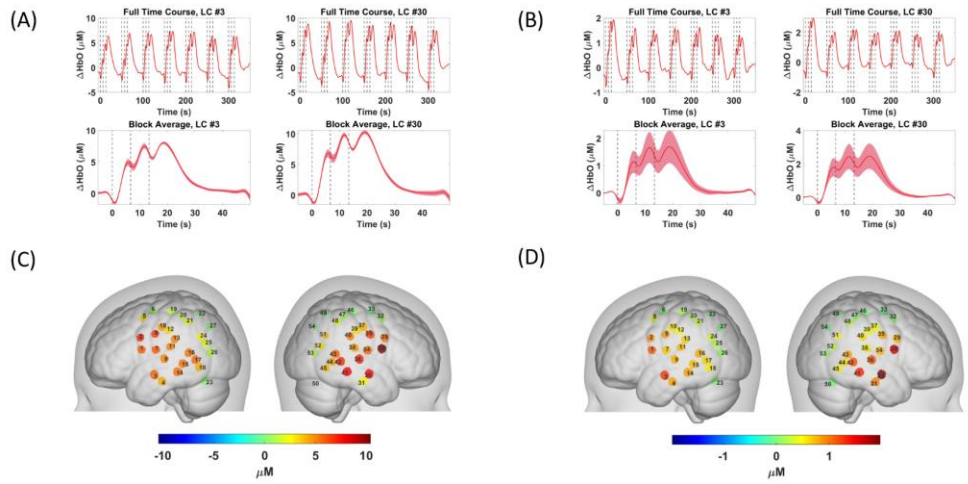

Figure 4-2: Task-evoked-alike fluctuations in HbO caused by jaw clenching. Full time courses and block averages of bilateral clenching channels at the session level (A) and group level (B). Topographies of amplitudes averaged across 5 to 15 s of all LS channels at the session level (C) and group level (D). The shaded areas represent the standard error across blocks in (A) and across subjects in (B).

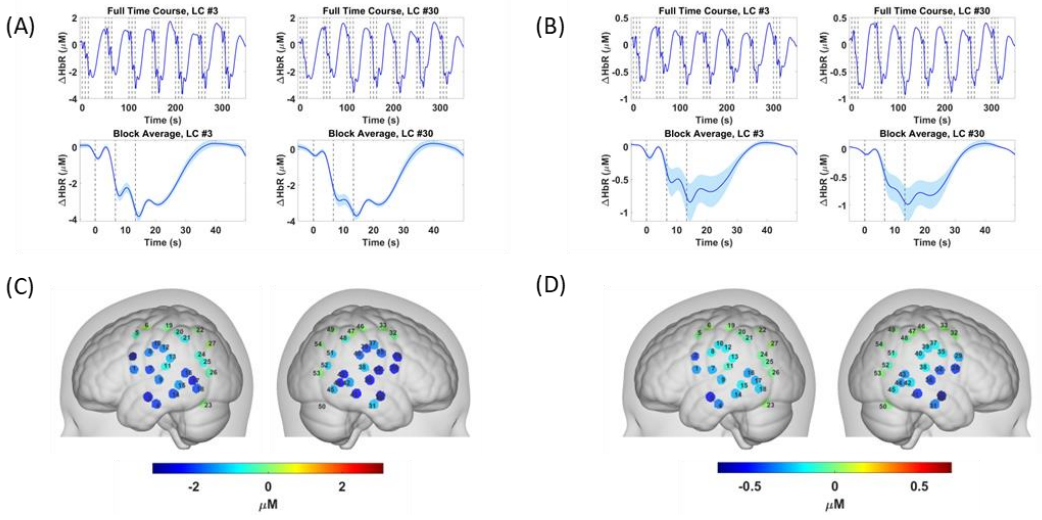

Figure 4-3: Task-evoked-alike fluctuations in HbR caused by jaw clenching. Full time courses and block averages of bilateral clenching channels at the session level (A) and group level (B). Topographies of amplitudes averaged across 5 to 15 s of all LS

channels at the session level (C) and group level (D). The shaded areas represent the standard error across blocks in (A) and across subjects in (B).

In order to quantify the motion-related activity, **Figure 4-4A** shows the group-level GVTD measure which reflects the co-fluctuations across all channels along the entire clenching session. The GVTD time course highly correlates with the group-level full time course shown in **Figure 4-2B** and demonstrates global fluctuations consistent across seven consecutive blocks. **Figure 4-4B** shows that the mean GVTD during the jaw clenching period (0 – 20 s) is significantly higher than that during the resting period (20 – 50 s), which indicates that there are global fluctuations across channels caused by the jaw clenching. The channels affected are mainly located at the temporal muscle region, as shown in **Figure 4-2D**. Channel 3 and 30 over the left and right auditory cortices, respectively, were designated as the clenching channels.

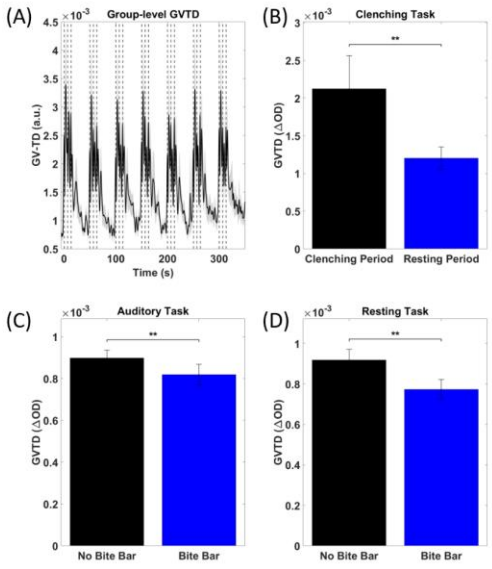

Figure 4-4: Global variance of temporal derivatives (GVTD) of fNIRS measurements. (A) Group-level GVTD along the entire jaw clenching session. (B) Mean GVTD values

during the jaw clenching period and the resting period. (C) and (D) Mean GVTD values across the entire session without and with a customized bite bar addressed to each subject in auditory and resting tasks. The dash lines indicate jaw-clenching movements. The asterisk indicates significant differences in the two-tailed paired-sample t-test.

Furthermore, we have investigated the spatio-temporal pattern of the optical signals during the jaw-clenching movements (**Figure 4-5**). To illustrate how the PCA-GLM reduce the hemodynamic-response-like fluctuations caused by jaw clenching, the results of PCA of one session (same session as in **Figure 4-2A**) were used as an example. The PCA-GLM framework firstly performs separate PCA analyses on LS channels and SS channels to identify a PC-LS component and a PC-SS component. The time course and spatial pattern of PC-LS demonstrate that the jaw-clenching-modulated fluctuations are well captured in PC-LS. **Figure 4-5A** shows the variance percentage accounted for by each component in the data of LS channels. After applying PCA on the LS recording acquired at the clenching task, a prominent component was identified such that the 1st component explained more than 95% of the total variance in the data. The time course of PC-LS is shown in **Fig. 4-5B**, which highly resembles the full time course shown in **Figure 4-2A** and is consistent with the high GVTD measure in **Figure 4-4A**. Moreover, the 1st PC presents a homogenous distribution located over the temporal muscle region (**Figure 4-5C**), indicating a high coefficient of spatial uniformity which is a necessary prerequisite for the success of the denoising PCA-GLM method (Zhang et al., 2021). Instead of directly utilizing the PC-LS as a regressor in the GLM, PC-LS was used to identify a principal component from the SS measurements which are more sensitive to superficial tissues (including temporal muscle). The PC that has the highest temporal

correlation with the PC-LS was determined as the PC-SS and then used as a regressor in the GLM to regress out the motion artifacts caused by jaw clenching.

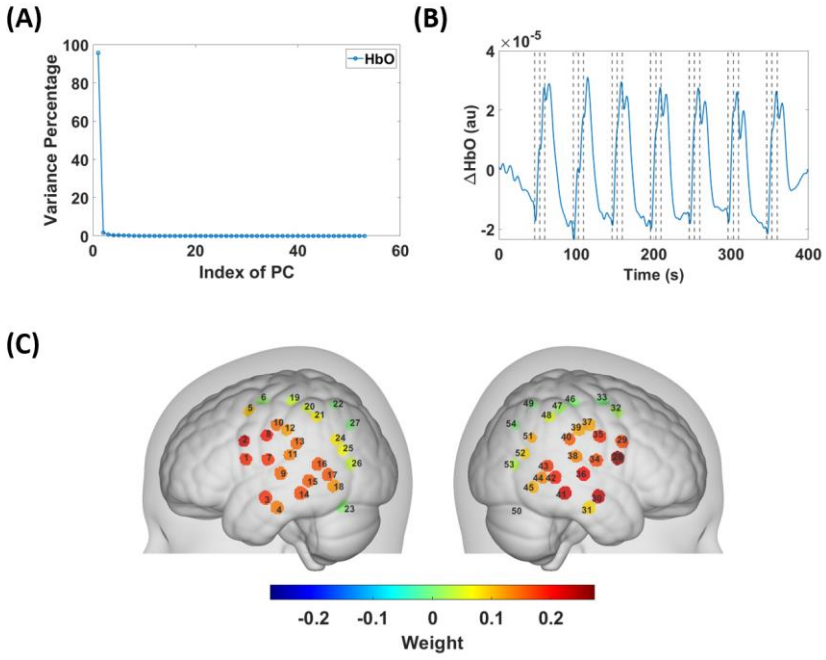

Figure 4-5: Spatio-temporal pattern of the fNIRS signals during clenching task. (A) Variance explained by components in PCA. (B) The time course of PC-LS captures the clenching motions. (C) The spatial pattern of PC-LS presents spatial uniformity.

4.3.2 Controlling Clenching-related Artifacts in Auditory Tasks

Figure 4-6 shows the data during auditory tasks at the group level. **Figure 4-6A** shows the auditory-evoked response by comparing the mean amplitude during an auditory stimuli window (5 – 18 s) to that during a silence window (20 – 30 s). There are several activated channels in both hemispheres while LS channel 3 located at the middle temporal gyrus is the most activated. The LS channel 3 is therefore identified as the channel of interest in terms of auditory-evoked response in the following analyses. In addition, LS channel 25 located at the angular gyrus, which is expected to not show activation, is

selected as a channel of interest to study the effects of a bite bar and PCA-GLM on non-auditory-related channels.

As indicated in **Figure 4-4C,** the mean GVTD during the entire session is significantly lower while a bite bar is applied to each subject in the auditory task. This indicates that the individually customized bite bar proposed in this study is effective in suppressing jaw clenching movements and thus reducing global fluctuations in the fNIRS signals. **Figures 4-6B and C** show the block averages under four different conditions. In LS channel 3, the block average more resembles an auditory-evoked response with a bite bar applied. Meanwhile, the block average has a higher amplitude after PCA-GLM. In LS channel 25, the block average shows a negative response regardless of whether a bite bar is applied with No Correction. In addition to motion artifacts, there might be another factor, i.e., blood stealing effects (Harel et al., 2002; Shmuel et al., 2002) that might have contributed to the negative response. The activation in the auditory cortex could cause a decreased cerebral blood flow in other neighboring regions. After PCA-GLM is applied, LS channel 25 shows a relatively flattened response, which aligns with the expectation that no activation in the angular gyrus during an auditory task. To quantify the improvements on LS channels 3 and 25 introduced by a bite bar and PCA-GLM, respectively, four metrics were used to measure the goodness of the fNIRS signals. **Figure 4-6B** shows that in LS channel 3 the beta value, CNR and mean amplitude are significantly higher while within-subject SD is significantly lower with a bite bar applied. **Figure 4-6C** shows that in LS channel 25 the beta value, CNR and mean amplitude have large negative magnitudes with No Correction and much smaller magnitudes after PCA-GLM. Meanwhile, the within-subject SD is significantly lower after PCA-GLM. These

results suggest that a bite bar improves the detection of auditory response in auditory-related channels while PCA-GLM reduces the spurious activation due to jaw clenching in non-auditory-related channels.

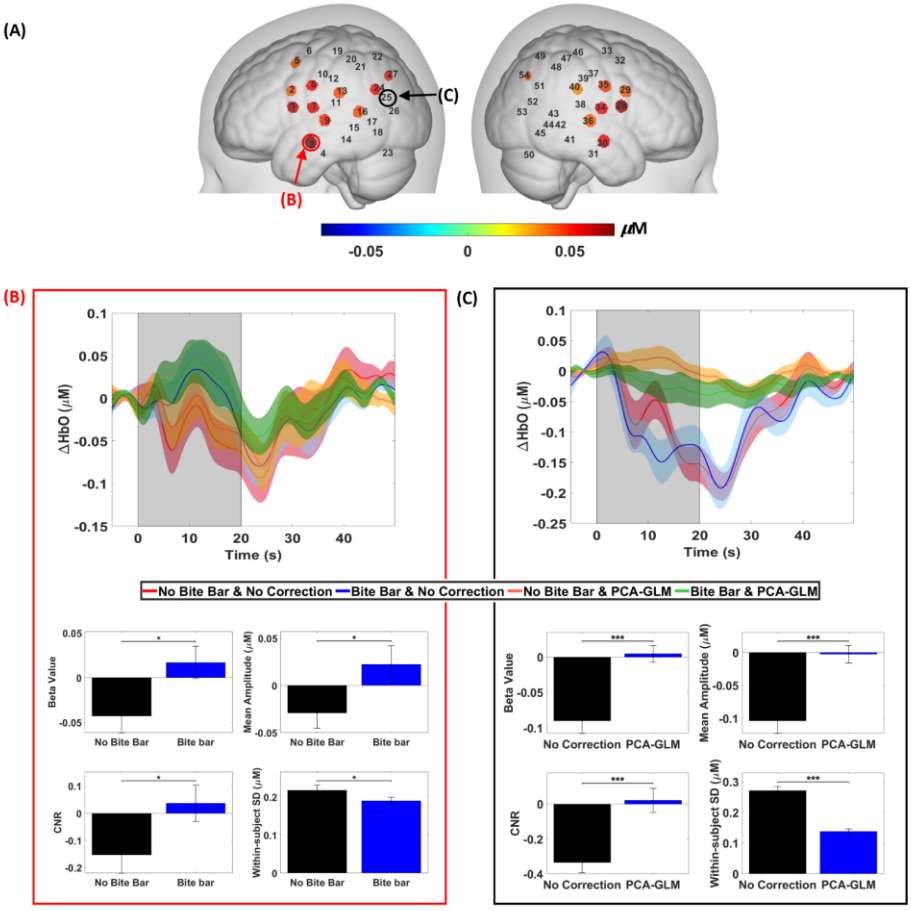

Figure 4-6: Improvements in HbO signals by a bite bar and PCA-GLM in representative channels. (A) Auditory-evoked response map. The differences in mean amplitudes between a sound window (5 – 18 s) and a silence window (20 – 30 s). Only LS channels with significant differences were shown (q<0.05, FDR corrected). (B) Comparison of block averages under four different conditions in LS channel 3, a representative channel of clenching artifacts. (C) Comparison of block averages under four different conditions in LS channels 25, a representative channel of superficial activity. Quantitative metrics

for evaluation include the beta value, mean amplitude during the task period, contrast-to-noise ratio (CNR), and within-subject standard derivation (SD). * indicates $p < 0.05$, *** indicates $p < 0.001$.

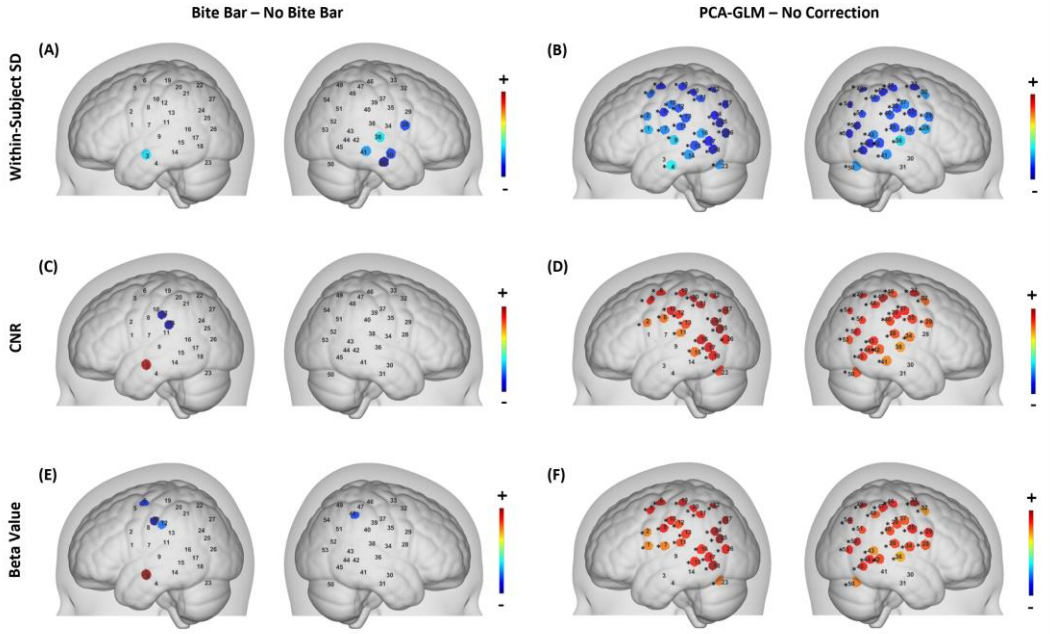

Figure 4-7: Topographies of improvements in fNIRS signals introduced by a bite bar and PCA-GLM. Four evaluation metrics are calculated, including within-subject standard derivation (A, B), contrast-to-noise ratio (C,D), and beta value of the GLM regressor for auditory stimuli (E,F). comparisons are made between bite-bar vs. without-bite-bar (A,C,E), and PCA-GLM vs. without-correction (B,D,F). Only channels with significant differences in comparison ($p < 0.05$) are shown. * indicates channels with a significant difference after multiple comparisons correction ($q < 0.05$).

4.3.3 Controlling Clenching-related Artifacts During Resting State

Figure 4-4D shows that the mean GVTD across the entire session is significantly lower with a bite bar applied to each subject in the resting task. **Figures 4-8A and B** show

the functional connectivity seeded at LS channel 3 with [No Bite Bar, No Correction] and [Bite Bar, PCA-GLM], respectively. **Figure 4-8C** shows the differences in functional connectivity between [Bite Bar, PCA-GLM] and [No Bite Bar, No Correction]. The visualization was generated with BrainNet Viewer (Xia et al., 2013). There is significantly increased connectivity between LS channel 3 in the left hemisphere and LS channels 30, 36 and 41 in the right hemisphere, which demonstrates that bite bar and PCA-GLM jointly increase the cross-hemisphere functional connectivity between homologous auditory cortices.

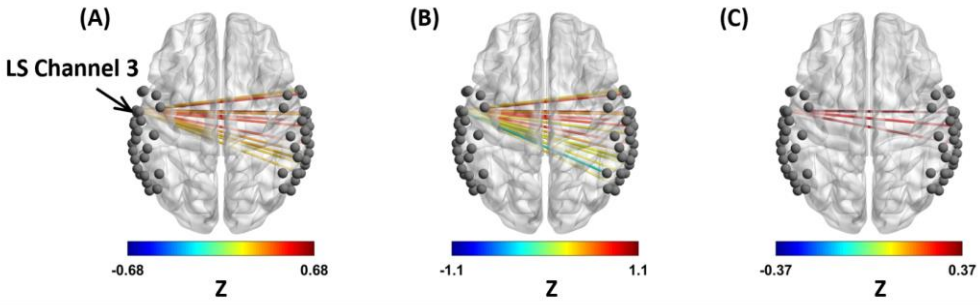

Figure 4-8: Enhanced cross-hemisphere resting-state functional connectivity by a bite bar and PCA-GLM. (A) and (B) Functional connectivity seeded at LS channel 3 with [No Bite Bar, No correction] and [Bite Bar, PCA-GLM] respectively. (C) The differences in functional connectivity between [No Bite Bar, No correction] and [Bite Bar, PCA-GLM]. The strength of functional connectivity is color-coded. The line connecting two channels indicates significant functional connectivity in (A) and (B) and differences in (C) ($q<0.05$, FDR corrected).

4.4 Discussions

Due to the advantages of portability, cost-effectiveness, low operating noise and compatibility with medical implanted devices (e.g., cochlear implant) (Chiarelli et al.,

2017; Luke et al., 2021; Scholkmann et al., 2014), fNIRS has seen increasing applications in studying the speech and auditory function (Sevy et al., 2010; Wan et al., 2018). However, there are still several confounding factors in fNIRS signals, including interferences from superficial layers of the head, systemic physiological noises and motion artifacts (von Lühmann et al., 2019; von Lühmann et al., 2020; Zhang et al., 2021). Although less vulnerable to head movements, fNIRS can still suffer from jaw movements such as speech speaking and voluntary jaw clenching, which can cause contractions of the temporalis muscle (Novi et al., 2020; Schecklmann et al., 2017). The jaw movements could result in blood flow changes in the temporal muscle as well as relative movements between the optodes and the scalp, leading to artifacts in the fNIRS signals (Schecklmann et al., 2017). Although many previous studies have investigated the impact and correction of head movements (Cui et al., 2010; Fishburn et al., 2019; Izzetoglu et al., 2010; Scholkmann et al., 2010), the control and correction of jaw movements in fNIRS recordings remain largely unclear (Novi et al., 2020; Schecklmann et al., 2017). This study showed that the motion artifacts caused by voluntary jaw clenching can introduce hemodynamic-response-like artifacts that resemble task-evoked responses in motor and auditory tasks.

Our results showed that jaw clenching could introduce hemodynamic response-like artifacts that resemble task-evoked activations into fNIRS signals. Specifically, the jaw clenching introduces a task-activation-like increase in HbO in a pair of symmetric channels located at the temporal cortex (shown in **Figure 4-2**), which is consistent with the previous literature (Novi et al., 2020; Schecklmann et al., 2017). These artifacts could be misinterpreted as evoked auditory responses in an auditory task and lead to spurious

activations in the analyses. This has therefore underlined the importance of the control, detection and removal of the jaw clenching artifacts in fNIRS recordings. The quantitative metric GVTD (**Figure 4-4A**) which measures the coherent fluctuations across channels reflects a time course highly correlated to the group-level full time courses of concentration changes (**Figure 4-2B**), which indicates the jaw clenching introduces hemodynamic-response-like artifacts broadly in LS channels located at the temporal muscle region. The GVTD is significantly higher during the jaw clenching period than during the resting period (**Figure 4-2B**), which supported that the global fluctuations are caused by the jaw clenching rather than global activity during the resting state.

We then validated the previous established PCA-GLM framework in correcting the jaw-clenching-modulated artifacts. PCA analyses were performed on data of LS channels and SS channels separately to identify PC-LS and PC-SS. The results demonstrated that PC-LS shows a time course (**Figure 4-5B**) resembling the group-level time course in the clenching task (**Figure 4-2B**) as well as a spatial pattern concentrating at the temporal muscle region (Morais et al., 2017; Volkening et al., 2016). The time course and spatial pattern of PC-LS together demonstrate that the jaw-clenching-modulated fluctuations are well reflected in PC-LS.

In addition to applying motion artifact correction techniques, we think it would be beneficial to control the jaw clenching movements during the recordings to prevent the appearance of motion artifacts in the fNIRS signals. To achieve this, we designed a bite bar consisting of a rectangle plastic plate and vinyl polysiloxane putty (**Figure 4-1A**) customized for each participant and repeated the auditory and resting tasks with and without applying the bite bar. The results showed that the mean GVTD during the entire

session is significantly lower while a bite bar is applied to each subject in both the auditory and resting tasks (**Figures 4C and D**), which indicates the individually customized bite bar is effective in suppressing the jaw clenching movements and reducing global fluctuations across channels. Furthermore, the block average of LS channel 3 located at the temporal gyrus more resembles an auditory-evoked response with a bite bar applied (**Figure 4-6B**). In LS channel 25 located at the angular gyrus, which is expected to not show activation during an auditory task, shows a relatively flattened response after PCA-GLM is applied (**Figure 4-6C**). Quantitatively, in LS channel 3, the beta value, CNR and mean amplitude are significantly higher while within-subject SD is significantly lower with a bite bar applied (**Figure 4-6B**). In LS channel 25, the beta value, CNR and mean amplitude have much smaller magnitudes after PCA-GLM while showing large negative amplitudes with No Correction. Meanwhile, the within-subject SD is significantly lower after PCA-GLM is applied (**Figure 4-6C**). These results suggest that a bite bar improves the detection of auditory response in auditory-related channels while PCA-GLM reduces the spurious activation due to jaw clenching in non-auditory-related channels.

The results of the resting-state data showed that there is significantly increased connectivity between LS channel 3 in the left hemisphere and LS channels 30, 36 and 41 in the right hemisphere, which indicates that bite bar and PCA-GLM jointly increase the cross-hemisphere functional connectivity between homologous auditory cortices (**Figure 4-8**). These results indicate that the bite bar can help to suppress jaw clenching movements and introduce improvements in mapping functional connectivity.

Our results suggest that future fNIRS studies should instruct participants to refrain from clenching the jaw or chewing gum during the recordings or consider utilizing an individually customized bite bar proposed in this study to forcefully suppress jaw clenching unless the task engages certain movements of the jaw (e.g., speech). Furthermore, carefulness must be taken to address the jaw clenching artifacts in the data processing, even verbal instruction or a bite bar has been implemented to reduce the jaw clenching. Motion correction techniques should be employed to remove the motion artifacts caused by jaw clenching. For example, the combination of a bite bar in the data collection stage and PCA-GLM in the data processing stage is shown to be effective in improving the fNIRS signals in this study.

4.5 Conclusions

In summary, we have characterized the effects of jaw clenching on fNIRS signals, proposed and validated an individually customized bite bar to suppress the jaw clenching, and validated our previously established PCA-GLM method in removing jaw-clenching motion artifacts. This study underlined the importance of controlling jaw clenching and provide a possible solution integrating a bite bar in the data collection stage and PCA-GLM in the data processing stage. The characterization of jaw-clenching artifacts and the validation of a possible solution presented in this study will benefit the accurate understanding of the auditory mechanisms in normal healthy subjects and patients.

5 Chapter 5 Conclusions and Future Work

5.1 Conclusions

This chapter discusses and summarizes my research work towards establishing fNIRS as a routine tool in clinical use presented in this dissertation.

Noninvasive functional neuroimaging techniques have become important tools for neuroscience research and clinical use. fMRI and EEG are two neuroimaging modalities commonly utilized in monitoring the human brain under normal and diseased conditions. These two techniques have their own merits and limitations. fMRI has high spatial resolution but low temporal resolution, while EEG has high temporal resolution but low spatial resolution. In this context, fNIRS, as a non-invasive optical imaging technique with moderate spatial and temporal resolution and advantages in robustness against head motion, portability, cost-effectiveness and compatibility with medical electronic implants, has drawn great interest in research and clinical applications. However, the interferences from head motion, superficial blood flow and systemic physiological activity have comprised the image quality of fNIRS. Most of the existing methods were developed in a partial montage that only includes a few channels (Gagnon et al., 2011; Zhang et al., 2007; Zhang et al., 2005), or covers only part of the cortex (Sato et al., 2016; Zhang et al., 2016). In order to tap the full potential of fNIRS, we developed an automatic denoising method namely PCA-GLM and validated its efficacy in improving the whole-head fNIRS recordings. The PCA-GLM method will facilitate the applications of fNIRS in monitoring activations from multiple distant regions in a complex task or coherent spontaneous activity across functionally connected areas in a resting-state task in research and clinical applications.

Since the first finding revealed that the low-frequency oscillations (<0.1 Hz) in the BOLD signals measured by fMRI are temporally correlated in motor cortex and other regions related to motion function under the resting state (Biswal et al., 1995), a great deal of effort has been dedicated to the research of resting-state functional connectivity and resulted in significant advances in the understanding of the functional organization, aging process and neurological disorders of the human brain (Zhang and Raichle, 2010). Previous fNIRS studies have successfully mapped the resting-stated functional connectivity with seed-based correlation analysis or independent component analysis (ICA) in different brain systems, such as prefrontal (Mesquita et al., 2010), sensorimotor (Lu et al., 2010; Mesquita et al., 2010; White et al., 2009), auditory (Lu et al., 2010) and visual (Mesquita et al., 2010; White et al., 2009) networks. Mesquita et al. (2010) utilized a sparse whole-head montage while others used partial montages that only covered a part of the head (Lu et al., 2010; White et al., 2012; White et al., 2009). All these studies have demonstrated fNIRS's capability of mapping functional connectivity in frontal, sensorimotor, auditory and visual networks. However, the higher-order large-scale brain networks such as default mode network (DMN), dorsal attention network (DAN) and frontoparietal control network (FPCN) have been shown to be associated with the aging process and neuropsychiatric disorders including Alzheimer's disease, depression and schizophrenia (Andrews-Hanna et al., 2007; Greicius, 2008; Zhang and Raichle, 2010). In this work, we have for the first time demonstrated that fNIRS as a broadly accessible modality can image the resting-state functional connectivity in the posterior midline, prefrontal and parietal structures of the default mode network in the human brain by cross-modal comparison with fMRI. These outcomes have validated fNIRS capability in

mapping large-scale resting-state functional connectivity with distributed spatial patterns as identified in fMRI studies (Damoiseaux et al., 2006; Thomas Yeo et al., 2011). Therefore, the whole-head fNIRS's capability in mapping functional connectivity between distributed cortical hubs as demonstrated in our work provides an economic and practically feasible option for assessing the anterior-posterior DMN connectivity as biomarkers for monitoring aging and Alzheimer's disease in large populations.

Despite the fact that intrinsic oscillations of the vascular networks (Drew et al., 2020; Mateo et al., 2017) and other physiological oscillations such as respiration, cardiac pulsation and cerebrospinal fluid may also contribute to the measured hemodynamics in the upper frequencies (Liu, 2016), our understanding of the human brain functional connectivity has been primarily established by fMRI at sub-hertz sampling rates for the activity below 0.1 Hz (Biswal et al., 1996; Cordes et al., 2001; Mitra et al., 1997). However, it is still poorly understood how the oscillations that exist beyond the safely sampled range could contribute to the network organization via the aliased effects. In this work, we have shown that a sampling rate lower that is insufficient to sample the respiration and cardiac pulse frequency will introduce spatially organized aliased connectivity to RSFC. Furthermore, our data-driven analysis has revealed that the aliasing effect is seed- and region-dependent and that the resulted spurious connectivity exists within the DMN regions and extends beyond in other cortical areas, appearing as aliased networks. Since the aliased functional connectivity patterns may obscure our current understanding, accurate imaging without aliasing is especially important in understanding AD stages, because of the high comorbidity of vascular diseases in aging populations. Despite that a low sampling has been widely used in similar fMRI studies, our findings

have emphasized that maintaining a sufficiently high sampling rate of fNIRS is crucial, especially when RSFC of DMN is considered as a biomarker.

fNIRS has become of great interest in the neuroscience community in studying the auditory function in healthy subjects and patients with hearing loss (Pollonini et al., 2014; Saliba et al., 2016). For example, fNIRS can be used to detect the auditory response in infant cochlear implant users who are unable to verbally communicate their hearing and comfort when audiologists adjust the sound levels (Bortfeld, 2019). A better understanding of auditory perception mechanisms of normal sound and cochlear stimuli can facilitate the early intervention of hearing loss in infants and therefore help to reserve and develop their speech and auditory function. There are several critical confounding factors in fNIRS signals, including interferences from superficial layers of the head, systemic physiological noise and motion artifacts (von Lühmann et al., 2019; von Lühmann et al., 2020; Zhang et al., 2021). Although less vulnerable to head movements, fNIRS can still suffer from jaw movements such as speech speaking and voluntary jaw clenching, which can cause contractions of the temporalis muscle (Novi et al., 2020; Schecklmann et al., 2017). The jaw movements could result in blood flow changes in the temporal muscle as well as relative movements between the optodes and the scalp, leading to artifacts in the fNIRS signals (Schecklmann et al., 2017). While many previous studies have investigated the impact and correction of head movements (Cui et al., 2010; Fishburn et al., 2019; Izzetoglu et al., 2010; Scholkmann et al., 2010), the effect and especially handling of jaw movements in fNIRS signals remain largely unclear (Novi et al., 2020; Schecklmann et al., 2017). In this work, we have characterized the effects of jaw clenching on fNIRS signals and demonstrated that the resulted motion artifacts

resemble the task-evoked activations. These findings underline the importance of controlling, detecting and removing the jaw clenching artifacts in fNIRS recordings. To suppress the jaw clenching movements, we have designed a bite bar customized for each individual. We then demonstrated that the customized bite bar and PCA-GLM method can effectively reduce the motion artifacts caused by jaw clenching and improve the detection of auditory response and the mapping of functional connectivity. The characterization of jaw clenching artifacts and the validation of a possible solution presented in this work will benefit the accurate understanding of the auditory mechanisms in normal healthy subjects and patients, which will facilitate the early intervention of hearing loss to reserve patients' speech and auditory function.

5.2 Future Work

One important direction of future work based on my dissertation is towards applying the fNIRS for clinical applications, possibly in combination with EEG. My dissertation has fruited three pilot clinical applications of fNIRS, including one that has concluded the experimental work and two that are ongoing. One study was to use fNIRS in measuring the auditory responses to programmed stimuli in cochlear implant users, in collaboration with the Heart for Hearing Institute. Another ongoing study is to use fNIRS and concurrent EEG in measuring the impaired neurovascular coupling in ovarian cancer patients receiving chemotherapy treatment, in collaboration with OU Stephenson Cancer Center. One other study that was recently initiated is to use fNIRS and concurrent EEG in measuring the impaired neurovascular coupling in epileptic patients, in collaboration with the OU Department of Neurosurgery.

In addition to working towards clinical applications, my dissertation has also pointed out areas where further development and/or improvement are needed. One aspect is to continually improve the denoising algorithm. Our PCA-GLM denoising method utilized the auxiliary recordings of pulse, respiration and movement. These additional nuisance regressors address the slow fluctuations in pulses, respiration and movement. Notably, this benefit of denoising was achieved by including zero-shift time courses of auxiliary measurement. Studies have shown that a time-embedding approach (von Lühmann et al., 2020) or considering a response function to the respiration (Birn et al., 2008) or cardiac pulses (Chang et al., 2009) might further capture their impact on cerebral hemodynamics. While these fluctuations are typical of less concern to a task in block design, they have been suggested to bias the organization of large-scale networks, especially in the resting brain (Mesquita et al., 2010; Yuan et al., 2013). Therefore, the incorporation of time-embedding approach and response functions of respiration and cardiac pulses in our PCA-GLM method is warranted to explore the benefits of these extra components.

The sample size (i.e., 13 subjects) is relatively small in this work. In addition, test-retest reliability of fNIRS in imaging the default mode network is critical but yet to be established in a moderate sample size. Furthermore, the characterization of RSFC and aliasing effects in whole-head fNIRS needs to be further demonstrated in a larger sample size similar to those in fMRI RSN studies, e.g., about 1000 participants in a study carried out by Thomas Yeo et al. (2011).

To avoid the aliasing effects on functional connectivity as depicted in this work, future fNIRS studies should sustain a sufficiently high sampling rate to critically sample the respiration and cardiac pulsation. A high sampling rate can be achieved by advancements

in the acquisition hardware but also ingenious ways of setting up the measurements. In the work of mapping RSFC, we used a NIRScout continuous-wave system (NIRX, Germany) of which the sampling rate primarily depends on the number of light sources. If the 34 light sources in our montage are illuminated sequentially, the sampling rate would be 62.5/34 = 1.84 Hz which is not sufficiently high enough to avoid the aliasing of cardiac pulsation. In order to maintain a high sampling rate with a large number of sources, we employed the parallel illumination in the NIRScout system (NIRX, Germany), which illuminated multiple sources in each single time step. To avoid optical crosstalk, we have manually selected the optimal source illumination based on the criterion that the distances between sources illuminated in the same time step should be larger than 9 cm so that each detector will primarily receive light from one emitter in a single time step. 34 light sources were illuminated in 10 time steps, resulting in a sampling rate of 6.25 Hz which is high enough to critically sample respiration and cardiac pulsation. The parallel illumination has significantly accelerated the data acquisition. However, the selection of illumination sequence demanded manual effort and might not achieve optimal performance in reducing optical crosstalk since it was based on distances between sources rather than the sensitivity profile of channels. Therefore, in addition to advancements in acquisition hardware, future high-density whole-head fNIRS studies can also benefit from an optimization tool that can generate the optimal illumination sequence based on forward light modeling of the input montage, to achieve a high sampling rate while using high-density optodes array.

With the advancements in hardware and the growing interest in developing high-density fNIRS with full head coverage, future RSFC studies with fNIRS will benefit from

a large field of view and improved image quality. However, the increased numbers of sources and detectors in a whole-head configuration can add the weight borne by the subject and cause discomfort during the recordings. This is unwanted especially in RSFC studies because the pain or discomfort can potentially drive the subject to deviate from the resting state and introduce bias in mapping the RSNs (Necka et al., 2019; Otti et al., 2013; Valet et al., 2004). Although we have used a desk-mounted arm to hold the optodes during recordings, comfortability could be further improved upon the current setup with an ergonomic support design (Eggebrecht et al., 2014).

A large number of sources can also increase the dosage of near-infrared light emitted into the brain and raise the temperature of the brain tissues (Bozkurt and Onaral, 2004). The temperature changes might modulate the level of cerebral activity. Recent studies have also shown that near-infrared light photobiomodulation can modulate functional connectivity via a non-thermal mechanism (Dmochowski et al., 2020; Urquhart et al., 2020; Wanniarachchi et al., 2021). Future high-density whole-head fNIRS studies can potentially benefit from a tool that can quantify the light dosage injected into the brain and help to control the modulation effects on functional connectivity by the near-infrared light.

Noteworthy, while the respiration and cardiac pulsation have been previously considered as noises contaminating the BOLD functional connectivity measured by fMRI, recent studies have suggested that these physiological pulsations have great potential as clinical biomarkers of brain diseases (Chen et al., 2020a; Raitamaa et al., 2021; Tong et al., 2019). The advantage of an inbuilt higher sampling rate over fMRI will enable fNIRS to spectrally separate LFOs, respiration and cardiac pulsation, and to

potentially provide cardiovascular biomarkers of neuropsychiatric diseases complementary to RSFC. Future work is warranted to study the network organization of physiological pulsations.

The interpretation of hemodynamic signals in fNIRS and BOLD signals in fMRI relies on the relationship which relates the neural activity to the accompanying hemodynamic response (Arthurs and Boniface, 2002). Therefore, an understanding of the neurovascular coupling process is crucial for the accurate interpretation of functional imaging data. When inferring the neural activation from BOLD or hemodynamic signals, the impulse response induced by neural activation has been commonly modelled as a hemodynamic response function (HRF), which rises shortly after the neural activation with a time-to-peak of about 5 s (Friston et al., 1994; Glover, 1999; Huettel et al., 2004). This method has therefore assumed that the HRF is consistent across brain regions and subjects. However, studies have reported that HRF varies across brain regions (Aguirre et al., 1998; Hong, 2014; Jasdzewski et al., 2003b), ages (Huettel et al., 2001; Jacobs et al., 2008), and brain pathologies such as stroke (Bonakdarpour et al., 2007; Siegel et al., 2016), traumatic brain injury (Mayer et al., 2014; Werner and Engelhard, 2007) and Alzheimer's disease (Rombouts et al., 2005; Sperling et al., 2003). Subject-specific and voxel-specific HRFs have been proven to provide more accurate detection of epilepsy (Kang et al., 2003; Lu et al., 2006). Therefore, the HRF should be estimated with variability to account for the effects of the abovementioned conditions. The variant HRF can facilitate more accurate interpretations of BOLD signals but also provide biomarkers of neurological and psychiatric diseases and facilitate early intervention. Future studies are warranted to establish a multimodal data fusion framework for a whole-head

simultaneous fNIRS-EEG multimodal imaging, which will provide a full felid of view for mapping functional connectivity but also enable studying the neurovascular coupling that relates the neural activity with hemodynamic activity.

6 Chapter 6: Products of This Dissertation

6.1 Peer-Reviewed Publications

1. [Under review] **Zhang, F.,** Khan, A. F., Ding, L., Yuan, H., Network Organization of Resting-State Cerebral Hemodynamics and Their Aliasing Contributions Measured by Functional Near-Infrared Spectroscopy.
2. [Under review] **Zhang, F.**, Reid, A., Schroeder, A., Ding, L., Yuan, H., Controlling Clenching-Related Motion Artifacts in Functional Near-Infrared Spectroscopy.
3. [In preparation**] Zhang, F.**, Chen. Y., Ma, J., Wolfe, J., Ding, L., Yuan, H., Assessment of Auditory Response in Cochlear Implant Users.
4. [In preparation] **Zhang, F.**, Khan, A. F., Ding, L., Yuan, H., Neurovascular Coupling in Human Brain Measured by Simultaneous fNIRS and EEG.
5. Khan, A. F., **Zhang, F.**, Shou, G., Yuan, H., Ding, L., Transient brain-wide coactivations and structured transitions revealed in hemodynamic imaging data. *NeuroImage*, 2022, 119460. DOI: doi.org/10.1016/j.neuroimage.2022.119460
6. **Zhang, F.**, Reid, A., Schroeder, A., Cutter, M., Kim, K., Ding, L., Yuan, H., Clenching-Related Motion Artifacts in Functional Near-Infrared Spectroscopy in the Auditory Cortex. 44th Annual International Conference of the IEEE Engineering in Medicine and Biology Society, 2022.
7. **Zhang, F.**, Cheong, D., Khan, A. F., Chen, Y., Ding, L., & Yuan, H. (2021). Correcting Physiological Noise in Whole-Head Functional Near-Infrared Spectroscopy. *Journal of Neuroscience Methods*, 109262. DOI: doi.org/10.1016/j.jneumeth.2021.109262

8. Khan, A. F., **Zhang, F.**, Yuan, H., & Ding, L. (2021). Brain-wide functional diffuse optical tomography of resting state networks. *Journal of Neural Engineering*, *18*(4), 046069. DOI: https://doi.org/10.1088/1741-2552/abfdf9
9. Khan, A. F., **Zhang, F.**, Yuan, H., Ding, L., Brain-Wide Diffuse Optical Tomography Based on Cap-Based, Whole-Head fNIRS Recording. 43rd Annual International Conference of the IEEE Engineering in Medicine and Biology Society, 2021. DOI: 10.1109/EMBC46164.2021.9630249.
10. Cheong, D.#, **Zhang, F.#**, Kim, K., Reid, A., Ding, L., Yuan, H., Task-Related Systemic Artifacts in Functional Near Infrared Spectroscopy. 42nd Annual International Conference of the IEEE Engineering in Medicine and Biology Society, 2020. DOI: 10.1109/EMBC44109.2020.9176366. (#These authors contributed equally.)
11. **Zhang, F.**, Cheong, D., Chen, Y., Khan, A. F., Ding, L., Yuan, H., Superficial Fluctuations in Functional Near-Infrared Spectroscopy. 41st Annual International Conference of the IEEE Engineering in Medicine and Biology Society, 2019. DOI: 10.1109/EMBC.2019.8856349.
12. Khan, A. F., **Zhang, F.**, Yuan, H., Ding, L., Dynamic Activation Patterns of the Motor Brain Revealed by Diffuse Optical Tomography (**selected as a Finalist**). 41st Annual International Conference of the IEEE Engineering in Medicine and Biology Society, 2019. DOI: 10.1109/EMBC.2019.8857370.

6.2 Published Conference Abstracts

1. Edwards, S., **Zhang, F.**, Wenger, M., Kuan-Celarier, A., Walker, J., Yuan, H., Treatment-related Cognitive Impairment and Neurovascular Coupling in Cancer Patients. Annual Meeting of the Biomedical Engineering Society, San Antonio TX, 2022.
2. **Zhang, F.**, Cheong, D., Khan, A. F., Chen, Y., Ding, L., Yuan, H., Correcting physiological noise in whole-head functional near-Infrared spectroscopy. 50th Annual Meeting of Society for Neuroscience, 2021.
3. Reid, A., Schroeder, A.J., **Zhang, F.**, Yuan, H., Controlling Movement-Related Artifacts During fNIRS Recordings. Annual Meeting of the Biomedical Engineering Society, Orlando GA, 2021.
4. Khan, A.F., **Zhang, F.**, Yuan, H., Ding, L., Cap-Based Brain-Wide Diffuse Optical Tomography of Resting-State Networks. 27th Annual Meeting of the Organization for Human Brain Mapping, Virtual Meeting, 2021.
5. Khan, A. F., **Zhang, F.**, Yuan, H., Ding, L., Interrogating Resting-State Networks with Brain-Wide Diffuse Optical Tomography (BW-DOT). 43rd Annual International Conference of the IEEE Engineering in Medicine and Biology Society, 2021.
6. Kim, K., **Zhang, F.**, Cheng, M., Reid, A., Cheong, D., Yuan, H., The Effects of Movement-Related Artifacts During fNIRS Recordings in the Auditory Cortex. BMES Annual Meeting, 2020.

7. Hanan, C., **Zhang, F.**, Ding, L., Yuan, H., Neurovascular Coupling in the Human Brain Measured by Simultaneous fNIRS and EEG. 4th OU-OUHSC Biomedical Engineering Symposium, 2020.
8. **Zhang, F.**, Cheong, D., Chen, Y., Khan, A. F., Ding, L., Yuan, H., Correcting Physiological Noises in Functional Near-Infrared Spectroscopy. 41st Annual International Conference of the IEEE Engineering in Medicine and Biology Society, 2019.
9. Khan, A. F., **Zhang, F.**, Yuan, H., Ding, L., Reconstructing Resting State Networks with Diffuse Optical Tomography. 41st Annual International Conference of the IEEE Engineering in Medicine and Biology Society, 2019.
10. Cheong, D., **Zhang, F.**, Yuan, H., Investigating the Regional Dependence of Short Channels in Functional Near-Infrared Spectroscopy. Annual Meeting of the Biomedical Engineering Society, 2019.
11. Cheong, D., **Zhang, F.**, Yuan, H., High-Density Diffuse Optical Tomography of the Human Motor Cortex. 50th Annual Meeting of the Biomedical Engineering Society, 2018.

6.3 Poster Presentations

1. **Zhang, F.**, Chen, Y., Cheong, D., Chen, Y., Wolfe, J., Ding, L., Yuan, H., Assessment of Auditory Responses in Cochlear Implant Users Using Functional Near-infrared Spectroscopy. The 4th Annual OU-OUHSC Biomedical Engineering Symposium, 2020.

2. **Zhang, F.**, Khan, A. F., Cheong, D., Chen, Y., Ding, L., Yuan, H., Mapping Functional Connectivity in The Human Brain Using Diffuse Optical Tomography. The 4th Annual OU-OUHSC Biomedical Engineering Symposium, 2020.
3. **Zhang, F.**, Khan, A. F., Cheong, D., Chen, Y., Ding, L., Yuan, H., Mapping Functional Connectivity in The Human Brain Using Diffuse Optical Tomography. Oklahoma Center for Neuroscience Research Retreat, 2020.
4. **Zhang, F.**, Cheong, D., Chen, Y., Khan, A. F., Ding, L., Yuan, H., Complementary Physiological Data Enhance Analysis of fNIRS Data during A Motor Task. 3rd OU-OUHSC Biomedical Engineering Symposium, 2019.
5. **Zhang, F.**, Csiszar, A., Ungvari, Z., Yabluchanskiy, A., Ding, L., Yuan, H., Neurovascular Coupling in the Human Brain Measured by Simultaneous fNIRS and EEG. Oklahoma Center for Neuroscience Research Retreat, 2019.
6. Reid, A., Cheong, D., Kim, K., **Zhang, F.**, Yuan, H., Physiological Noises in fNIRS Signals Measured from the Visual Cortex. 3rd OU-OUHSC Biomedical Engineering Symposium, 2019.
7. Kim, K., Cheong, D., Reid, A., **Zhang, F.**, Yuan, H., Physiological Noises in fNIRS Signals Measured from the Auditory Cortex. 3rd OU-OUHSC Biomedical Engineering Symposium, 2019.
8. **Zhang, F.**, Csiszar, A., Ungvari, Z., Yabluchanskiy, A., Yuan, H., Neurovascular Coupling in Human Brain Measured by Simultaneous fNIRS and EEG. 2nd OU-OUHSC Biomedical Engineering Symposium, 2018.

7 References

Aasted, C.M., Yücel, M.A., Cooper, R.J., Dubb, J., Tsuzuki, D., Becerra, L., Petkov, M.P., Borsook, D., Dan, I., Boas, D.A., 2015. Anatomical guidance for functional near-infrared spectroscopy: AtlasViewer tutorial. Neurophotonics 2, 020801.

Aihara, T., Shimokawa, T., Ogawa, T., Okada, Y., Ishikawa, A., Inoue, Y., Yamashita, O., 2020. Resting-State Functional Connectivity Estimated With Hierarchical Bayesian Diffuse Optical Tomography. Front Neurosci 14, 32.

Allen, E.A., Damaraju, E., Plis, S.M., Erhardt, E.B., Eichele, T., Calhoun, V.D., 2014. Tracking whole-brain connectivity dynamics in the resting state. Cerebral cortex 24, 663-676.

Andrews-Hanna, J.R., Snyder, A.Z., Vincent, J.L., Lustig, C., Head, D., Raichle, M.E., Buckner, R.L., 2007. Disruption of large-scale brain systems in advanced aging. Neuron 56, 924-935.

Bateman, R.J., Xiong, C., Benzinger, T.L., Fagan, A.M., Goate, A., Fox, N.C., Marcus, D.S., Cairns, N.J., Xie, X., Blazey, T.M., 2012. Clinical and biomarker changes in dominantly inherited Alzheimer's disease. N Engl J Med 367, 795-804.

Beckmann, C.F., DeLuca, M., Devlin, J.T., Smith, S.M., 2005. Investigations into resting-state connectivity using independent component analysis. Philosophical Transactions of the Royal Society B: Biological Sciences 360, 1001-1013.

Bénar, C.-G., Aghakhani, Y., Wang, Y., Izenberg, A., Al-Asmi, A., Dubeau, F., Gotman, J., 2003. Quality of EEG in simultaneous EEG-fMRI for epilepsy. Clinical neurophysiology 114, 569-580.

Benjamini, Y., Hochberg, Y., 1995. Controlling the false discovery rate: a practical and powerful approach to multiple testing. Journal of the Royal statistical society: series B (Methodological) 57, 289-300.

Bertero, M., De Mol, C., Pike, E.R., 1988. Linear inverse problems with discrete data: II. Stability and regularisation. Inverse problems 4, 573.

Birn, R.M., Diamond, J.B., Smith, M.A., Bandettini, P.A., 2006. Separating respiratory-variation-related fluctuations from neuronal-activity-related fluctuations in fMRI. Neuroimage 31, 1536-1548.

Birn, R.M., Smith, M.A., Jones, T.B., Bandettini, P.A., 2008. The respiration response function: the temporal dynamics of fMRI signal fluctuations related to changes in respiration. NeuroImage 40, 644-654.

Biswal, B., Deyoe, E.A., Hyde, J.S., 1996. Reduction of physiological fluctuations in fMRI using digital filters. Magnetic resonance in medicine 35, 107-113.

Biswal, B., Zerrin Yetkin, F., Haughton, V.M., Hyde, J.S., 1995. Functional connectivity in the motor cortex of resting human brain using echo‐planar MRI. Magnetic resonance in medicine 34, 537-541.

Boas, D.A., Dale, A.M., Franceschini, M.A., 2004. Diffuse optical imaging of brain activation: approaches to optimizing image sensitivity, resolution, and accuracy. Neuroimage 23, S275-S288.

Bortfeld, H., 2019. Functional near‐infrared spectroscopy as a tool for assessing speech and spoken language processing in pediatric and adult cochlear implant users. Developmental psychobiology 61, 430-443.

Boubela, R.N., Kalcher, K., Huf, W., Kronnerwetter, C., Filzmoser, P., Moser, E., 2013. Beyond noise: using temporal ICA to extract meaningful information from high-frequency fMRI signal fluctuations during rest. Frontiers in human neuroscience 7, 168.

Bozkurt, A., Onaral, B., 2004. Safety assessment of near infrared light emitting diodes for diffuse optical measurements. Biomed Eng Online 3, 9.

Brigadoi, S., Ceccherini, L., Cutini, S., Scarpa, F., Scatturin, P., Selb, J., Gagnon, L., Boas, D.A., Cooper, R.J., 2014. Motion artifacts in functional near-infrared spectroscopy: a comparison of motion correction techniques applied to real cognitive data. Neuroimage 85, 181-191.

Britz, J., Van De Ville, D., Michel, C.M., 2010. BOLD correlates of EEG topography reveal rapid resting-state network dynamics. Neuroimage 52, 1162-1170.

Brookes, M.J., Woolrich, M., Luckhoo, H., Price, D., Hale, J.R., Stephenson, M.C., Barnes, G.R., Smith, S.M., Morris, P.G., 2011. Investigating the electrophysiological basis of resting state networks using magnetoencephalography. Proceedings of the National Academy of Sciences 108, 16783-16788.

Buckner, R.L., Andrews-Hanna, J.R., Schacter, D.L., 2008. The brain's default network: anatomy, function, and relevance to disease. Ann N Y Acad Sci 1124, 1-38.

Buckner, R.L., Sepulcre, J., Talukdar, T., Krienen, F.M., Liu, H., Hedden, T., Andrews-Hanna, J.R., Sperling, R.A., Johnson, K.A., 2009. Cortical hubs revealed by intrinsic functional connectivity: mapping, assessment of stability, and relation to Alzheimer's disease. J Neurosci 29, 1860-1873.

Burle, B., Spieser, L., Roger, C., Casini, L., Hasbroucq, T., Vidal, F., 2015. Spatial and temporal resolutions of EEG: Is it really black and white? A scalp current density view. International Journal of Psychophysiology 97, 210-220.

Buxton, R.B., 2013. The physics of functional magnetic resonance imaging (fMRI). Reports on Progress in Physics 76, 096601.

Carius, D., Andrä, C., Clauß, M., Ragert, P., Bunk, M., Mehnert, J., 2016. Hemodynamic response alteration as a function of task complexity and expertise—an fNIRS study in jugglers. Frontiers in human neuroscience 10, 126.

Casey, B.J., Cannonier, T., Conley, M.I., Cohen, A.O., Barch, D.M., Heitzeg, M.M., Soules, M.E., Teslovich, T., Dellarco, D.V., Garavan, H., 2018. The adolescent brain cognitive development (ABCD) study: imaging acquisition across 21 sites. Developmental cognitive neuroscience 32, 43-54.

Cavedo, E., Lista, S., Khachaturian, Z., Aisen, P., Amouyel, P., Herholz, K., Jack Jr, C., Sperling, R., Cummings, J., Blennow, K., 2014. The road ahead to cure Alzheimer's disease: development of biological markers and neuroimaging methods for prevention trials across all stages and target populations. The Journal of prevention of Alzheimer's disease 1, 181.

Chang, C., Cunningham, J.P., Glover, G.H., 2009. Influence of heart rate on the BOLD signal: the cardiac response function. NeuroImage 44, 857-869.

Chen, J.E., Glover, G.H., 2015. BOLD fractional contribution to resting-state functional connectivity above 0.1 Hz. Neuroimage 107, 207-218.

Chen, J.E., Lewis, L.D., Chang, C., Tian, Q., Fultz, N.E., Ohringer, N.A., Rosen, B.R., Polimeni, J.R., 2020a. Resting-state "physiological networks". Neuroimage 213, 116707.

Chen, L.-C., Sandmann, P., Thorne, J.D., Herrmann, C.S., Debener, S., 2015. Association of concurrent fNIRS and EEG signatures in response to auditory and visual stimuli. Brain topography 28, 710-725.

Chen, W.L., Wagner, J., Heugel, N., Sugar, J., Lee, Y.W., Conant, L., Malloy, M., Heffernan, J., Quirk, B., Zinos, A., Beardsley, S.A., Prost, R., Whelan, H.T., 2020b. Functional Near-Infrared Spectroscopy and Its Clinical Application in the Field of Neuroscience: Advances and Future Directions. Front Neurosci 14, 724.

Chen, Y., Tang, J., Chen, Y., Farrand, J., Craft, M.A., Carlson, B.W., Yuan, H., 2020c. Amplitude of fNIRS resting-state global signal is related to EEG vigilance measures: A simultaneous fNIRS and EEG study. Frontiers in neuroscience, 1265.

Chen, Y., Tang, J.H., De Stefano, L.A., Wenger, M.J., Ding, L., Craft, M.A., Carlson, B.W., Yuan, H., 2022. Electrophysiological resting state brain network and episodic memory in healthy aging adults. Neuroimage 253, 118926.

Chiarelli, A.M., Zappasodi, F., Di Pompeo, F., Merla, A., 2017. Simultaneous functional near-infrared spectroscopy and electroencephalography for monitoring of human brain activity and oxygenation: a review. Neurophotonics 4, 041411.

Cordes, D., Haughton, V.M., Arfanakis, K., Carew, J.D., Turski, P.A., Moritz, C.H., Quigley, M.A., Meyerand, M.E., 2001. Frequencies contributing to functional connectivity in the cerebral cortex in “resting-state” data. American journal of neuroradiology 22, 1326-1333.

Cordes, D., Haughton, V.M., Arfanakis, K., Wendt, G.J., Turski, P.A., Moritz, C.H., Quigley, M.A., Meyerand, M.E., 2000. Mapping functionally related regions of brain

with functional connectivity MR imaging. American journal of neuroradiology 21, 1636-1644.

Cox, R.W., 1996. AFNI: software for analysis and visualization of functional magnetic resonance neuroimages. Computers and Biomedical research 29, 162-173.

Coyle, S.M., Ward, T.E., Markham, C.M., 2007. Brain–computer interface using a simplified functional near-infrared spectroscopy system. Journal of neural engineering 4, 219.

Cui, X., Bray, S., Reiss, A.L., 2010. Functional near infrared spectroscopy (NIRS) signal improvement based on negative correlation between oxygenated and deoxygenated hemoglobin dynamics. Neuroimage 49, 3039-3046.

Dale, A.M., Fischl, B., Sereno, M.I., 1999. Cortical surface-based analysis: I. Segmentation and surface reconstruction. Neuroimage 9, 179-194.

Damoiseaux, J.S., Beckmann, C.F., Arigita, E.J., Barkhof, F., Scheltens, P., Stam, C.J., Smith, S.M., Rombouts, S.A., 2008. Reduced resting-state brain activity in the "default network" in normal aging. Cereb Cortex 18, 1856-1864.

Damoiseaux, J.S., Rombouts, S., Barkhof, F., Scheltens, P., Stam, C.J., Smith, S.M., Beckmann, C.F., 2006. Consistent resting-state networks across healthy subjects. Proceedings of the National Academy of Sciences 103, 13848-13853.

Dehghani, H., Eames, M.E., Yalavarthy, P.K., Davis, S.C., Srinivasan, S., Carpenter, C.M., Pogue, B.W., Paulsen, K.D., 2009. Near infrared optical tomography using NIRFAST: Algorithm for numerical model and image reconstruction. Communications in numerical methods in engineering 25, 711-732.

Desjardins, A.E., Kiehl, K.A., Liddle, P.F., 2001. Removal of confounding effects of global signal in functional MRI analyses. Neuroimage 13, 751-758.

Dmochowski, G.M., Shereen, A.D., Berisha, D., Dmochowski, J.P., 2020. Near-Infrared Light Increases Functional Connectivity with a Non-thermal Mechanism. Cereb Cortex Commun 1, tgaa004.

Dong, S., Jeong, J., 2018. Improvement in recovery of hemodynamic responses by extended Kalman filter with non-linear state-space model and short separation measurement. IEEE Transactions on Biomedical Engineering 66, 2152-2162.

Drew, P.J., Mateo, C., Turner, K.L., Yu, X., Kleinfeld, D., 2020. Ultra-slow oscillations in fMRI and resting-state connectivity: neuronal and vascular contributions and technical confounds. Neuron 107, 782-804.

Duan, L., Zhang, Y.-J., Zhu, C.-Z., 2012. Quantitative comparison of resting-state functional connectivity derived from fNIRS and fMRI: a simultaneous recording study. Neuroimage 60, 2008-2018.

Eggebrecht, A.T., Ferradal, S.L., Robichaux-Viehoever, A., Hassanpour, M.S., Dehghani, H., Snyder, A.Z., Hershey, T., Culver, J.P., 2014. Mapping distributed brain function and networks with diffuse optical tomography. Nat Photonics 8, 448-454.

Erdogan, S.B., Yucel, M.A., Akin, A., 2014. Analysis of task-evoked systemic interference in fNIRS measurements: insights from fMRI. Neuroimage 87, 490-504.

Fischl, B., 2012. FreeSurfer. Neuroimage 62, 774-781.

Fischl, B., Sereno, M.I., Tootell, R.B., Dale, A.M., 1999. High‐resolution intersubject averaging and a coordinate system for the cortical surface. Human brain mapping 8, 272-284.

Fishburn, F.A., Ludlum, R.S., Vaidya, C.J., Medvedev, A.V., 2019. Temporal Derivative Distribution Repair (TDDR): A motion correction method for fNIRS. Neuroimage 184, 171-179.

Fox, M.D., Raichle, M.E., 2007. Spontaneous fluctuations in brain activity observed with functional magnetic resonance imaging. Nature Reviews Neuroscience 8, 700.

Franceschini, M.A., Fantini, S., Thompson, J.H., Culver, J.P., Boas, D.A., 2003. Hemodynamic evoked response of the sensorimotor cortex measured noninvasively with near‐infrared optical imaging. Psychophysiology 40, 548-560.

Franceschini, M.A., Joseph, D.K., Huppert, T.J., Diamond, S.G., Boas, D.A., 2006. Diffuse optical imaging of the whole head. Journal of biomedical optics 11, 054007.

Gaab, N., Gabrieli, J.D., Glover, G.H., 2008. Resting in peace or noise: Scanner background noise suppresses default‐mode network. Human brain mapping 29, 858-867.

Gagnon, L., Cooper, R.J., Yucel, M.A., Perdue, K.L., Greve, D.N., Boas, D.A., 2012. Short separation channel location impacts the performance of short channel regression in NIRS. Neuroimage 59, 2518-2528.

Gagnon, L., Perdue, K., Greve, D.N., Goldenholz, D., Kaskhedikar, G., Boas, D.A., 2011. Improved recovery of the hemodynamic response in diffuse optical imaging using short optode separations and state-space modeling. Neuroimage 56, 1362-1371.

Glover, G.H., 2011. Overview of functional magnetic resonance imaging. Neurosurgery Clinics 22, 133-139.

Glover, G.H., Li, T.Q., Ress, D., 2000. Image‐based method for retrospective correction of physiological motion effects in fMRI: RETROICOR. Magnetic Resonance in

Medicine: An Official Journal of the International Society for Magnetic Resonance in Medicine 44, 162-167.

Golestani, A.M., Kwinta, J.B., Khatamian, Y.B., Chen, J.J., 2017. The Effect of Low-Frequency Physiological Correction on the Reproducibility and Specificity of Resting-State fMRI Metrics: Functional Connectivity, ALFF, and ReHo. Front Neurosci 11, 546.

Greicius, M., 2008. Resting-state functional connectivity in neuropsychiatric disorders. Curr Opin Neurol 21, 424-430.

Greicius, M.D., Srivastava, G., Reiss, A.L., Menon, V., 2004. Default-mode network activity distinguishes Alzheimer's disease from healthy aging: evidence from functional MRI. Proc Natl Acad Sci U S A 101, 4637-4642.

Harel, N., Lee, S.P., Nagaoka, T., Kim, D.S., Kim, S.G., 2002. Origin of negative blood oxygenation level-dependent fMRI signals. J Cereb Blood Flow Metab 22, 908-917.

He, B., Liu, Z., 2008. Multimodal functional neuroimaging: integrating functional MRI and EEG/MEG. IEEE Rev Biomed Eng 1, 23-40.

He, B., Yuan, H., Meng, J., Gao, S., 2020. Brain–Computer Interfaces. In: He, B. (Ed.), Neural Engineering. Springer International Publishing, Cham, pp. 131-183.

Herold, F., Wiegel, P., Scholkmann, F., Müller, N.G., 2018. Applications of functional near-infrared spectroscopy (fNIRS) neuroimaging in Exercise–Cognition science: a systematic, Methodology-Focused review. Journal of clinical medicine 7, 466.

Hillman, E.M., 2014. Coupling mechanism and significance of the BOLD signal: a status report. Annu Rev Neurosci 37, 161-181.

Homae, F., Watanabe, H., Otobe, T., Nakano, T., Go, T., Konishi, Y., Taga, G., 2010. Development of global cortical networks in early infancy. J Neurosci 30, 4877-4882.

Hong, K.-S., Naseer, N., Kim, Y.-H., 2015. Classification of prefrontal and motor cortex signals for three-class fNIRS–BCI. Neuroscience letters 587, 87-92.

Hou, X., Zhang, Z., Zhao, C., Duan, L., Gong, Y., Li, Z., Zhu, C., 2021. NIRS-KIT: a MATLAB toolbox for both resting-state and task fNIRS data analysis. Neurophotonics 8, 010802.

Hsu, D., Marshall, G.A., 2017. Primary and Secondary Prevention Trials in Alzheimer Disease: Looking Back, Moving Forward. Curr Alzheimer Res 14, 426-440.

Hu, X., Le, T.H., Parrish, T., Erhard, P., 1995. Retrospective estimation and correction of physiological fluctuation in functional MRI. Magnetic resonance in medicine 34, 201-212.

Hu, Z., Liu, G., Dong, Q., Niu, H., 2020. Applications of resting-state fNIRS in the developing brain: a review from the connectome perspective. Frontiers in neuroscience 14, 476.

Huotari, N., Raitamaa, L., Helakari, H., Kananen, J., Raatikainen, V., Rasila, A., Tuovinen, T., Kantola, J., Borchardt, V., Kiviniemi, V.J., Korhonen, V.O., 2019. Sampling Rate Effects on Resting State fMRI Metrics. Front Neurosci 13, 279.

Huppert, T.J., Diamond, S.G., Franceschini, M.A., Boas, D.A., 2009. HomER: a review of time-series analysis methods for near-infrared spectroscopy of the brain. Applied optics 48, D280-D298.

Huppert, T.J., Hoge, R.D., Diamond, S.G., Franceschini, M.A., Boas, D.A., 2006. A temporal comparison of BOLD, ASL, and NIRS hemodynamic responses to motor stimuli in adult humans. Neuroimage 29, 368-382.

Irani, F., Platek, S.M., Bunce, S., Ruocco, A.C., Chute, D., 2007. Functional near infrared spectroscopy (fNIRS): an emerging neuroimaging technology with important applications for the study of brain disorders. Clin Neuropsychol 21, 9-37.

Izzetoglu, M., Chitrapu, P., Bunce, S., Onaral, B., 2010. Motion artifact cancellation in NIR spectroscopy using discrete Kalman filtering. Biomed Eng Online 9, 16.

Jahanian, H., Holdsworth, S., Christen, T., Wu, H., Zhu, K., Kerr, A.B., Middione, M.J., Dougherty, R.F., Moseley, M., Zaharchuk, G., 2019. Advantages of short repetition time resting-state functional MRI enabled by simultaneous multi-slice imaging. J Neurosci Methods 311, 122-132.

Jasdzewski, G., Strangman, G., Wagner, J., Kwong, K., Poldrack, R., Boas, D., 2003. Differences in the hemodynamic response to event-related motor and visual paradigms as measured by near-infrared spectroscopy. Neuroimage 20, 479-488.

Jones, D.T., Knopman, D.S., Gunter, J.L., Graff-Radford, J., Vemuri, P., Boeve, B.F., Petersen, R.C., Weiner, M.W., Jack, C.R., Jr., Alzheimer's Disease Neuroimaging, I., 2016. Cascading network failure across the Alzheimer's disease spectrum. Brain 139, 547-562.

Keehn, B., Wagner, J.B., Tager-Flusberg, H., Nelson, C.A., 2013. Functional connectivity in the first year of life in infants at-risk for autism: a preliminary near-infrared spectroscopy study. Front Hum Neurosci 7, 444.

Khan, A.F., Zhang, F., Yuan, H., Ding, L., 2021. Brain-wide functional diffuse optical tomography of resting state networks. Journal of neural engineering 18, 046069.

Kirilina, E., Jelzow, A., Heine, A., Niessing, M., Wabnitz, H., Bruhl, R., Ittermann, B., Jacobs, A.M., Tachtsidis, I., 2012. The physiological origin of task-evoked systemic artefacts in functional near infrared spectroscopy. Neuroimage 61, 70-81.

Kirilina, E., Yu, N., Jelzow, A., Wabnitz, H., Jacobs, A.M., Tachtsidis, I., 2013. Identifying and quantifying main components of physiological noise in functional near infrared spectroscopy on the prefrontal cortex. Frontiers in human neuroscience 7, 864.

Koch, W., Teipel, S., Mueller, S., Benninghoff, J., Wagner, M., Bokde, A.L., Hampel, H., Coates, U., Reiser, M., Meindl, T., 2012. Diagnostic power of default mode network resting state fMRI in the detection of Alzheimer's disease. Neurobiol Aging 33, 466-478.

Kohno, S., Miyai, I., Seiyama, A., Oda, I., Ishikawa, A., Tsuneishi, S., Amita, T., Shimizu, K., 2007. Removal of the skin blood flow artifact in functional near-infrared spectroscopic imaging data through independent component analysis. Journal of biomedical optics 12, 062111.

Leff, D.R., Orihuela-Espina, F., Elwell, C.E., Athanasiou, T., Delpy, D.T., Darzi, A.W., Yang, G.-Z., 2011. Assessment of the cerebral cortex during motor task behaviours in adults: a systematic review of functional near infrared spectroscopy (fNIRS) studies. Neuroimage 54, 2922-2936.

Li, L., Babawale, O., Yennu, A., Trowbridge, C., Hulla, R., Gatchel, R.J., Liu, H., 2018. Whole-cortical graphical networks at wakeful rest in young and older adults revealed by functional near-infrared spectroscopy. Neurophotonics 5, 035004.

Li, R., Mayseless, N., Balters, S., Reiss, A.L., 2021. Dynamic Inter-Brain Synchrony in Real-life Inter-Personal Cooperation: A Functional Near-infrared Spectroscopy Hyperscanning Study. Neuroimage, 118263.

Liao, S.M., Gregg, N.M., White, B.R., Zeff, B.W., Bjerkaas, K.A., Inder, T.E., Culver, J.P., 2010. Neonatal hemodynamic response to visual cortex activity: high-density near-infrared spectroscopy study. J Biomed Opt 15, 026010.

Light, G.A., Williams, L.E., Minow, F., Sprock, J., Rissling, A., Sharp, R., Swerdlow, N.R., Braff, D.L., 2010. Electroencephalography (EEG) and event‐related potentials (ERPs) with human participants. Current protocols in neuroscience 52, 6.25. 21-26.25. 24.

Lindquist, M.A., Loh, J.M., Atlas, L.Y., Wager, T.D., 2009. Modeling the hemodynamic response function in fMRI: efficiency, bias and mis-modeling. Neuroimage 45, S187-S198.

Liu, T.T., 2016. Noise contributions to the fMRI signal: An overview. Neuroimage 143, 141-151.

Liu, Z., de Zwart, J.A., van Gelderen, P., Kuo, L.-W., Duyn, J.H., 2012. Statistical feature extraction for artifact removal from concurrent fMRI-EEG recordings. Neuroimage 59, 2073-2087.

Logothetis, N.K., 2008. What we can do and what we cannot do with fMRI. Nature 453, 869.

Lu, C.-M., Zhang, Y.-J., Biswal, B.B., Zang, Y.-F., Peng, D.-L., Zhu, C.-Z., 2010. Use of fNIRS to assess resting state functional connectivity. Journal of neuroscience methods 186, 242-249.

Luke, R., Larson, E., Shader, M.J., Innes-Brown, H., Van Yper, L., Lee, A.K.C., Sowman, P.F., McAlpine, D., 2021. Analysis methods for measuring passive auditory fNIRS responses generated by a block-design paradigm. Neurophotonics 8, 025008.

Maidan, I., Nieuwhof, F., Bernad-Elazari, H., Reelick, M.F., Bloem, B.R., Giladi, N., Deutsch, J.E., Hausdorff, J.M., Claassen, J.A., Mirelman, A., 2016. The role of the frontal lobe in complex walking among patients with Parkinson's disease and healthy older adults: an fNIRS study. Neurorehabilitation and neural repair 30, 963-971.

Makizako, H., Shimada, H., Park, H., Tsutsumimoto, K., Uemura, K., Suzuki, T., 2013. Brain activation during dual-task walking and executive function among older adults with mild cognitive impairment: a fNIRS study. Aging clinical and experimental research 25, 539-544.

Mantini, D., Perrucci, M.G., Cugini, S., Ferretti, A., Romani, G.L., Del Gratta, C., 2007. Complete artifact removal for EEG recorded during continuous fMRI using independent component analysis. Neuroimage 34, 598-607.

Mateo, C., Knutsen, P.M., Tsai, P.S., Shih, A.Y., Kleinfeld, D., 2017. Entrainment of arteriole vasomotor fluctuations by neural activity is a basis of blood-oxygenation-level-dependent "resting-state" connectivity. Neuron 96, 936-948. e933.

Mayeli, A., Zotev, V., Refai, H., Bodurka, J., 2016. Real-time EEG artifact correction during fMRI using ICA. Journal of neuroscience methods 274, 27-37.

Mesquita, R.C., Franceschini, M.A., Boas, D.A., 2010. Resting state functional connectivity of the whole head with near-infrared spectroscopy. Biomedical optics express 1, 324-336.

Michel, C.M., Koenig, T., 2018. EEG microstates as a tool for studying the temporal dynamics of whole-brain neuronal networks: a review. Neuroimage 180, 577-593.

Mitra, P.P., Ogawa, S., Hu, X., Uğurbil, K., 1997. The nature of spatiotemporal changes in cerebral hemodynamics as manifested in functional magnetic resonance imaging. Magnetic resonance in medicine 37, 511-518.

Molavi, B., May, L., Gervain, J., Carreiras, M., Werker, J.F., Dumont, G.A., 2013. Analyzing the resting state functional connectivity in the human language system using near infrared spectroscopy. Front Hum Neurosci 7, 921.

Morais, G.A.Z., Scholkmann, F., Balardin, J.B., Furucho, R.A., de Paula, R.C.V., Biazoli, C.E., Sato, J.R., 2017. Non-neuronal evoked and spontaneous hemodynamic changes in the anterior temporal region of the human head may lead to misinterpretations of functional near-infrared spectroscopy signals. Neurophotonics 5, 011002.

Mueller, S.G., Weiner, M.W., Thal, L.J., Petersen, R.C., Jack, C., Jagust, W., Trojanowski, J.Q., Toga, A.W., Beckett, L., 2005. The Alzheimer's disease neuroimaging initiative. Neuroimaging Clinics 15, 869-877.

Musso, F., Brinkmeyer, J., Mobascher, A., Warbrick, T., Winterer, G., 2010. Spontaneous brain activity and EEG microstates. A novel EEG/fMRI analysis approach to explore resting-state networks. Neuroimage 52, 1149-1161.

Naseer, N., Hong, K.-S., 2015. fNIRS-based brain-computer interfaces: a review. Frontiers in human neuroscience 9, 3.

Necka, E.A., Lee, I.S., Kucyi, A., Cheng, J.C., Yu, Q., Atlas, L.Y., 2019. Applications of dynamic functional connectivity to pain and its modulation. Pain Rep 4, e752.

Nguyen, H.-D., Yoo, S.-H., Bhutta, M.R., Hong, K.-S., 2018. Adaptive filtering of physiological noises in fNIRS data. Biomedical engineering online 17, 180.

Nierhaus, T., Gundlach, C., Goltz, D., Thiel, S.D., Pleger, B., Villringer, A., 2013. Internal ventilation system of MR scanners induces specific EEG artifact during simultaneous EEG-fMRI. Neuroimage 74, 70-76.

Nieuwhof, F., Reelick, M.F., Maidan, I., Mirelman, A., Hausdorff, J.M., Olde Rikkert, M.G., Bloem, B.R., Muthalib, M., Claassen, J.A., 2016. Measuring prefrontal cortical activity during dual task walking in patients with Parkinson's disease: feasibility of using a new portable fNIRS device. Pilot and feasibility studies 2, 1-11.

Noah, J.A., Zhang, X., Dravida, S., DiCocco, C., Suzuki, T., Aslin, R.N., Tachtsidis, I., Hirsch, J., 2021. Comparison of short-channel separation and spatial domain filtering for removal of non-neural components in functional near-infrared spectroscopy signals. Neurophotonics 8, 015004.

Novi, S.L., Roberts, E., Spagnuolo, D., Spilsbury, B.M., D'manda, C.P., Imbalzano, C.A., Forero, E., Yodh, A.G., Tellis, G.M., Tellis, C.M., 2020. Functional near-infrared spectroscopy for speech protocols: characterization of motion artifacts and guidelines for improving data analysis. Neurophotonics 7, 015001.

Obrig, H., 2014. NIRS in clinical neurology—a 'promising'tool? Neuroimage 85, 535-546.

Obrig, H., Israel, H., Kohl-Bareis, M., Uludag, K., Wenzel, R., Muller, B., Arnold, G., Villringer, A., 2002. Habituation of the visually evoked potential and its vascular response: implications for neurovascular coupling in the healthy adult. Neuroimage 17, 1-18.

Obrig, H., Neufang, M., Wenzel, R., Kohl, M., Steinbrink, J., Einhaupl, K., Villringer, A., 2000. Spontaneous low frequency oscillations of cerebral hemodynamics and metabolism in human adults. Neuroimage 12, 623-639.

Ogawa, S., Lee, T.-M., Kay, A.R., Tank, D.W., 1990. Brain magnetic resonance imaging with contrast dependent on blood oxygenation. Proceedings of the National Academy of Sciences 87, 9868-9872.

Oostenveld, R., Praamstra, P., 2001. The five percent electrode system for high-resolution EEG and ERP measurements. Clinical neurophysiology 112, 713-719.

Otti, A., Guendel, H., Henningsen, P., Zimmer, C., Wohlschlaeger, A.M., Noll-Hussong, M., 2013. Functional network connectivity of pain-related resting state networks in somatoform pain disorder: an exploratory fMRI study. J Psychiatry Neurosci 38, 57-65.

Perrey, S., 2008. Non-invasive NIR spectroscopy of human brain function during exercise. Methods 45, 289-299.

Pinti, P., Scholkmann, F., Hamilton, A., Burgess, P., Tachtsidis, I., 2018. Current status and issues regarding pre-processing of fNIRS neuroimaging data: An investigation of diverse signal filtering methods within a General Linear Model framework. Frontiers in human neuroscience 12.

Piper, S.K., Krueger, A., Koch, S.P., Mehnert, J., Habermehl, C., Steinbrink, J., Obrig, H., Schmitz, C.H., 2014. A wearable multi-channel fNIRS system for brain imaging in freely moving subjects. Neuroimage 85, 64-71.

Plichta, M.M., Gerdes, A.B., Alpers, G.W., Harnisch, W., Brill, S., Wieser, M.J., Fallgatter, A.J., 2011. Auditory cortex activation is modulated by emotion: a functional near-infrared spectroscopy (fNIRS) study. Neuroimage 55, 1200-1207.

Pollonini, L., Olds, C., Abaya, H., Bortfeld, H., Beauchamp, M.S., Oghalai, J.S., 2014. Auditory cortex activation to natural speech and simulated cochlear implant speech measured with functional near-infrared spectroscopy. Hear Res 309, 84-93.

Power, J.D., Barnes, K.A., Snyder, A.Z., Schlaggar, B.L., Petersen, S.E., 2012. Spurious but systematic correlations in functional connectivity MRI networks arise from subject motion. Neuroimage 59, 2142-2154.

Power, J.D., Barnes, K.A., Snyder, A.Z., Schlaggar, B.L., Petersen, S.E., 2013. Steps toward optimizing motion artifact removal in functional connectivity MRI; a reply to Carp. Neuroimage 76.

Power, J.D., Cohen, A.L., Nelson, S.M., Wig, G.S., Barnes, K.A., Church, J.A., Vogel, A.C., Laumann, T.O., Miezin, F.M., Schlaggar, B.L., 2011. Functional network organization of the human brain. Neuron 72, 665-678.

Putze, F., Hesslinger, S., Tse, C.-Y., Huang, Y., Herff, C., Guan, C., Schultz, T., 2014. Hybrid fNIRS-EEG based classification of auditory and visual perception processes. Frontiers in neuroscience 8, 373.

Raitamaa, L., Huotari, N., Korhonen, V., Helakari, H., Koivula, A., Kananen, J., Kiviniemi, V., 2021. Spectral analysis of physiological brain pulsations affecting the BOLD signal. Hum Brain Mapp 42, 4298-4313.

Rondinoni, C., Amaro, E., Cendes, F., Dos Santos, A., Salmon, C., 2013. Effect of scanner acoustic background noise on strict resting-state fMRI. Brazilian journal of medical and biological research 46, 359-367.

Saager, R.B., Berger, A.J., 2005. Direct characterization and removal of interfering absorption trends in two-layer turbid media. JOSA A 22, 1874-1882.

Saager, R.B., Berger, A.J., 2008. Measurement of layer-like hemodynamic trends in scalp and cortex: implications for physiological baseline suppression in functional near-infrared spectroscopy. Journal of biomedical optics 13, 034017.

Saliba, J., Bortfeld, H., Levitin, D.J., Oghalai, J.S., 2016. Functional near-infrared spectroscopy for neuroimaging in cochlear implant recipients. Hearing research 338, 64-75.

Santosa, H., Zhai, X., Fishburn, F., Sparto, P.J., Huppert, T.J., 2020. Quantitative comparison of correction techniques for removing systemic physiological signal in functional near-infrared spectroscopy studies. Neurophotonics 7, 035009.

Sasai, S., Homae, F., Watanabe, H., Taga, G., 2011. Frequency-specific functional connectivity in the brain during resting state revealed by NIRS. Neuroimage 56, 252-257.

Sato, T., Nambu, I., Takeda, K., Aihara, T., Yamashita, O., Isogaya, Y., Inoue, Y., Otaka, Y., Wada, Y., Kawato, M., 2016. Reduction of global interference of scalp-hemodynamics in functional near-infrared spectroscopy using short distance probes. Neuroimage 141, 120-132.

Schecklmann, M., Mann, A., Langguth, B., Ehlis, A.-C., Fallgatter, A.J., Haeussinger, F.B., 2017. The temporal muscle of the head can cause artifacts in optical imaging studies with functional near-infrared spectroscopy. Frontiers in human neuroscience 11, 456.

Scholkmann, F., Kleiser, S., Metz, A.J., Zimmermann, R., Mata Pavia, J., Wolf, U., Wolf, M., 2014. A review on continuous wave functional near-infrared spectroscopy and imaging instrumentation and methodology. Neuroimage 85 Pt 1, 6-27.

Scholkmann, F., Spichtig, S., Muehlemann, T., Wolf, M., 2010. How to detect and reduce movement artifacts in near-infrared imaging using moving standard deviation and spline interpolation. Physiological measurement 31, 649.

Schuenke, M., Schulte, E., Schumacher, U., 2010. Thieme atlas of anatomy: head and neuroanatomy. Thieme.

Ségonne, F., Dale, A.M., Busa, E., Glessner, M., Salat, D., Hahn, H.K., Fischl, B., 2004. A hybrid approach to the skull stripping problem in MRI. Neuroimage 22, 1060-1075.

Sevy, A.B., Bortfeld, H., Huppert, T.J., Beauchamp, M.S., Tonini, R.E., Oghalai, J.S., 2010. Neuroimaging with near-infrared spectroscopy demonstrates speech-evoked activity in the auditory cortex of deaf children following cochlear implantation. Hear Res 270, 39-47.

Sherafati, A., Snyder, A.Z., Eggebrecht, A.T., Bergonzi, K.M., Burns‐Yocum, T.M., Lugar, H.M., Ferradal, S.L., Robichaux‐Viehoever, A., Smyser, C.D., Palanca, B.J., 2020. Global motion detection and censoring in high‐density diffuse optical tomography. Human brain mapping 41, 4093-4112.

Shmuel, A., Yacoub, E., Pfeuffer, J., Van de Moortele, P.F., Adriany, G., Hu, X., Ugurbil, K., 2002. Sustained negative BOLD, blood flow and oxygen consumption response and its coupling to the positive response in the human brain. Neuron 36, 1195-1210.

Shmueli, K., van Gelderen, P., de Zwart, J.A., Horovitz, S.G., Fukunaga, M., Jansma, J.M., Duyn, J.H., 2007. Low-frequency fluctuations in the cardiac rate as a source of variance in the resting-state fMRI BOLD signal. Neuroimage 38, 306-320.

Shulman, R.G., Rothman, D.L., Behar, K.L., Hyder, F., 2004. Energetic basis of brain activity: implications for neuroimaging. Trends in neurosciences 27, 489-495.

Sorg, C., Riedl, V., Mühlau, M., Calhoun, V.D., Eichele, T., Läer, L., Drzezga, A., Förstl, H., Kurz, A., Zimmer, C., 2007. Selective changes of resting-state networks in individuals at risk for Alzheimer's disease. Proceedings of the National Academy of Sciences 104, 18760-18765.

Sperling, R., Mormino, E., Johnson, K., 2014. The evolution of preclinical Alzheimer's disease: implications for prevention trials. Neuron 84, 608-622.

Sperling, R.A., Dickerson, B.C., Pihlajamaki, M., Vannini, P., LaViolette, P.S., Vitolo, O.V., Hedden, T., Becker, J.A., Rentz, D.M., Selkoe, D.J., 2010. Functional alterations in memory networks in early Alzheimer's disease. Neuromolecular medicine 12, 27-43.

Sperling, R.A., LaViolette, P.S., O'Keefe, K., O'Brien, J., Rentz, D.M., Pihlajamaki, M., Marshall, G., Hyman, B.T., Selkoe, D.J., Hedden, T., 2009. Amyloid deposition is associated with impaired default network function in older persons without dementia. Neuron 63, 178-188.

Srinivasan, S., Pogue, B.W., Jiang, S., Dehghani, H., Paulsen, K.D., 2005. Spectrally constrained chromophore and scattering near-infrared tomography provides quantitative and robust reconstruction. Applied optics 44, 1858-1869.

Stefanovska, A., Bracic, M., Kvernmo, H.D., 1999. Wavelet analysis of oscillations in the peripheral blood circulation measured by laser Doppler technique. IEEE Transactions on Biomedical Engineering 46, 1230-1239.

Strangman, G., Culver, J.P., Thompson, J.H., Boas, D.A., 2002. A quantitative comparison of simultaneous BOLD fMRI and NIRS recordings during functional brain activation. Neuroimage 17, 719-731.

Sutoko, S., Chan, Y.L., Obata, A., Sato, H., Maki, A., Numata, T., Funane, T., Atsumori, H., Kiguchi, M., Tang, T.B., 2019. Denoising of neuronal signal from mixed systemic low-frequency oscillation using peripheral measurement as noise regressor in near-infrared imaging. Neurophotonics 6, 015001.

Tachtsidis, I., Scholkmann, F., 2016. False positives and false negatives in functional near-infrared spectroscopy: issues, challenges, and the way forward. Neurophotonics 3, 031405.

Tak, S., Ye, J.C., 2014. Statistical analysis of fNIRS data: a comprehensive review. Neuroimage 85, 72-91.

Takahashi, T., Takikawa, Y., Kawagoe, R., Shibuya, S., Iwano, T., Kitazawa, S., 2011. Influence of skin blood flow on near-infrared spectroscopy signals measured on the forehead during a verbal fluency task. Neuroimage 57, 991-1002.

Talairach, J., Tournoux, P., 1988. Co-planar stereotaxic atlas of the human brain. 1988. New York: Theime.

Teplan, M., 2002. Fundamentals of EEG measurement. Measurement science review 2, 1-11.

Thomas Yeo, B., Krienen, F.M., Sepulcre, J., Sabuncu, M.R., Lashkari, D., Hollinshead, M., Roffman, J.L., Smoller, J.W., Zöllei, L., Polimeni, J.R., 2011. The organization of the human cerebral cortex estimated by intrinsic functional connectivity. Journal of neurophysiology 106, 1125-1165.

Tong, Y., 2010. Time lag dependent multimodal processing of concurrent fMRI and near-infrared spectroscopy (NIRS) data suggests a global circulatory origin for low-frequency oscillation signals in human brain. Neuroimage 53, 553-564.

Tong, Y., 2012. Concurrent fNIRS and fMRI processing allows independent visualization of the propagation of pressure waves and bulk blood flow in the cerebral vasculature. Neuroimage 61, 1419-1427.

Tong, Y., Frederick, B.d., 2014. Studying the spatial distribution of physiological effects on BOLD signals using ultrafast fMRI. Frontiers in human neuroscience 8, 196.

Tong, Y., Hocke, L.M., Frederick, B.B., 2019. Low frequency systemic hemodynamic" noise" in resting state BOLD fMRI: Characteristics, Causes, Implications, Mitigation Strategies, and Applications. Frontiers in neuroscience 13, 787.

Tong, Y., Lindsey, K.P., de, B.F.B., 2011. Partitioning of physiological noise signals in the brain with concurrent near-infrared spectroscopy and fMRI. J Cereb Blood Flow Metab 31, 2352-2362.

Torricelli, A., Contini, D., Pifferi, A., Caffini, M., Re, R., Zucchelli, L., Spinelli, L., 2014. Time domain functional NIRS imaging for human brain mapping. Neuroimage 85 Pt 1, 28-50.

Tsvetanov, K.A., Henson, R.N., Rowe, J.B., 2021. Separating vascular and neuronal effects of age on fMRI BOLD signals. Philosophical Transactions of the Royal Society B 376, 20190631.

Urquhart, E.L., Wanniarachchi, H., Wang, X., Gonzalez-Lima, F., Alexandrakis, G., Liu, H., 2020. Transcranial photobiomodulation-induced changes in human brain functional connectivity and network metrics mapped by whole-head functional near-infrared spectroscopy in vivo. Biomedical optics express 11, 5783-5799.

Valet, M., Sprenger, T., Boecker, H., Willoch, F., Rummeny, E., Conrad, B., Erhard, P., Tolle, T.R., 2004. Distraction modulates connectivity of the cingulo-frontal cortex and the midbrain during pain--an fMRI analysis. Pain 109, 399-408.

Van Dijk, K.R., Sabuncu, M.R., Buckner, R.L., 2012. The influence of head motion on intrinsic functional connectivity MRI. Neuroimage 59, 431-438.

Van Essen, D.C., Smith, S.M., Barch, D.M., Behrens, T.E., Yacoub, E., Ugurbil, K., Consortium, W.-M.H., 2013. The WU-Minn human connectome project: an overview. Neuroimage 80, 62-79.

Villringer, A., Chance, B., 1997. Non-invasive optical spectroscopy and imaging of human brain function. Trends Neurosci 20, 435-442.

Virtanen, J., Noponen, T.E., Meriläinen, P., 2009. Comparison of principal and independent component analysis in removing extracerebral interference from near-infrared spectroscopy signals. Journal of biomedical optics 14, 054032.

Volkening, N., Unni, A., Löffler, B.S., Fudickar, S., Rieger, J.W., Hein, A., 2016. Characterizing the influence of muscle activity in fNIRS brain activation measurements. IFAC-PapersOnLine 49, 84-88.

von Lühmann, A., Boukouvalas, Z., Müller, K.-R., Adalı, T., 2019. A new blind source separation framework for signal analysis and artifact rejection in functional Near-Infrared Spectroscopy. Neuroimage 200, 72-88.

von Lühmann, A., Li, X., Müller, K.-R., Boas, D.A., Yücel, M.A., 2020. Improved physiological noise regression in fNIRS: A multimodal extension of the General Linear Model using temporally embedded Canonical Correlation Analysis. Neuroimage 208, 116472.

Wan, N., Hancock, A.S., Moon, T.K., Gillam, R.B., 2018. A functional near-infrared spectroscopic investigation of speech production during reading. Hum Brain Mapp 39, 1428-1437.

Wanniarachchi, H., Wang, X., Urquhart, E.L., Liu, H., 2021. Transcranial Photobiomodulation (tPBM) Enhances Local Hemodynamics and Global Dynamic Connectivity in the Cortex as Measured by fNIRS. Bio-Optics: Design and Application. Optical Society of America, p. JTu4A. 28.

Watabe, T., Hatazawa, J., 2019. Evaluation of Functional Connectivity in the Brain Using Positron Emission Tomography: A Mini-Review. Frontiers in neuroscience 13, 775.

Watanabe, H., Shitara, Y., Aoki, Y., Inoue, T., Tsuchida, S., Takahashi, N., Taga, G., 2017. Hemoglobin phase of oxygenation and deoxygenation in early brain development measured using fNIRS. Proceedings of the National Academy of Sciences of the United States of America 114, E1737-E1744.

Wheelock, M.D., Culver, J.P., Eggebrecht, A.T., 2019. High-density diffuse optical tomography for imaging human brain function. Review of Scientific Instruments 90, 051101.

White, B.R., Liao, S.M., Ferradal, S.L., Inder, T.E., Culver, J.P., 2012. Bedside optical imaging of occipital resting-state functional connectivity in neonates. Neuroimage 59, 2529-2538.

White, B.R., Snyder, A.Z., Cohen, A.L., Petersen, S.E., Raichle, M.E., Schlaggar, B.L., Culver, J.P., 2009. Resting-state functional connectivity in the human brain revealed with diffuse optical tomography. Neuroimage 47, 148-156.

Wise, R.G., Ide, K., Poulin, M.J., Tracey, I., 2004. Resting fluctuations in arterial carbon dioxide induce significant low frequency variations in BOLD signal. Neuroimage 21, 1652-1664.

Wu, M., Wang, Y., Zhao, X., Xin, T., Wu, K., Liu, H., Wu, S., Lin, M., Chai, X., Li, J., 2022. Anti-phasic oscillatory development for speech and noise processing in cochlear implanted toddlers. bioRxiv.

Wyser, D., Mattille, M., Wolf, M., Lambercy, O., Scholkmann, F., Gassert, R., 2020. Short-channel regression in functional near-infrared spectroscopy is more effective when considering heterogeneous scalp hemodynamics. Neurophotonics 7, 035011.

Xia, M., Wang, J., He, Y., 2013. BrainNet Viewer: a network visualization tool for human brain connectomics. PloS one 8, e68910.

Yeo, B.T., Krienen, F.M., Sepulcre, J., Sabuncu, M.R., Lashkari, D., Hollinshead, M., Roffman, J.L., Smoller, J.W., Zollei, L., Polimeni, J.R., Fischl, B., Liu, H., Buckner, R.L., 2011. The organization of the human cerebral cortex estimated by intrinsic functional connectivity. J Neurophysiol 106, 1125-1165.

Yuan, H., Ding, L., Zhu, M., Zotev, V., Phillips, R., Bodurka, J., 2016. Reconstructing large-scale brain resting-state networks from high-resolution EEG: spatial and temporal comparisons with fMRI. Brain connectivity 6, 122-135.

Yuan, H., Perdoni, C., He, B., 2010. Relationship between speed and EEG activity during imagined and executed hand movements. Journal of neural engineering 7, 026001.

Yuan, H., Perdoni, C., Yang, L., He, B., 2011. Differential electrophysiological coupling for positive and negative BOLD responses during unilateral hand movements. Journal of Neuroscience 31, 9585-9593.

Yuan, H., Zotev, V., Phillips, R., Bodurka, J., 2013. Correlated slow fluctuations in respiration, EEG, and BOLD fMRI. Neuroimage 79, 81-93.

Yuan, H., Zotev, V., Phillips, R., Drevets, W.C., Bodurka, J., 2012. Spatiotemporal dynamics of the brain at rest—exploring EEG microstates as electrophysiological signatures of BOLD resting state networks. Neuroimage 60, 2062-2072.

Zhang, D., Raichle, M.E., 2010. Disease and the brain's dark energy. Nat Rev Neurol 6, 15-28.

Zhang, F., Cheong, D., Chen, Y., Khan, A., Ding, L., Yuan, H., 2019. Superficial Fluctuations in Functional Near-Infrared Spectroscopy. 2019 41st Annual International Conference of the IEEE Engineering in Medicine and Biology Society (EMBC).

Zhang, F., Cheong, D., Khan, A.F., Chen, Y., Ding, L., Yuan, H., 2021. Correcting Physiological Noise in Whole-Head Functional Near-Infrared Spectroscopy. Journal of neuroscience methods, 109262.

Zhang, F., Reid, A., Schroeder, A., Cutter, M., Ding, L., Yuan, H., 2022. Clenching-Related Motion Artifacts in Functional Near-Infrared Spectroscopy in the Auditory Cortex. 2022 44th Annual International Conference of the IEEE Engineering in Medicine and Biology Society (EMBC).

Zhang, H., Zhang, Y.-J., Lu, C.-M., Ma, S.-Y., Zang, Y.-F., Zhu, C.-Z., 2010. Functional connectivity as revealed by independent component analysis of resting-state fNIRS measurements. Neuroimage 51, 1150-1161.

Zhang, Q., Brown, E.N., Strangman, G.E., 2007. Adaptive filtering to reduce global interference in evoked brain activity detection: a human subject case study. Journal of biomedical optics 12, 064009.

Zhang, Q., Strangman, G.E., Ganis, G., 2009. Adaptive filtering to reduce global interference in non-invasive NIRS measures of brain activation: how well and when does it work? Neuroimage 45, 788-794.

Zhang, X., Noah, J.A., Hirsch, J., 2016. Separation of the global and local components in functional near-infrared spectroscopy signals using principal component spatial filtering. Neurophotonics 3, 015004.

Zhang, X., Yu, J., Zhao, R., Xu, W., Niu, H., Zhang, Y., Zuo, N., Jiang, T., 2015. Activation detection in functional near-infrared spectroscopy by wavelet coherence. J Biomed Opt 20, 016004.

Zhang, Y., Brooks, D.H., Franceschini, M.A., Boas, D.A., 2005. Eigenvector-based spatial filtering for reduction of physiological interference in diffuse optical imaging. Journal of biomedical optics 10, 011014.

Zhang, Y., Zhu, C., 2020. Assessing brain networks by resting-state dynamic functional connectivity: an fNIRS-EEG Study. Frontiers in neuroscience 13, 1430.

Zhou, J., Greicius, M.D., Gennatas, E.D., Growdon, M.E., Jang, J.Y., Rabinovici, G.D., Kramer, J.H., Weiner, M., Miller, B.L., Seeley, W.W., 2010. Divergent network connectivity changes in behavioural variant frontotemporal dementia and Alzheimer's disease. Brain 133, 1352-1367.

Multimodal Functional Neuroimaging: Integrating Functional MRI and EEG/MEG

Author: Bin He

Publication: IEEE Reviews in Biomedical Engineering

Publisher: IEEE

Date: 2008

1) The following IEEE copyright/ credit notice should be placed prominently in the references: © [year of original publication] IEEE. Reprinted, with permission, from [author names, paper title, IEEE publication title, and month/year of publication]

2) Only the accepted version of an IEEE copyrighted paper can be used when posting the paper or your thesis on-line.

3) In placing the thesis on the author's university website, please display the following message in a prominent place on the website: In reference to IEEE copyrighted material which is used with permission in this thesis, the IEEE does not endorse any of [university/educational entity's name goes here]'s products or services. Internal or personal use of this material is permitted. If interested in reprinting/republishing IEEE copyrighted material for advertising or promotional purposes or for creating new collective works for resale or redistribution, please go to http://www.ieee.org/publications_standards/publications/rights/rights_link.html to learn how to obtain a License from RightsLink.

If applicable, University Microfilms and/or ProQuest Library, or the Archives of Canada may supply single copies of the dissertation.

Correcting physiological noise in whole-head functional near-infrared spectroscopy

Author: Fan Zhang

Publication: Journal of Neuroscience Methods

Date: 2021

Publisher: Elsevier